Geofísica Internacional

— Geofísica Internacional —

Contents

CARTA DE LOS EDITORES

Cerca de la medianoche del 7 de septiembre de 2017 (08/09/2017, 04:49:17 UTC) ocurrió uno de los sismos más grandes registrados instrumentalmente en México. La magnitud estimada (Mw=8.2) es solo comparable con el sismo de 1932 ocurrido en las costas de Jalisco y Colima.

En este caso la ruptura ocurrió en el golfo de Tehuantepec aproximadamente a unos 150 km de la costa del estado de Chiapas.

Su magnitud no fue la única sorpresa, su mecanismo focal y la profundidad reportada mostraron que no se trataba de un sismo de subducción sino un sismo de fallamiento normal (asociado a un régimen extensivo). Los daños provocados fueron cuantiosos especialmente en el Istmo de Tehuantepec y en la zona costera de Chiapas. Afectaciones importantes fueron reportadas aún a cientos de kilómetros como en las ciudades de Villahermosa y Puebla. El sismo provocó el lamentable deceso de 96 personas en su mayoría fallecidos en la ciudad de Juchitán.

Los protocolos de Protección Civil fueron activados y la atención a víctimas y población afectada fue un tema central por varios días. La sociedad civil también se organizó para recabar ayuda humanitaria y enviarla a las zonas más afectadas.

En este marco y como cada año, 12 días después, el 19 de septiembre, se recordaba con tristeza el terremoto que marcó la historia de la Ciudad de México en 1985. Como parte de un simulacro de sismo, a las 11:00 de la mañana sonaron, en la CDMX y en otros estados de la República Mexicana, las alarmas usadas para difundir el sistema de alerta sísmica. Nadie en ese momento podría imaginar que dos horas después, a las 13:14 (19/09/2017, 19:14:39), ocurriría un temblor que nuevamente afectaría notablemente a esta megalópolis y a un número muy importante de ciudades y poblaciones de los estados de Morelos, Puebla y Estado de México.

Ante la relevancia de estos dos sismos, la revista *Geofísica Internacional* invitó a la comunidad científica a presentar trabajos en una amplia gama de aspectos relacionados con ambos sismos. Los trabajos serán publicados en una sección a lo largo de algunos números del presente año.

Los editores encargados agradecen la invitación y esperan que la comunidad científica relacionada con los temas discutidos se enriquezca y motive con la información y discusiones vertidas en los trabajos publicados.

Eduardo Reinoso Angulo   Arturo Iglesias Mendoza

Some minutes before midnight of September 7th in 2017 (08/09/2017, 04:49:17 UTC) occurred one of the largest earthquakes ever recorded in Mexico. Estimated magnitude (Mw=8.2) is only compared to the magnitude of 1932 Jalisco-Colima earthquake.

Now, the rupture occurred in Tehuantepec gulf around 150 km far from the coast of Chiapas State.

Magnitude not was the only surprise, its focal mechanism and the reported depth showed that this earthquake was not a subduction event but a normal fault earthquake (related to an extensive regime). Severe damage was reported especially in Tehuantepec Isthmus and in the coastal zone of Chiapas. Relevant disturbances were reported even within hundreds of kilometers away from epicenter in cities such as Villahermosa and Puebla. This earthquake unfortunately killed 96 people, most of them in Juchitán City.

Civil protection procedures were activated and the attention to victims and affected population was the focus for several days. Non-gubernamental institutions and people in general were organized to collect funds, food and other important things, and sent them to the most affected areas.

Within this context and as every year, 12 days after, on September 19th, the activities for the sad commemoration of the 1985 earthquake were being carried out. As part of a national earthquake drill, at 11:00 AM, alarms sounded in Mexico City and other parts of the country. Nobody could not imagine at that time, that two hours later, at 01:14 PM (19/09/2017, 19:14:39), an earthquake would occur and could affect this megacity and important cities of Morelos, Puebla and México States.

This earthquake killed 369 persons and an important number of buildings suffered moderate to severe damages.

Damage to the colonial heritage was remarkable, and even to some prehispanic buildings (*e.g.* Archeological site of Xochicalco).

There were a lot of reports of notable changes in the prolific hydrological system of Morelos state and some of its emblematic spas.

Due to the relevance of these two earthquakes, the *Geofísica Internacional* journal invited the scientific community to present papers related to any aspect of these earthquakes. Articles will be published in a dedicated section along some issues during this year.

Invited editors acknowledge the invitation to coordinate efforts and hope that the scientific community will benefit from the information and discussions expressed in the published papers.

Eduardo Reinoso Angulo   Arturo Iglesias Mendoza

Moment Tensor Catalog for Mexican Earthquakes: Almost Two Decades of Seismicity

Sara Ivone Franco[1]*, Arturo Iglesias[2] and Eiichi Fukuyama[3]

Resumen

Con el objetivo de obtener las soluciones del tensor de momento para temblores con M $\geq$ 4.0 reportados en el territorio nacional en el periodo 2000-2018, hemos analizado más de 20,000 temblores utilizando las formas de onda y el catálogo del SSN (Servicio Sismológico Nacional).

Debido al número de eventos, en este artículo proponemos un procedimiento automático basado en un conjunto de criterios que permita obtener las soluciones del tensor de momento para el mayor número posible de eventos.

Utilizando la localización epicentral y la magnitud preliminar para cada evento se determina un subconjunto de estaciones válidas. La longitud mínima del registro y el filtro que se aplica a los sismogramas observados y sintéticos es definido de manera automática. La formulación aplicada requiere el conocimiento de la función de Green elástica entre cada par temblor-estación. Para reducir el tiempo de cómputo se usa una biblioteca de funciones de Green pre-calculadas. A través de una inversión lineal, para combinaciones de tres estaciones, los datos observados y las funciones de Green correspondientes son utilizados para determinar el tensor de momentos sísmicos (con parte isotrópica nula). Para minimizar posibles sesgos asociados a una distribución lineal de las estaciones utilizadas, cada solución es pesada en función de la cobertura azimutal.

Siguiendo el proceso automático propuesto se obtuvieron soluciones para tan solo 8,000 temblores; ésto debido a ciertas limitaciones como pueden ser el tamaño del registro disponible y/o la integridad de los mismos. La calidad de las soluciones se mide a través del valor de la reducción de la varianza (VR). Un análisis estadístico de la calidad nos permite establecer como límite admissible para soluciones confiables un valor de VR $\geq$ 50%.

Con este criterio, presentamos un catálogo con 1,500 eventos, incluyendo algunos eventos pequeños (Mw < 4.0). La ubicación de los eventos bien resueltos coincide con las áreas de mayor densidad de estaciones sismológicas y, a la vez, con los límites de las placas tectónicas. La

*Corresponding author
ivonne@geofisica.unam.mx

1 Departamento de Sismología
Instituto de Geofísica
UNAM
México City
arturo@igeofisica.unam.mx

3 National Research Institute for Earth Science and disaster Resilence
Tsukuba, Japan. fuku@bosai.go.jp

Now at department of Civil and Earth resources engineering,
Graduate School of engineering,
Kyoto University, Kyoto, Japan.
fukuyama.eiichi.3x@kyoto-u.ac.jp

comparación entre el catálogo obtenido en este trabajo y el presentado por el Global Centroid Moment Tensor (GCMT) arroja similitudes importantes; sin embargo, lamagnitud reportada en nuestro catálogo es sistemáticamente menor que aquélla reportada por el GCMT.

La ubicación de los eventos bien resueltos coincide con las áreas de mayor densidad de estaciones sismológicas y, a la vez, con los límites de las placas tectónicas. La comparación entre el catálogo obtenido en este trabajo y el presentado por el Global Centroid Moment Tensor (GCMT) arroja similitudes importantes; sin embargo, también muestra un sesgo sistemático en la magnitud reportada por ambos catálogos. El catálogo obtenido es presentado en línea en una base de datos pública (132.248.6.13/~cmt). Este trabajo es el primero en México que presenta una base de datos de esta índole.

ABSTRACT

In this work we used waveforms and the catalog of National Seismological Service (SSN) to analyze more than 20,000 events with M>= 4.0 for the period 2000-2018 with the goal of determining their moment tensor solutions. Because of large number of events, we automatize the process based on a set criteria. Using epicentral location and magnitude of each earthquake reported by the SSN, a set of valid stations to be used for the moment solution, the length of time series, and the filter band for data and synthetics are automatically selected. To expedite calculations a pre-computed library of Green functions is used.

Through a linear inversion, for three-station combinations, the observed data and the corresponding Green functions are used to determine the seismic moment tensor (with null isotropic component). To reduce a possible bias related to the station distribution, each solution is weightened as a function of the azimuthal coverage of the stations used. After the automatic process solutions of only 8,000 earthquakes could be obtained; other events were rejected because of incomplete length of the data segment and/or its integrity.

The solution quality is measured by the variance reduction value (VR). A statistical analysis of quality allows us to establish a VR value of $\geq$ 50% as reasonable threshold for reliable solutions. With these criteria a catalog of ~ 1,500 events have been compiled, including some small events (Mw < 4.0).

There is evidence that show that the location of the well-solved events matches the areas of higher density of seismologic stations, and the limits of tectonic plates as well. A comparison between the catalog here obtained and the Global Centroid Moment Tensor (GCMT) catalog shows similarities. However, the magnitude reported in our catalog is systematically smaller than those reported by GCMT.

The moment tensor solution catalog is available online in a public database (132.248.6.13/~cmt). This work is the first in Mexico in which a database of this kind is presented.

KEY WORDS: Moment Tensor, Mexico, database, catalogs, seismicity, GCMT. (p. 55).

INTRODUCTION

Mexican National Seismological Service (SSN, by its Spanish acronym) is the agency responsible to provide information about the earthquakes which occur in Mexico. The parameters routinely reported are magnitude, hypocentral location, and origin time. However, presently, seismic moment tensor is not routinely reported. Seismic moment tensor includes useful information about the focal mechanism and magnitude of the earthquake which are critical in understanding geological processes, seismotectonics, and seismic hazard.

Seismic Moment Tensor Solutions (MTS) for earthquakes worldwide, including Mexico, are systematically computed by the Global Centroid Moment Tensor Project (GCMT) (Dziewonski and Woodhouse, 1983; Ekström *et al.*, 2012; http://www.globalcmt.org/), and by the National Earthquake Information Center (NEIC) (http://neic.usgs.gov). In both cases, body and surface waves, recorded at teleseismic distances, are inverted to obtain the MTS.

The GCMT catalog includes seismic moment tensor for most of the global earthquakes with $Mw \geq 5$ (http://www.globalcmt.org/), and, typically, quick solutions are published from some tenths of minutes to a few hours after the earthquake. The GCMT uses a method developed by Dziewonsky *et al.* (1981) to invert long-period body and mantle waves. Seismic data used is provided by stations of the Global Seismic Network (GSN) and of the Incorporated Research Institutions for Seismology (IRIS). On the other hand, NEIC follows the method developed by Sipkin (1982), which uses long-period data from the vertical component (IRIS and GSN networks) to invert body-waves. This approach is focused on the USA and adjacent areas. For Mexico it includes most of the $Mw \geq 6$ events (http://earthquake.usgs.gov/earthquakes/eqarchives/sopar/). Additionally, NEIC computes W-phase Moment Tensor (Kanamori and Rivera, 2008; Hayes *et al.*, 2009) for significant worldwide earthquakes.

Due to the interest in (a) getting focal parameters of earthquakes in near real time, and (b) to complete the catalogs for earthquakes with $Mw < 5.0$, systems based on regional data have emerged in the last years. Since the early 90's, the Berkeley Seismological Laboratory developed an automatic system that allows to compute the MTS few minutes after the occurrence of an earthquake in California (Romanovicz *et al.*, 1993; NCDEC, 2014). This methodology has been used in several other regional systems.

The National Research Institute for Earth Science and Disaster Resilience computes most $M > 4.0$ earthquakes and some $M > 3.5$ earthquakes for Japan (Fukuyama *et al.*, 1999). In Italy, the Mediterranean Very Broadband Seismographic Network implemented an automatic moment tensor computation for earthquakes with $M > 3.5$ (Pondrelli *et al.*, 2003; Pondrelli *et al.*, 2015). In Spain, the National Geographic Institute implemented a near real time moment tensor computation using data of a broadband network, which triggers with $M > 3.5$ earthquakes (Rueda and Mezcua, 2005).

In the case of Mexico, there are some papers in which MTS has been computed with regional and/or local Mexican data for earthquakes with $Mw < 5$; however, the scope of these works is for specific areas (e.g. Zúñiga *et al.*, 2003; Pacheco and Singh, 2010).

In this work we present the first Moment Tensor catalog, on a regional scale, for earthquakes recorded by the SSN.

Mexico is located in a tectonically active setting. Most of the recorded seismicity is due to the interaction between five major tectonic plates (Figure 1), namely: North American, Pacific, Cocos, Rivera and Caribbean. This tectonic context represents a challenge for improving strategies to monitor seismic activity and to get more information about the recorded events.

In the last two decades, the SSN has experienced a significant expansion in the broadband station network. At present, the SSN operates a seismic network of ~60 broadband seismic stations (Figure 1). Earthquake locations and magnitudes are obtained and reported routinely (available in www.ssn.unam.mx).

The broadband seismic stations operated by SSN are equipped with broadband triaxial seismometers. A 100 sps real time velocity stream is sent to the central facilities. In the early 21st century only small segments of data containing regional earthquakes were stored. Nowadays, data is stored in 1-day mseed file continuous stream. Using a web search over the SSN's catalog (http://www2.ssn.unam.mx:8080/catalogo/), we found 22,024 earthquakes with $M \geq 4$ in the period January 2000 - December 2018. In this paper, we use a systematic and automatic procedure to compute MTS for these events.
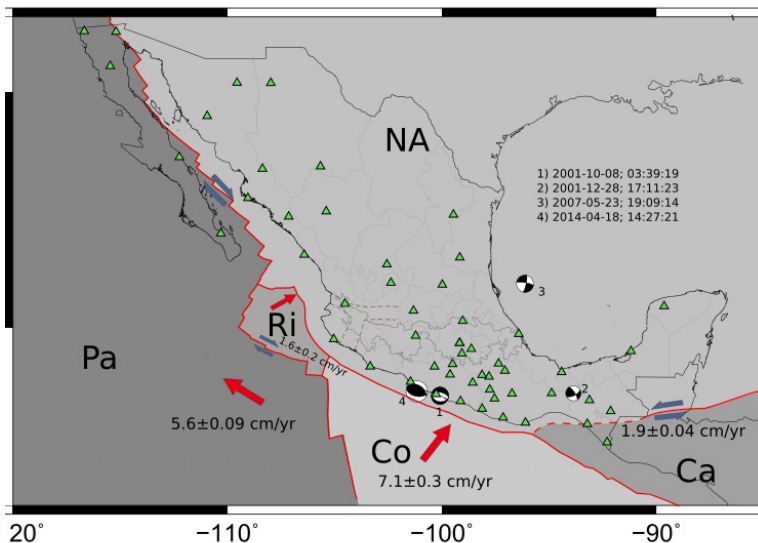
Figure 1. Mexico's tectonic setting. NA: North America plate, Pa: Pacific plate, Ri: Rivera plate, Co: Cocos plate, Ca: Caribbean plate. The arrows show relative motion between plates. The velocities are relative to NA and were taken from MORVEL (DeMets *et al.*, 2010). The triangles show the SSN broadband stations in 2018. The "beach balls" are the MTS solutions for 4 events taken from the database; more details about these events are given in the text. Number of the event is keyed to Table 3.

METHOD

The method used in this work was proposed by Fukuyama *et al.* (1999) and adapted to the SSN database by Franco *et al.* (2002) and Iglesias *et al.* (2008). As described later, the algorithm requires a minimum data record length. The algorithm searches the segment containing the record of the earthquake in 1-day mseed file or in the segment stored in the case of the early years.

We present a brief description of the method used to determine the moment tensor (further details can be found in Fukuyama *et al.*, 1999). The computation procedure is based on the Time-Domain Moment Tensor inversion method developed at the Berkeley Seismological Laboratory (Dreger and Helmberger, 1993; Pasyanos *et al.*, 1996).

For a point source, the observed displacement ds(t) at a seismic station located on Earth's surface can be computed as the convolution of the seismic moment tensor (M_{ij} and the derivative of Green's function ($G_{si,j}(t)$, which represents the response of the propagation media to a unit pulse recorded in some location:

$$d_s(t) = M_{ij} * G_{si,j}(t) \tag{1}$$

Kikuchi and Kanamori (1991) proposed to decompose the M_{ij} tensor as a combination of six elementary faults, M_n:

$$M_1 = \begin{bmatrix} 0 & 1 & 0 \\ 1 & 0 & 0 \\ 0 & 0 & 0 \end{bmatrix}; \; M_2 = \begin{bmatrix} 1 & 0 & 0 \\ 0 & -1 & 0 \\ 0 & 0 & 0 \end{bmatrix}; \; M_3 = \begin{bmatrix} 0 & 0 & 0 \\ 0 & 0 & -1 \\ 0 & 1 & 0 \end{bmatrix}$$

$$M_4 = \begin{bmatrix} 0 & 0 & 1 \\ 0 & 0 & 0 \\ 1 & 0 & 0 \end{bmatrix}; \; M_5 = \begin{bmatrix} -1 & 0 & 0 \\ 0 & 0 & 0 \\ 0 & 0 & 1 \end{bmatrix}; \; M_6 = \begin{bmatrix} 1 & 0 & 0 \\ 0 & 1 & 0 \\ 0 & 0 & 1 \end{bmatrix}$$

The "beach ball" scheme corresponding to each of the previous mechanisms are:
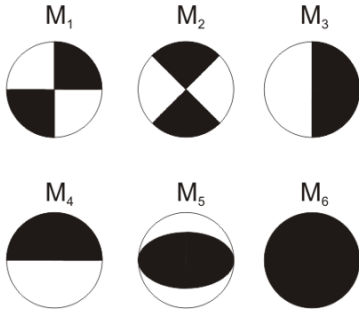
Using this representation, any moment tensor can be expressed as a linear combination of these elementary faults:

$$M_{ij} = a_n * M_n$$

Kikuchi and Kanamori (1991) show that the moment tensor (Mij) can be expressed as a function of a_n weighting factors as:

$$M_{ij} = \begin{bmatrix} a_2 - a_5 + a_6 & a_1 & a_4 \\ a_1 & -a_2 + a_6 & a_3 \\ a_4 & a_3 & a_5 + a_6 \end{bmatrix}$$

Since in this work we focus on tectonic earthquakes, and to reduce the non-uniqueness problem, we assume the isotropic component equal to zero; thus, previous equation is reduced to:

$$M_{ij} = \begin{bmatrix} a_2 - a_5 & a_1 & a_4 \\ a_1 & -a_2 & a_3 \\ a_4 & a_3 & a_5 \end{bmatrix}$$

Equation 1, using the moment tensor described above, is linearly inverted for the entire three-component broadband displacement waveforms (Dreger and Helmberger, 1993) to obtain Mij.

1 GREEN'S FUNCTIONS

The Green's functions were precomputed for each event-station combination in a discrete mesh using the frequency wavenumber method (Saikia, 1994), assuming a layered half space model without lateral velocity variations (Fukuyama *et al.*, 1999). are calculated every 5 km for a horizontal mesh from a distance of 5 to 1500 km. In depth direction, the mesh spacing is 2 km in a range of 2 to100 km; for deeper locations, the mesh spacing is every 5 km until 200 km depth (see Figure 2 for a sketch). Velocity model proposed by Campillo, *et al.* (1996) (Table 1) is used in computing.

Table 1: Velocity model used for the computation of Green's Functions (Campillo *et al.*, 1996).

Layer	Thickness, km	α , km/s	β, km/s	ρ, gr/cm³
1	5.0	5.36	3.10	4.45
2	12.0	5.72	3.30	4.72
3	28.0	6.50	3.75	5.33
Half Space	∞	8.23	4.50	6.66

As discussed in the next section, in order to minimize finite source effects, among other considerations, we filtered data in 3 different frequency bands related to the initial magnitude (see Table 2; Fukuyama *et al.*, 1999; Fukuyama and Dreger, 2000). Therefore, all Green´s function calculated for each pair of horizontal distance and depth are also filtered in same specific bands. The pre-computed Green´s function library consists of more than 60,000 files.
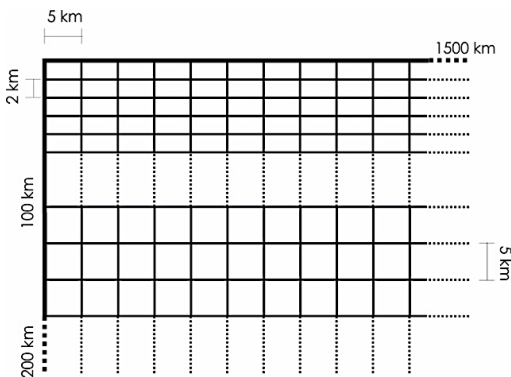
Figure 2. Sketch of the mesh used to compute Green´s function. Each Green's function has been calculated in the intersection point of the mesh, both horizontally and in depth. Notice, that the step is 5 km apart at depth > 100km.

59

Table 2: Minimum and maximum epicentral distance, filter bandwidth and data length as a function of initial magnitude reported by SSN.

Magnitude range	Epicentral distance range (km)	Frequency range (Hz)	Data length from initial time (seconds)
$4.0 \leq M < 5.0$	30 - 450	0.02 - 0.10	150
$5.0 \leq M < 6.5$	100 - 600	0.01 - 0.05	180
$6.5 \leq M < 7.5$	400 - 995	0.005 - 0.02	240
$M \geq 7.5$	500 - 1500	0.005 - 0.02	360

2 SELECTION OF STATIONS, FILTER BAND AND DATA LENGTH

As mentioned before, we analyzed a large database of regional earthquakes, which requires an automatic procedure based on specific criteria to select records for inversion. The selection criteria are a combination of rules based on the following:

1) Data integrity: An automatic procedure checks the integrity of the data in these aspects:
    a) Use of records from stations included in a list of valid stations (i.e. those that meet the conditions described in Table 2).
    b) Sufficient data length for inversion of the three components (N-S, E-W, Z).
    c) Pole-zero file valid for the date and time of the earthquake.
2) Point source approximation: In order to avoid finite source effects, we apply the following criteria based on the magnitude reported by SSN:
    a) From the list of stations available, we choose stations sufficiently far to approximate the event as a point source (Table 2).
    b) To pre-process observed data, we apply a specific filter related with magnitude and, therefore, related to epicentral distance. It is important to emphasize that the filter bands are the same used in the pre-calculated Green´s function library of synthetic seismograms. The filter bands have been taken from Fukuyama *et al.* (1999).
    c) Signal/noise ratio: This ratio decreases with distance and depends on the magnitude of the event. We do not choose the records of stations located too far from the event location, based on magnitude.

Taking into account above considerations, we choose, as a function of the initial magnitude, a combination of parameters to compute MTS: (a) minimum and maximum epicentral distance, (b) filter bandwidth, and (c) record length. In Table 2 we summarize the values of parameters.

The schematic representation of Table 2 corresponds to Figure 3. This figure shows a set of doughnuts whose center coincides to the epicentral location. The shaded area is the zone

fulfilling parameters described in Table 2. The stations located inside this region will be the subset of valid stations.

The stations located inside the doughnuts holes are discarded. Inner and outer radii are determined by a specific magnitude range, and observed data and synthetics are bandpass filtered in the corresponding interval.

In Figure 3, we plot doughnuts for 5 arbitrary locations. Even in places where the density of stations is poor (doughnut number 2 of Figure 3), the algorithm should be able to find solutions for small events (M < 5.0). For this configuration, MTS for large events could be computed for any epicentral location. On the other hand, an example of a coverage problem is shown in Figure 3B. For events with magnitude $5.0 \leq M < 6.5$, located in the northern zone of Baja California peninsula (doughnut No. 1), the availability of valid stations to compute MTS depends strongly on the epicentral location.
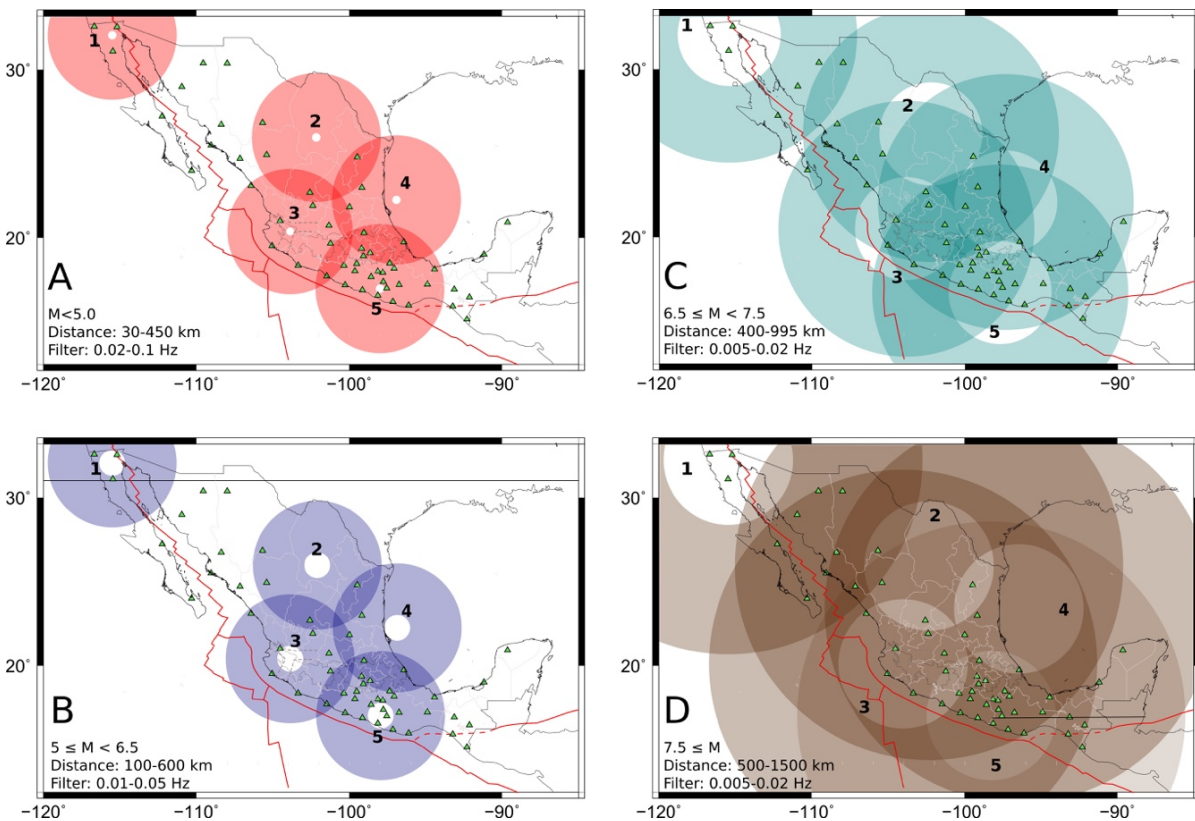
Figure 3. Schematic representation of parameters used to choose valid stations (for 5 arbitrary locations) and filter bandwidths to pre-process data and compute Green's functions.

3 Automatic process

Since we had to run the same procedure for more than 20,000 events, we developed a set of computational programs to automate the analysis of each event of the catalog. For further reference to the procedure described here we use the acronym AMTP (Automatic Moment Tensor Procedure).

The entire AMTP is summarized in Figure 4 by means of a flowchart. In this figure, we present 2 flowcharts, the main process (Figure 4A) and the sub-process of station selection (Figure 4B).

If data records are not available for any valid station and/or data are incomplete or corrupted in one of the three components, the event is discarded from the inversion.

After several tests, we choose to perform inversion with combinations of three stations at each time. Using fewer stations reduce the reliability of the solution, and use of more stations increase the computing time of procedure and reduces the possibility of finding a well fitted solution.

If records from more than 3 valid stations are available, then the strategy proposed by Fukuyama *et al.* (1999) and Kubo *et al.* (2002) for the inversion consists of selecting the closest stations falling in the epicentral range, according to the criteria listed in Table 2.

An important disadvantage of this strategy is that selected stations could be geographically concentrated in a narrow segment. Solutions obtained for this kind of configuration could be biased, even when data and synthetics are well matched at the three stations. A good azimuthal distribution reduces non-uniqueness problems and increases the reliability of the solution, but the fit between the data and synthetics could be poor. We propose to use a hybrid strategy, which, although implies a larger computational cost, increases the possibility to find a solution with a good azimuthal coverage and small misfit.

From the list of valid stations, we compute all the possible combinations without repetition of three stations. For each combination a grid search in depth is performed. The algorithm computes the MTS inversion for different depths (± 30 km, according to Figure 4a). For each combination, the algorithm store only the solution with the largest variance reduction (VR) defined as:

$$\sum_i w_i \int \left(1 - \frac{\left(s_i(t) - o_i(t) \right)^2}{|s_i(t)||o_i(t)|} \right)$$

where si(t) and oi(t) are the synthetic and observed waveforms, respectively, and wi is a weighting function proportional to the epicentral distance (Fukuyama et al., 1999).

Starting process
SSN: hypocentral location and magnitude

Copy in work directory and unzip the corresponding GF (taking account initial magnitude, see Table 2).

Stations Selection *

Combinations of 3 stations (SC triplets).
Compute azimuth weights.

Preprocess signal:
Deconvolution
Rotation
Get displacement (integer signal)
Filter in specific band

i = 1

Best solution with triplet i and j depth

i = i+1

Use first triplet

j = 0

i > sc

NO

j = j+1

moment tensor invesion

j > dd
dd: different depths

YES

NO

YES

Best MTS

Update database
Web page publication

A

Start station selection:

k = 1

Read new station from the valid, apriori list

In function of magnitude, the stations is into distance range

NO

YES

station data exists

NO

YES

Length record is enough

NO

YES

Pole-zero file response exists

NO

YES

Save the station in a useful subset

k = k +1

k > st
st: total stations availables in network

NO

YES

go back to principal process

B

Figure 4. Flow chart of the entire AMTP. A) General flow chart. The process starts with the SSN information of hypocenter, magnitude and origin time. The flow chart shows the iterative loop in triplet station combinations, and for each one trying different depths (± 30km; read detail in text). B) Flow chart to show the procedure to select station combination, taking azimuthal coverage into account.

Finally, to choose the selected combination, we weight VR with a function which depends on azimuthal coverage of the combination. For a three station scenario, the ideal azimuthal coverage (minimum gap) has stations 120° from each other; this implies that the absolute value of the azimuth differences between each station $\Delta\phi$ (cover area) is 160° in average ($\Delta\phi = \left[\frac{(|\phi_1 - \phi_2| + |\phi_1 - \phi_3| + |\phi_2 - \phi_3|)}{3}\right]$). Therefore, the worst scenario is with three aligned stations, $\Delta\phi = 0°$ (see Figure 5).
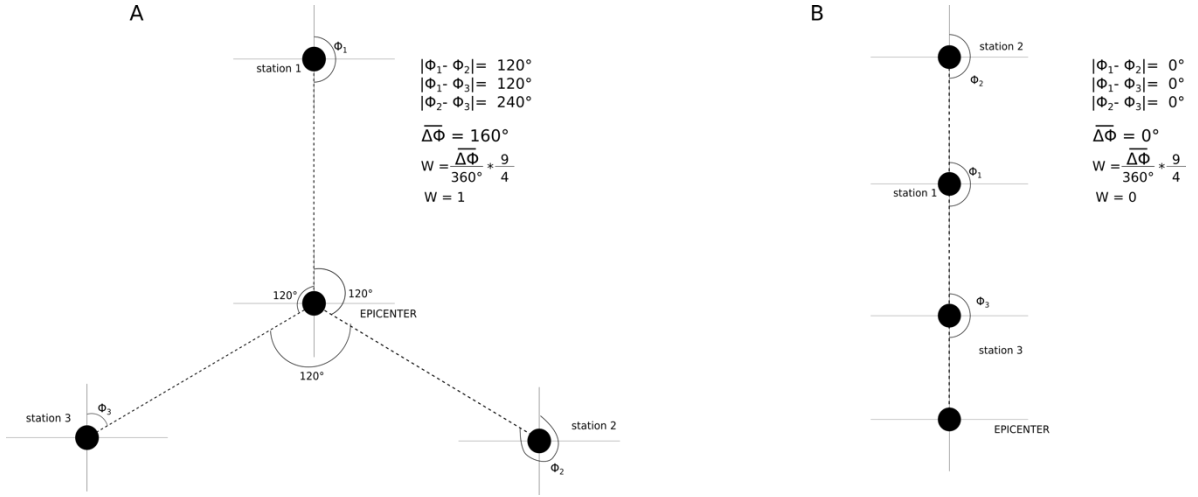
Figure 5. Schematic consideration to calculate azimuthal weight.

We choose a linear function between 0.5 and 1 for $0° \leq \Delta\phi \leq 160°$:

$$W = \frac{\Delta\phi}{320} + 0.5 \tag{2}$$

Our selected combination is one that maximizes the product: VR*W.

The scalar seismic moment, double-couple orientation components (DC) and the percentage of the compensated linear vector dipole (CLVD) are obtained from the tensor; the isotropic component of moment tensor is constrained to be zero.

RESULTS

The AMTP yields a database of 8,081 MTS which represents 36.7% of the total of the input catalog. Many events were discarded in the seismic record selection since their length did not fit Table 2 criteria. As mentioned before, the procedure starts with events reported with magnitude M ≥ 4.0, but the AMTP computes more than 1,000 events with Mw < 4.0.

All the MTS are stored into a directory structure. For each MTS there is one directory. The convention to name directories is: yyyy_mo_dd_hh_mm: where yyyy are four digits for year; mo, two digits for month; dd, two digits for day: hh, two digits for hour; and, mm, two digits for minutes.

The MTS directory consists of a set of files, which are: (1) plot of the best MTS; (2) ascii file with all the parameters estimated for MTS (e.g. the best depth, each element of moment tensor, fault plane solution, VR value, Mw, scalar seismic moment, among others); (3) list of available stations, following the doughnut criteria; (4) list of triplets of station combinations.

In Table 3, we list four events which we use to provide examples of the results obtained by AMTP. In this table are included the number of available stations, the Mw from AMTP, and Mw reported by GCMT, VR and CLVD values are also reported. We also list the parameters reported by the SSN. The geographic location of each event, listed in Table 3, is shown in Figure 1. Figure 6 shows typical output information from AMTP.

Table 3: Events used to provide example about the information generated by AMTP (Figure 6). These events are representative for the possible solution obtained by AMTP. The events are sorted by date.

Event number	Date yyyy_mm_dd	Origin time hh:mm:ss	Hipocentral location			Depth AMTP, km	Depth GCMT, km	M SSN	Mw AMTP	Mw GCMT	AMTP		Number of available station
			Latitutde °N	Longitude ° E	Depth SSN km						CLVD %	VR %	
1	2001-10-08	3:39:19	16.94	-100.14	4	8	15	6.1	5.8	5.8	21	73.37	9
2	2001-12-28	17:11:23	17.09	-93.89	202	180	N/A	4.3	5	N/A	59	8.3	4
3	2007-05-23	19:09:14	21.93	-96.14	16	44	24	5.5	5.7	5.6	76	54.22	8
4	2014-04-18	14:27:21	17,011	-101.46	18	18	18.9	7.2	7.1	7.3	25	88.76	17
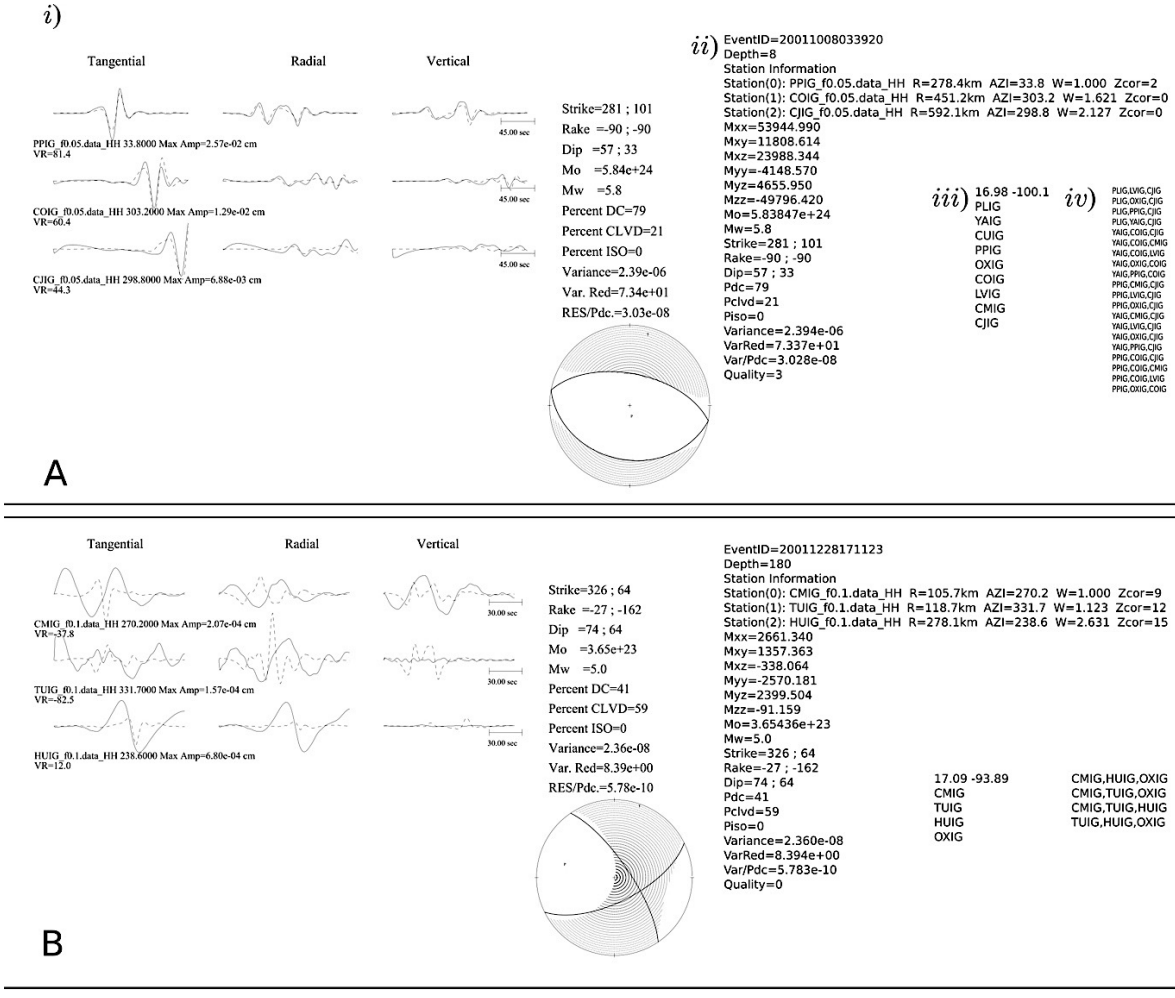
Figure 6. Output examples from the AMTP. For each event the figure shows: i) Typical output plot. ii) The ascii file with all the parameters obtained in the inversion. iii) Available stations list. iv) Maximum triplet station combinations. (A) The event corresponds to event 1 of Table 3. This event represents a small shallow earthquake located in a very densely instrumented zone. (B) Example of solution of a small, deep earthquake located in a zone with sparse station distribution, few available stations, poor VR values (event 2 of Table 3).

Panel C

Tangential   Radial   Vertical

DHIG_f0.05.data_HH 239.6000 Max Amp=3.27e-03 cm
VR=41.3

PPIG_f0.05.data_HH 219.8000 Max Amp=5.80e-03 cm
VR=56.9

PLIG_f0.05.data_HH 222.5000 Max Amp=3.52e-03 cm
VR=59.9

45.00 sec

Strike=12 ; 280
Rake =-169 ; -11
Dip =79 ; 79
Mo =3.94e+24
Mw =5.7
Percent DC=24
Percent CLVD=76
Percent ISO=0
Variance=4.18e-07
Var. Red=5.42e+01
RES/Pdc.=1.71e-08

EventID=20070523190914
Depth=44
Station Information
Station(0): DHIG_f0.05.data_HH R=350.5km AZI=239.6 W=1.000 Zcor=3
Station(1): PPIG_f0.05.data_HH R=409.3km AZI=219.8 W=1.168 Zcor=3
Station(2): PLIG_f0.05.data_HH R=525.8km AZI=222.5 W=1.500 Zcor=3
Mxx=23778.201
Mxy=-36330.843
Mxz=1629.187
Myy=-4606.420
Myz=2512.247
Mzz=-19171.781
Mo=3.94097e+24
Mw=5.7
Strike=12 ; 280
Rake=-169 ; -11
Dip=79 ; 79
Pdc=24
Pclvd=76
Piso=0
Variance=4.175e-07
VarRed=5.422e+01
Var/Pdc=1.709e-08
Quality=2

21.93 -96.14	
DHIG	DHIG,PPIG,YAIG
PPIG	DHIG,PPIG,LNIG
YAIG	DHIG,PPIG,PLIG
LNIG	DHIG,PPIG,OXIG
PLIG	DHIG,PPIG,MEIG
OXIG	DHIG,PPIG,MOIG
MEIG	DHIG,YAIG,LNIG
MOIG	DHIG,YAIG,PLIG
	DHIG,YAIG,OXIG
	DHIG,YAIG,MEIG
	DHIG,YAIG,MOIG
	DHIG,LNIG,PLIG
	DHIG,LNIG,OXIG
	DHIG,LNIG,MEIG
	DHIG,LNIG,MOIG
	DHIG,PLIG,OXIG
	DHIG,PLIG,MEIG
	DHIG,PLIG,MOIG
	DHIG,OXIG,MEIG
	DHIG,OXIG,MOIG

C

Panel D

Tangential   Radial   Vertical

ANIG_f0.02.data_HH 321.6000 Max Amp=1.78e-01 cm
VR=84.5

ZAIG_f0.02.data_HH 347.1000 Max Amp=1.60e-01 cm
VR=92.6

CMIG_f0.02.data_HH 89.9000 Max Amp=8.83e-02 cm
VR=81.9

45.00 sec

Strike=103 ; 298
Rake =81 ; 102
Dip =51 ; 40
Mo =5.89e+26
Mw =7.1
Percent DC=75
Percent CLVD=25
Percent ISO=0
Variance=2.45e-04
Var. Red=8.88e+01
RES/Pdc.=3.27e-06

EventID=20140418142723
Depth=18
Station Information
Station(0): ANIG_f0.02.data_HH R=551.0km AZI=321.6 W=1.000 Zcor=20
Station(1): ZAIG_f0.02.data_HH R=634.7km AZI=347.1 W=1.152 Zcor=18
Station(2): CMIG_f0.02.data_HH R=670.5km AZI=89.9 W=1.217 Zcor=26
Mxx=-4748055.413
Mxy=-1595642.914
Mxz=1434545.165
Myy=-1293756.710
Myz=-434933.800
Mzz=6041812.123
Mo=5.88945e+26
Mw=7.1
Strike=103 ; 298
Rake=81 ; 102
Dip=51 ; 40
Pdc=75
Pclvd=25
Piso=0
Variance=2.450e-04
VarRed=8.876e+01
Var/Pdc=3.274e-06
Quality=4

17.18 -101.19	
ANIG	ANIG,HUIG,LVIG
HUIG	ANIG,HUIG,ZAIG
LVIG	ANIG,HUIG,CMIG
ZAIG	ANIG,HUIG,TUIG
CMIG	ANIG,HUIG,TGIG
TUIG	ANIG,HUIG,MAIG
TGIG	ANIG,HUIG,PCIG
MAIG	ANIG,HUIG,LNIG
PCIG	ANIG,LVIG,ZAIG
LNIG	ANIG,LVIG,CMIG
CCIG	ANIG,LVIG,TUIG
THIG	ANIG,LVIG,TGIG
SCIG	ANIG,LVIG,MAIG
HPIG	ANIG,LVIG,PCIG
LPIG	ANIG,LVIG,LNIG
MYIG	ANIG,ZAIG,CMIG
	ANIG,ZAIG,TUIG
	ANIG,ZAIG,TGIG
	ANIG,ZAIG,MAIG
	ANIG,ZAIG,PCIG

D

Cont. Figure 6. (C) Event located in a very unusual location (event 3 in Table 3). This event presented a high CLVD but an acceptable VR value. (D) An example for a very high VR value (89%). It is a large event (Mw = 7.1) with many available stations (event 4 in table 3).

DISCUSSION

The MTS gives relevant additional information about earthquake source parameters. Nevertheless, if the MTS has a poor-quality resolution (low VR values), the information may not be reliable.

With the aim of evaluating the quality of the MTS database, we carried out a statistical comparison between the input magnitude and the magnitude reported by AMTP. Also, we analyzed the source parameters reported in the AMTP catalog with GCMT solutions.

1 Comparison between SSN and AMTP catalogs

Figure 7 shows a plot of the output magnitude (Mw) versus input magnitude (M) as reported by SSN. VR of the events are represented by the color of the symbol. This figure reveals a large disparity for some input magnitudes and the Mw obtained, especially for lower magnitudes. This disparity decreases if we consider a subset of events with VR ≥ 50% (Figure 7, middle). However, for higher VR (e.g. VR ≥ 70%) the correlation does not improve significantly. So, VR ≥ 50% provides a quality control to accept (or reject) MTS. Although the number of solutions decreases considerably, such VR criterion gives reliability to the final catalog. Figure 7 (right) shows the magnitude distribution for MTS for VR ≥ 50%.
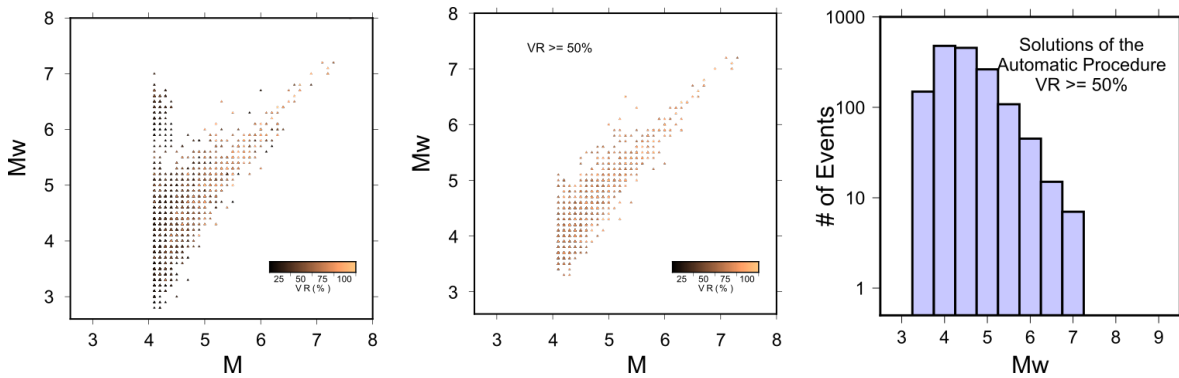

Figure 7. Left: Input magnitude (M as reported by SSN) vs. output magnitude (Mw) and its VR obtained for the Automatic Process. Center: Same as the left, but for events with VR ≥ 50%. The color of the symbol, in left and center frames, is related to the VR value. Right: Magnitude distribution of MTS with VR ≥ 50%.

For further analysis, we considered only the 1,521 events in which VR ≥ 50%. Here, we will refer these solutions as RMMT (Regional Mexican Moment Tensor).

To analyze a possible temporal evolution of the quality of solutions, in Figure 8 we show 1x1° regions with colors indicating percentage of solutions found in each square with VR ≥ 50%. We also include the location of stations (green triangles) operating at the end of each epoch. It is important to mention that solutions are cumulative. This figure shows that, at the beginning of the catalog (2000-2003), only some specific regions of the Pacific coast and the Tehuantepec Isthmus had reliable solutions. The map corresponding to 2000-2009 shows a remarkable change with respect to the previous one, especially in reliable solutions obtained for the Gulf of California and Central Mexico. The last frame shows the situation of the entire catalog (2000-2018) where we obtained reliable solutions for South and Central Mexico and the Gulf of California. In the supplementary material (appendix Figure S-1) we include a similar figure, but colors representing the quantity of solutions instead of quality for the RMMT catalog.
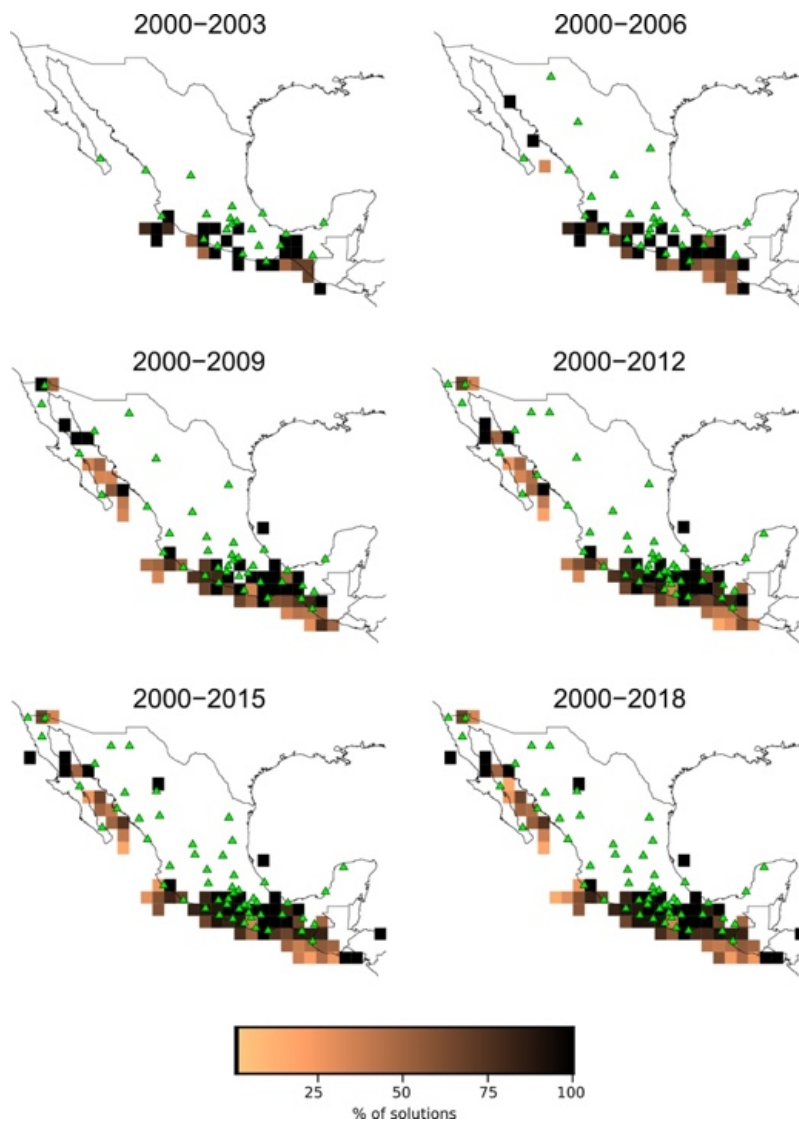
Figure 8. 1x1° regions with colors indicating percentage of solutions found in each square with VR ≥ 50%. Green triangles show the location of SSN stations. The figure shows a significant improvement in the reliable solutions.

Since hypocentral depth has larger uncertainty compared to epicentral location, the moment tensor inversion procedure includes a grid search around the reported depth by SSN (section 2.3). The best solution, after grid search, do not show a specific relation with input depth, except for the constraints imposed by the $\pm$ 30 km interval in the grid search (Figure 9). Although uncertainty in depth reported by SSN may be large, it is not possible to conclude whether the depth obtained by the procedure is better determined.
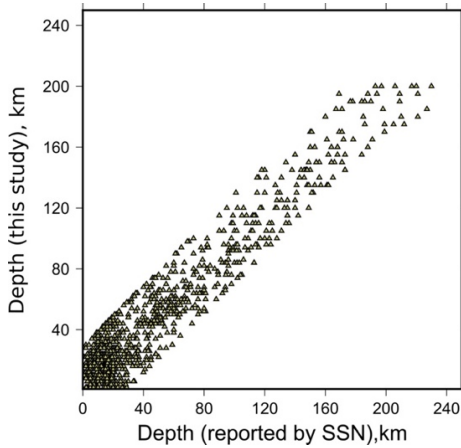
Figure 9. Depth from MTS (this study) *versus* the depth from SSN catalog.

2 Comparison between GCMT and RMMT catalogs

Of the 1,521 events of the RMMT catalog, 658 solutions are in common with the GCMT catalog (~43%).

The linear least squares fit between the datasets has a high correlation coefficient R2 of 0.92 (Figure 10). Although the R2 is good, the slope (1.044) and intercept (-0.38) of the equation suggests that there is a systematic underestimation of magnitude with respect to that reported by GCMT (Figure 11). We note that the disparity increases for magnitudes Mw ≤ 6.5. These differences have also been observed for smaller regional catalogs (e.g. Gasperini, *et al.*, 2012, Pondrelli *et al.*, 2016). There is not enough evidence to discriminate if the magnitudes of GCMT are overestimated or our determination of Mw is underestimated. A further analysis of Mw with independent data and/or other method could help solve this issue.
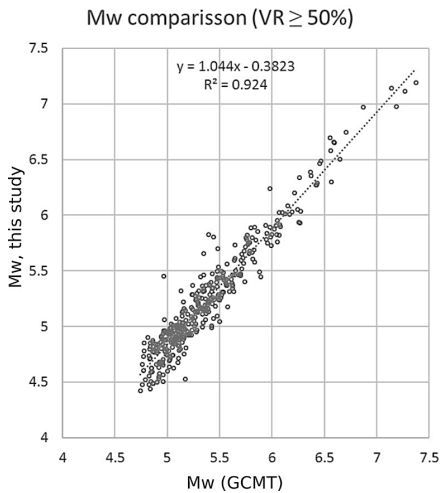
Figure 10. Comparison between Mw obtained in this study and reported by GCMT

The magnitude of events is only one of various parameters that we can get from MTS, and, as stated before, the correlation of magnitude between catalogs are acceptable. However, the aim is to get more source parameter information. In this sense, it is important to compare the entire moment tensor. To do this, we computed the Kagan angle, K (Kagan, 2007), which is the minimum 3D angle required to rotate the principal axes of one moment tensor onto other. In this case, K=0 would mean that the nodal plane reported by GCMT and in this study match exactly.
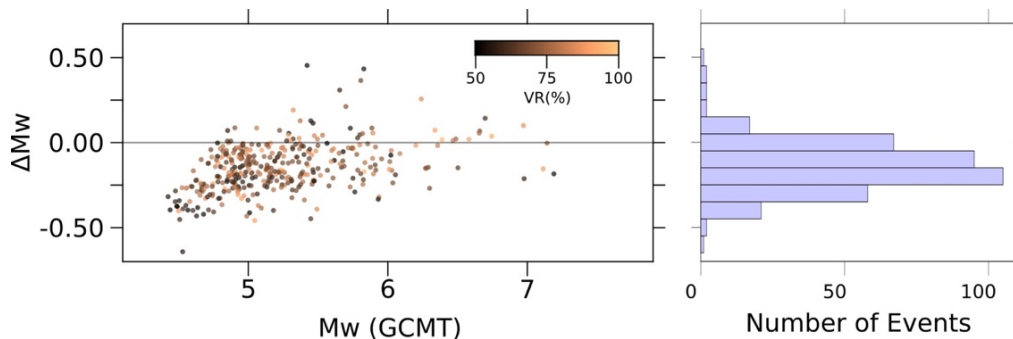
Figure 11. ΔMw vs Mw(GCMT) (left) and the histogram distribution of ΔMw (right). Most events in the RMMT catalog, seem to be underestimate by ~0.25. In the histogram, we can observe a normal distribution of ΔMw, with the mean value shifted ~0.25 from zero.

Figure 12A shows the geographical distribution of K value. Plots in Figures 12B and 12C (VR vs. K and Mw vs. K) show that there is no evident correlation between K and VR, or K and Mw.

As seen in Figure 12B (right), K is small for many events; 67% of the events have K ≤ 30°. The geographical distribution of events and K values show that the events with small K are located in central and southern Mexico, where the coverage of stations is better.

A comparison between the six independent components of the elements of the moment tensor was also carried out, and the corresponding figure can be found in the Appendix (S-2).

3 Tectonic Interpretation

Although the number of events in our RMMT catalog is only 8.6% of the total, it is still a useful tool to get a general picture of the different tectonic provinces of Mexico.

Figure 13 shows all the focal mechanism reported in the RMMT database. In this figure it is possible to distinguish different tectonic environments described briefly below.
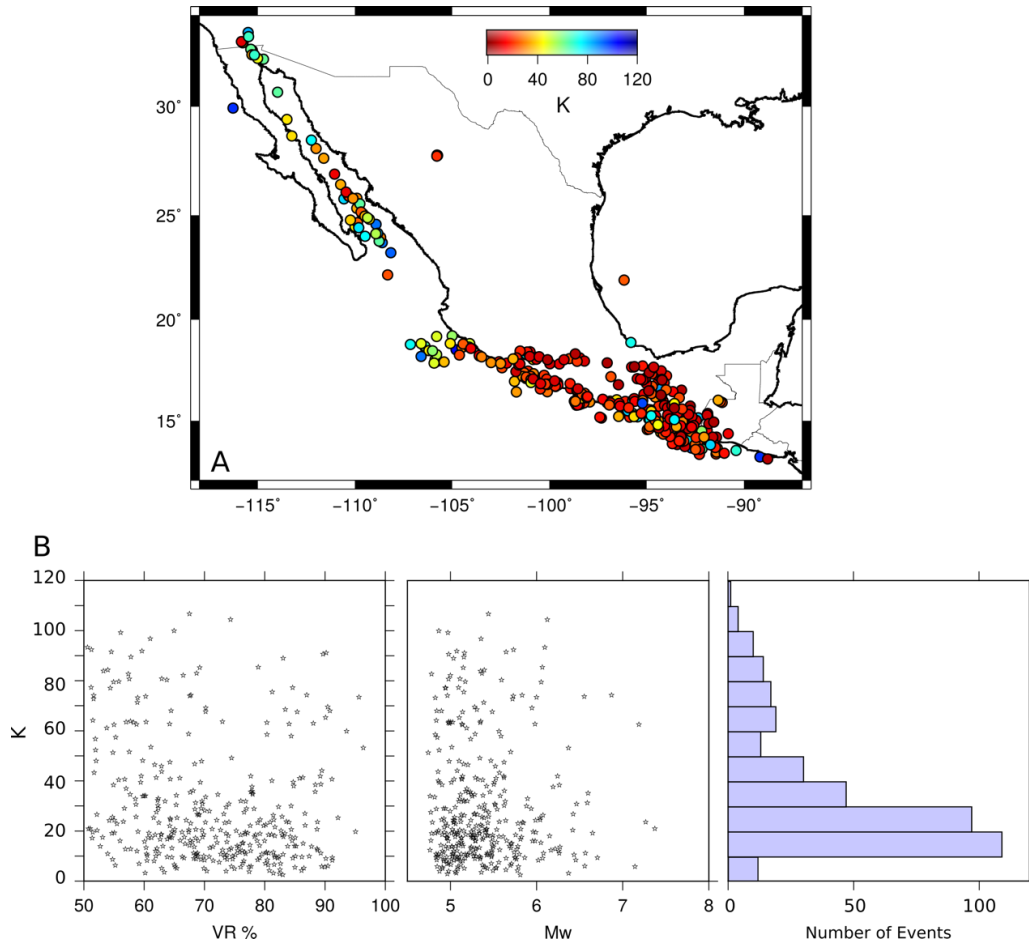
Figure 12. A) Geographical distribution of Kagan angle, K estimated for each event in the RMMT. The red color shows the best agreement (minimum K value). B) Left and center show relationship between K value and VR and Mw, respectively. B) Right shows distribution of K.

3.1 Pacific-North America boundary

The northwestern part of Mexico (Gulf of California) is characterized by a divergent-transcurrent tectonic regime. This type of plate boundary is mainly distinguished by shallow, normal and strike-slip faults. Most of the seismicity contained in our database for the Gulf of California and the Peninsula of Baja California shows shallow-strike slip and shallow-normal faults and a combination of both. However, in Figure 13 it is possible recognize some reverse faults suggesting a complex tectonic setting (e.g. Wong and Munguía, 2006; Mungía *et al.*, 2006).
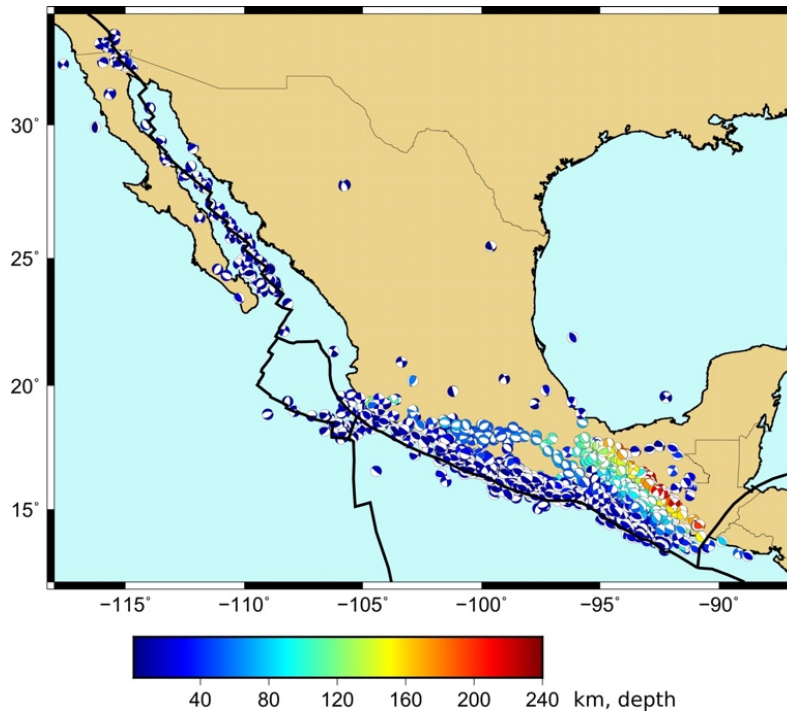
Figure 13. Focal mechanisms reported in the RMMT database. The color of beach balls is keyed to the depth obtained from grid search procedure.

3.2 Rivera-Cocos- North America tectonic contact

The Gordo Graben subduction under North America, a triple junction zone (Chapala, Colima and Tepic-Zacoalco rifts) and the Jalisco Block on the continental plate, together with the pure subduction of the Rivera plate, implies a very complex tectonic setting, which is in agreement with the focal mechanisms. It is possible to distinguish normal, strike-slip and thrust faults. The sparse station distribution in this area does not permit to obtain many MTS for medium or small earthquakes. The presence of many shallow earthquakes along the Rivera-Cocos limit is remarkable, indicating a large stress concentration. Another important feature is the intermediate-depth seismic activity (~100 km) very close to the coast. The occurrence of this type or earthquakes is in agreement with the geometry described by Pardo and Suárez (1995) and Manea *et al.* (2013).

3.2 Cocos-North America boundary

Seismicity at the boundary between Cocos and North America plates (offshore) shows predominance of thrust faults, but vertical and normal faults also occur. An example of this type of seismicity is the event number 1 in Table 3. Inland seismicity, in central and southern Mexico, is characterized by intermediate-depth normal faults occurring in the subducted Cocos plate. A sharp change in seismicity depths occurs to the east of 96° W, where earthquakes become deeper, indicating an abrupt change in the geometry of the subducted Cocos plate. An evident lack of seismicity is observed in a wide region between ~100-97° W and ~16-17° N where it is possible

to distinguish two different bands of seismicity. In this region, thrust shallow and steeply dipping thrust events are located close to the coast, and normal and deepest focal mechanism can be found in the second band of seismicity. The same observation was made by Pacheco and Singh (2010) from a very careful analysis of seismicity of this zone.

3.3 North America stable zone

Of special interest in the estimation of the probabilistic seismic hazard analysis (PSHA) are the non-clustered events in the Gulf of Mexico and northern Mexico. In this case, it is possible to distinguish shallow faults of different mechanisms.

Even if only the solutions for VR ≥ 60%, 70% and 80% are considered (appendix section, Figure S-3), the tectonic features observed remain the same.

DATABASE DESCRIPTION AND WEBPAGE

All the MTS that were calculated and yielded solution, independent of VR values, are saved in a database (mysql). In order to make this information accessible to public, we have developed a set of php scripts and a website: http://132.248.6.13/cmt. However, we consider important that the public database be only the RMMT catalog.

Inspired on the GCMT catalog, we offer four different format outputs:

a) Html columns with pictures of solutions;
b) CSV format with all the database information, including number of stations used during solution, VR value, tensor moment solution, etc.;
c) PSMECA format for GCMT convention;
d) PSMECA format for GCMT zero trace convention.

CONCLUSIONS

The main contribution of this work is the RMMT database, with more than 1,500 solutions for local events. For many of these events it is the only source of information. The criterion proposed to include the MTS in the RMMT gives reliability to the catalog, even when Mw estimated here is, on average, underestimated with respect to that reported by the GCMT.

The number and quality of MTS have been increased through time, in concordance with the SSN network development.

The number of solutions is significantly less than the number of events reported by SSN; the reason is that the records used for inversion have to fulfil several strict criteria. For example the length of the record: for the moment tensor inversion, we need at least 120 s; in contrast, for location estimation 30 s or one minute is enough.

In the geographical zones with a dense station coverage, there are more solutions and, proportionally, a better quality of resolution. In some areas, such as the Guerrero coast, there are many MTS with magnitude smaller than 4.0.

The events located in central-south Mexico show small K value between GCMT vs. RMMT.

The different tectonic environments of Mexico are well represented by the solutions reported in the RMMT. This permits identification of anomalous seismicity, that is, earthquakes that are not expected in the tectonic regime, for example the shallow, normal fault earthquake of October 8th, 2001 (Mw=5.8), or the event recorded at the Gulf of Mexico (May 23th 2007, Mw=5.7).

Database and free access via website could give an opportunity to get MTS of small to medium local earthquakes, useful information that is not available from international agencies.

The AMTP is a very useful tool to be continuously fed with new events and increase the RMMT catalog.

ACKNOWLEDGMENTS

REFERENCES

Campillo, M., S. K. Singh, N. Shapiro, J. F. Pacheco and Herrmann R. B., 1996. Crustal structure of the Mexican volcanic belt, based on group velocity dispersion. *Geofísica Internacional*, 35, 4, pp. 361-370.

DeMets, C., Gordon, R. G., and, Argus, D. F., 2010. Geologically current plate motions, Geophysical Journal International, 181, 1, pp. 1-80, doi: 10.1111/j.1365-246X.2009.04491.x

Dreger D.S. and Helmberger D., 1993. Determination of source parameters at regional distances with three-component sparse network data. *J. Geoph. Res.*, 98, B5, pp. 8107-8125, https://doi.org/10.1029/93JB00023.

Dziewonski A. M., Chou T. A., Woodhouse J.H., 1981. Determination of earthquake source parameters from waveform data for studies of global and regional seismicity. J. Geophys. Res., 86, pp. 2825-2852

Dziewonski, A.M. and Woodhouse J.H., 1983. Studies of the seismic source using normal-mode theory, in Kanamori, H. and E. Boschi, eds., Earthquakes: observation, theory, and interpretation: notes from the International School of Physics "Enrico Fermi" (1982: Varenna, Italy), North-Holland Publ. Co., Amsterdam, pp. 45-137.

Ekström, G., Nettles M., and Dziewonski A. M., 2012. The global CMT project 2004-2010: Centroid-moment tensors for 13,017 earthquakes. Phys. Earth Planet. Int., 200-201, pp. 1-9. doi:10.1016/j.pepi.2012.04.002

Franco-Sánchez S. I., Iglesias A., Pacheco J. F., Singh S.K., Fukuyama E., Pérez-Santana J. and Yi T., 2002. Inversión automática del tensor de momentos utilizando datos de la red de banda ancha del SSN. Geos, 22, 2, pp. 379.

Fukuyama, E., Ishida, M., Horiuchi, S., Inoue, H., Kubo, A., Kawai, H., Murakami, H., and Nonomura, K., 1999. NIED Seismic moment tensor catalogue, January-December, 1998 (Revised). Technical Note of the National Research Institute for the Earth Science and Disaster Resilience, 218.

Fukuyama, E. and Dreger D. S., 2000. Performance test of an automated moment tensor determination system for the future "Tokai" earthquake. Earth Planets Space, 52, pp. 383–392.

Gasperini P. Lolli B. Vanucci G., and Boschi E., 2012. A comparison of moment magnitude estimates for the European-Mediteranean and Italian regions. Geophys. J. Int., 190, pp. 1733-1745. https://doi.org/10.1111/j.1365-246X.2012.05575.x

Hayes, G.P., Rivera, L. and Kanamori, H., 2009. Source inversion of the W-Phase: real-time implementation and extension to low magnitudes, Seismol. Res. Lett., 80, pp. 817–822

Iglesias A., Franco-Sánchez S. I., and Rivet D., 2008. Sistema automático del cálculo de tensor de momentos sísmicos para sismos mexicanos. Geos, 28, 2, p. 229.

Kanamori H. and Rivera L., 2008. Source inversion of W-phase: Speeding up seismic tsunami warning. Geophys. J. Int., 175, pp. 222–238.

Kagan Y. Y., 2007. Simplified algorithms for calculating double-couple rotation. Geophys. J. Int., 171, pp. 411-418.

Kikuchi, M. and Kanamori H., 1991. Inversion of complex body waves III. Bull. Seism. Soc. Am., 81, pp. 2335-2350.

Kubo, A., Fukuyama E., Kawai, H. and Nonomura K., 2002. NIED seismic moment tensor catalogue for regional earthquakes around Japan: Quality test and application. Tectonophysics. 378, pp. 223-239.

Manea V., Manea M., and Ferrari L., 2013. A geodynamical perspective on the subduction of Cocos and Rivera plates beneath Mexico and Central America. Tectonophysics. 609. DOI: 10.1016/j.tecto.2012.12.039.

Munguía L., González M., Mayer S, and Aguirre A., 2006. Seismicity and state of stress in the La Paz–Los Cabos region, Baja California Sur, Mexico. Bull. Seism. Soc. Am., 96, pp. 624–636, doi: 10.1785/0120050114.

NCEDC, 2014 Northern California Earthquake Data Center. UC Berkeley Seismological Laboratory. Dataset. doi:10.7932/NCEDC.

Pacheco J.F. and Singh S.K., 2010. Seismicity and state of stress in Guerrero segment of the Mexican subduction zone. J. Geophys. Res. 10.1029/2009JB006453.

Pardo M. and Suarez G., 1995. Shape of the subducted Rivera and Coco plates in southern Mexico: Seismic and tectonic implications. J. Geophys. Res. 100, pp. 12,357-12,373.

Pasyanos, M., Dreger D., and Romanowicz, B., 1996. Toward real-time estimation of regional moment tensors, Bull. Seism. Soc. Am., 86, pp. 1255-1269.

Pérez-Campos, X., Espíndola V.H., Pérez J., Estrada J. A., Cárdenas Monroy C. , Bello D., González-López, González-Ávila D., Contreras-Ruiz-Esparza M.G., Maldonado R., Tan Y., Rodríguez-Rasilla I., Vela-Rosas M.A., Cruz J. L., Cárdenas A., Navarro-Estrada F, Hurtado A., Mendoza-Carvajal A. J., Montoya-Quintanar e., and Pérez-Velázquez M. A., 2018. The Mexican National Seismological Service: An Overview. Seismol. Res. Lett., v. 89, 2, pp. 318-323. https://doi.org/10.1785/0220170186.

Pondrelli, S., Di Luccio, F., Fukuyama, E., Mazza, S., Olivieri, M., and Pino N. A., 2003. Fast determination of moment tensor for the recent Molise (southern Italy) seismic sequence. Orfeus Electronic Newsletter, 5.

Pondrelli S. and Salimbeni S., 2015. Regional moment tensor review: An example from the European Mediterranean region. In Encyclopedia of Earthquake Engineering (pp. 1-15), http://link.springer.com/referenceworkentry/10.1007/978-3-642-36197-5_301-1, Springer Berlin Heidelberg, 2015.

Pondrelli S., Salimbeni S., and Perfetti P., 2016. Moment tensor solution for the Amatrice 2016 seismic sequence. Annals of geophysics, 59. DOI:10.4401/ag-7240.

Romanowicz, B., Pasyanos, M., Dreger, D., and Uhrhammer, R., 1993: Monitoring of strain release in central and northern California using broadband data. Geophys. Res. Lett., 20. pp. 1643-1646.

Rueda, J. and Mezcua J., 2005. Near-real-time seismic moment-tensor determination in Spain. Seismol. Res. Lett. 76, pp. 455-465.

Saikia, K.S., 1994. Modified frequency-wavenumber algorithm for regional seismograms using Filon's quadrature: modelling of Lg waves in eastern North America. Geoph. J. Int. 10.1111/j.1365-246X.1994.tb04680.x.

Sipkin, S.A., 1982. Estimation of earthquake source parameters by the inversion of waveform data: synthetic waveforms. Phys. Earth Planet. Inter., 30, pp. 242-259.SSN.

Servicio Sismológico Nacional de México, Instituto de Geofísica, UNAM (seismic records). doi:10.21766/SSNMX/SN/MX.

Wong V. and Munguía L., 2006. Seismicity, focal mechanisms, and stress distribution in the Tres Vírgenes volcanic and geothermal region, Baja California Sur, Mexico. Geofís. Int., 45, pp. 23-37.

Zúñiga, F. R., Pacheco, J. F., Guzmán-Speziale, M., Aguirre-Díaz,G. J., Espíndola, V. H., and Nava, E., 2003. The Sanfandila earthquake sequence of 1998, Queretaro, Mexico: activation of an undocumented fault in the northern edge of central Trans-Mexican Volcanic Belt, Tectonophysics, 361, pp. 229–238.

APPENDIX: SUPPLEMENTARY MATERIAL CAPTIONS:
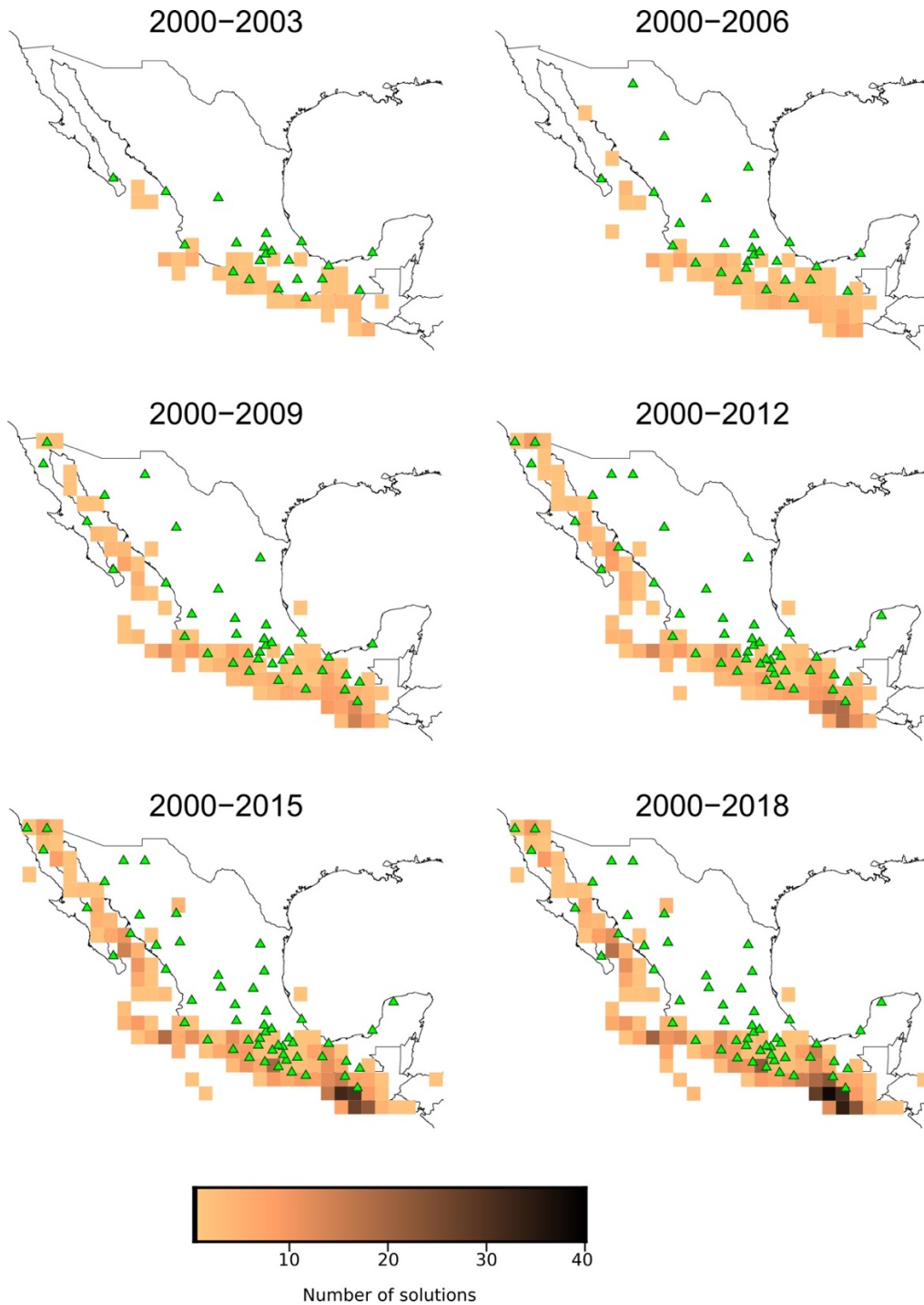
Figure S-1. 1x1° regions with colors denoting number of solutions found in each square. Green triangles show the location of SSN stations. The figure shows a substantial increase in number of MTS with time.
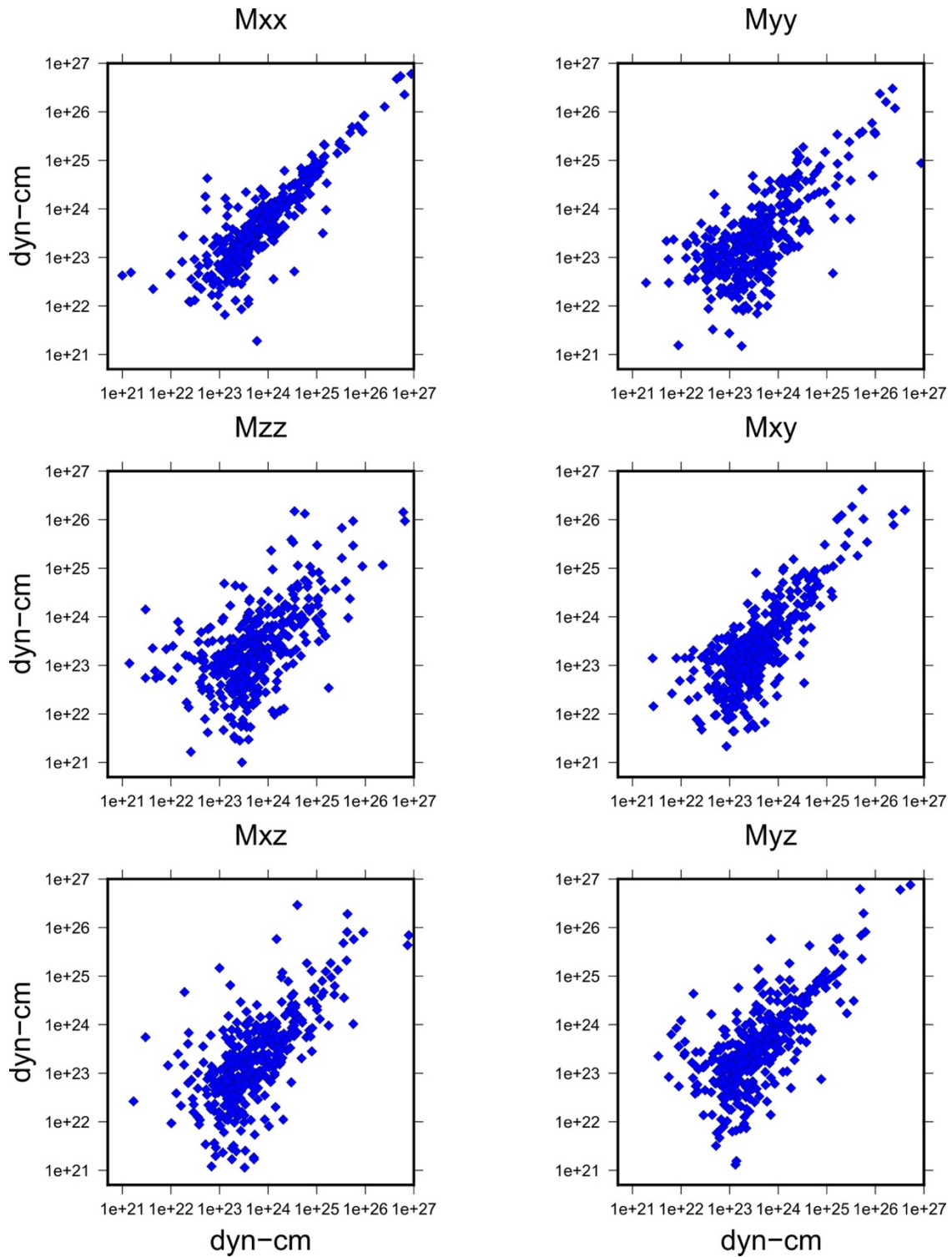
Figure S-2. Comparison of moment tensor components reported by GCMT vs RMMT catalogs.
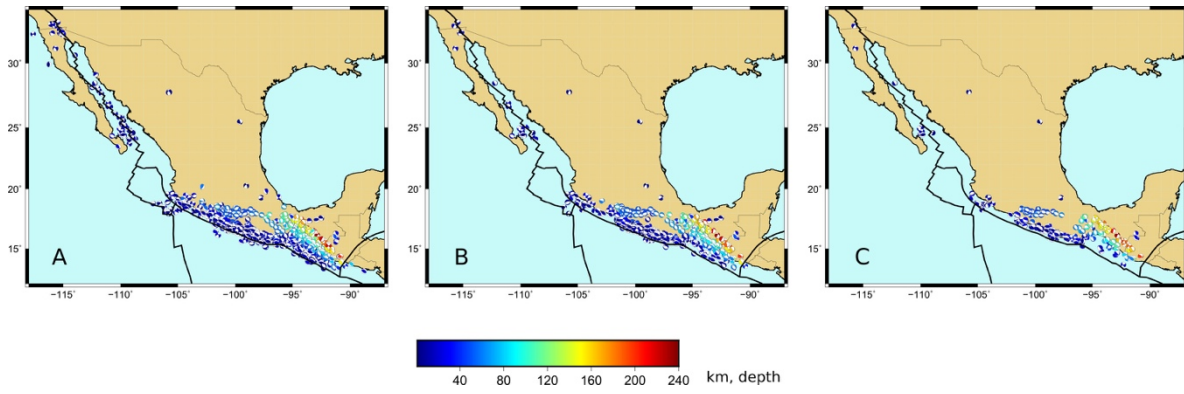
Figure S-3. Geographical distribution of MTS. The colors represent depth. (A) Solutions with VR > 60%. (B) Solutions with VR > 70%. (C) Solutions with VR>80%.

_____Original paper

Observed Seismic Intensities and Damage Pattern in Central Mexico during Intraslab Earthquakes of 1999 (Mw6.9) and 2017 (Mw7.1)

Danny Arroyo[1], Shri Krishna Singh[2], Mario Ordaz[3], Roberto Meli[3] and Mario Ramírez[1]

Resumen

El patrón y nivel de daño en la región de México Central durante el sismo de septiembre de 2017 Mw7.1 en Morelos-Puebla son diferentes a los observados durante el sismo de Tehuacán (Mw6.9) en 1999 a pesar de que ambos sismos intraplaca tienen magnitudes similares y profundidades focales comparables 57 km y 60 km, respectivamente. El sismo de 2017 causo claramente mas daño en la región de México Central. Los epicentros de ambos eventos están separados 127 km. Mediante el análisis de los registros sísmicos de México Central encontramos que el área expuesta a diferentes niveles de aceleración máxima del suelo y velocidad máxima del suelo es comparable para los dos eventos. Por ejemplo, el área expuesta a aceleraciones máximas del suelo mayores a 150 cm/s^2 es de 12,700 km^2 para el sismo de 1999 y 15400 km^2 para el sismo de 2017. La forma de los contornos de intensidades y localización epicentral sugiere una ruptura bilateral para el evento de 2017 y una ruptura con directividad hacia el norte para el sismo de 1999. Los cocientes espectrales para los dos eventos revelaron una fuente más energética hacia el norte para el sismo de 1999 que para el sismo de 2017 lo cual es consistente con resultados reportados previamente de directividad en la ruptura. Se concluye que la distinta localización de los dos eventos junto con la diferente distribución de las poblaciones, monumentos históricos y el incremento de población desde 1999 fueron las principales causas de la diferencia de los daños entre los dos eventos.

Palabras clave: sismo 2017 Morelos-Puebla, sismo 1999 Tehuacán, registros de movimiento fuerte, mapas de intensidades

Abstract

The pattern and level of damage during the 2017 Morelos-Puebla (Mw7.1) earthquake in central Mexico differ from those observed during the 1999 Tehuacán (Mw6.9) earthquake. Although these two intraslab events had similar magnitudes and depths, 57 km and 60 km respectively,

*Corresponding author
aresda@correo.azc.uam.mx

[1]Departamento de Materiales
Universidad Autónoma Metropolitana

[3] Instituto de Ingeniería
UNAM

the 2017 earthquake caused significantly more damage in central Mexico. The epicenters of the two events were separated by 127 km. From the analysis of strong-motion recordings in central Mexico, we find that the areas within different PGA and PGV contours during the two earthquakes are roughly equal. For example, PGA contour of 150 cm/s2 encloses 12,700 km2 and 15,400 km2 during the 1999 and 2017 events, respectively. The shape of the contours and the location of the epicenter suggests a bilateral rupture during the 2017 earthquake and a rupture directivity to the north for the 1999 earthquake. Spectral ratios of the two earthquakes reveal a more energetic 1999 source to the north than that of 2017 which is consistent with the previously reported rupture directivity. This leads us to conclude that the distinct locations of the two earthquakes along with uneven density of population, dwellings, and historical monuments, and demographic increase since 1999 were the principal causes of the difference in damage during the two earthquakes.

Key words: 2017 Morelos-Puebla Earthquake, 1999 Tehuacán Earthquake, strong ground motion records, intensity maps

INTRODUCTION

Intraslab earthquakes in central Mexico occur in the subducted Cocos plate at a depth of ~ 40 to 80 km and involve normal faulting. The recent intraslab earthquake of 19 September 2017 (Mw7.1) was located near the border of the states of Morelos and Puebla (18.41 °N, -98.71 °E; depth H = 57 km) (Figure 1). It caused severe damage in central Mexico and Mexico City. Several towns in the epicentral region were almost completely destroyed. Extensive damage was reported in the states of Morelos and Puebla. In Mexico City 44 buildings collapsed and approximately 600 buildings were severely damaged. It was the second most destructive earthquake in the history of the city, next only to the 1985 Michoacán (Mw8.0) earthquake. The PGA at CU, a strong-motion station in the hill-zone of Mexico City that has been in continuous operation for the last 54 years, was 57 cm/s2, the highest ever recorded. In comparison, the PGA at CU during the 1985 earthquake was 29 cm/s2.

It is well known that intraslab earthquakes pose significant seismic hazard to cities in central Mexico (see, e.g., Singh *et al.*, 2018 for a brief review). In 1931 a Mw7.8 earthquake devastated the city of Oaxaca; in 1973 a Mw7.0 earthquake damaged some cities of Veracruz; a Mw7.0 earthquake in 1980 caused severe damage in the state of Oaxaca; in 1999 a Mw6.9 earthquake caused damage to the city of Tehuantepec and the states of Puebla and Morelos and Oaxaca; and the great intraslab earthquake of 8 September 2017 (Mw8.2), which occurred off the coast of Chiapas and Oaxaca, caused wide-spread destruction to the coastal towns of these states. Figure 1 shows epicenters of 4 significant, recent intraslab earthquakes in and near Morelos-Puebla region (06/07/1964, Mw7.3; 24/10/1980, Mw7.0; 15/06/1999, Mw6.9; 19/09/2017, Mw7.1). The earthquake of 2017 is the closest, reliably located, intraslab earthquake to Mexico City (Singh *et al.*, 2018).

The 2017 and 1999 earthquakes were well recorded at many stations in central Mexico and Mexico City. The epicenters of the two events are separated by 127 km; the epicentral distance to CU in Mexico City from the 2017 and 1999 earthquakes are 113 km and 218 km,

respectively (Figure 1). Here we analyze the accelerograms of the two earthquakes to relate the recorded seismic intensities with observed damage patterns. We then investigate whether the location alone can explain the difference in the pattern and level of damage during the two earthquakes or other factors also played a role. Our focus is central Mexico excluding Mexico City.
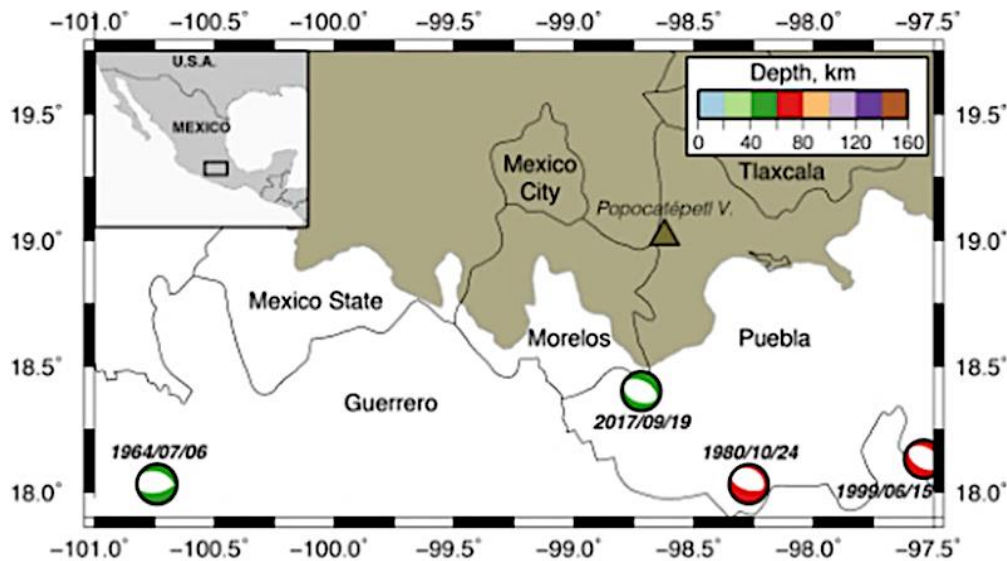
Figure 1. Map of central Mexico showing epicenters and focal mechanisms of four, recent significant intraslab earthquakes in the region. The epicenter of the 2017 earthquake is closer to Morelos and Mexico City than the other earthquakes.

RECORDED STRONG GROUND MOTIONS

The 1999 earthquake was recorded in 33 stations on firm soil sites listed (Table 1). The largest recorded intensities (PGA= 184 cm/s_2 and PGV=17 cm/s) were observed at CSER station located roughly 100 km from the epicenter. We constructed PGA and PGV contours via the Bayesian Kriging technique proposed by Kitanidis (1986). We first used the ground motion prediction equation (GMPE) proposed by Garcia *et al.* (2005) for Mexican intraslab earthquakes to generate prior median values of the intensities at different sites on a grid; these values were then updated with intensities listed in Table 1 via Bayes theorem. It is worth noting that 1999 data were used to construct the Garcia's GMPE therefore it fits well the 1999 data. We excluded recordings in Mexico City from the analysis because of the well-known large site effects. Figures 2a and 3a show PGA and PGV contours during the 1999 earthquake. The contours are elongated towards northwest from the epicenter suggesting rupture propagation towards this direction. This source directivity was previously documented from an analysis of the recorded waveforms (Singh *et al.*, 1999) as well as from PGA contours constructed using an interpolation technique based solely on the recorded data. The figures also show towns in the State of Puebla with population larger than 15,000.

Table 1. Recorded PGA and PGV during the 1999 earthquake

Station	Lat	Long	R, km	PGA*, cm/s2	PGV*, cm/s	Station	Lat	Long	R, km	PGA*, cm/s2	PGV*, cm/s
AGCA	16.837	-99.645	275	10.11	0.80	RABO	18.569	-98.445	124	141.59	11.01
ATYC	17.213	-100.432	331	7.25	0.54	RIOG	16.014	-97.439	245	5.71	0.46
CHFL	17.969	-97.866	73	106.96	10.69	SMLC	16.655	-96.729	196	13.29	0.67
COMD	18.122	-100.524	323	15.56	0.89	SMR2	16.774	-99.438	261	7.57	0.75
COPL	16.611	-98.984	239	9.59	0.81	TAMA	16.261	-96.575	240	6.68	0.54
COYC	16.998	-100.090	307	8.32	0.66	TEAC	18.618	-99.454	219	33.30	2.68
COYQ	17.380	-101.057	389	9.14	0.50	TNLP	18.096	-99.561	224	35.79	2.31
CSER	18.989	-97.377	112	184.47	17.39	UNIO	17.988	-101.811	458	2.43	0.38
JAMI	16.284	-97.821	218	17.18	0.55	VIGA	16.759	-99.233	246	17.73	0.81
LANE	15.940	-97.180	255	5.94	0.47	VNTA	16.914	-99.819	286	6.06	0.49
OCLL	17.037	-99.879	285	7.81	0.55	YAIG	18.862	-99.067	191	43.16	3.42
OMTP	16.689	-98.398	197	21.11	0.61	CUER	18.984	-99.230	211	42.99	2.89
OXLC	17.065	-96.703	160	20.74	1.80	LVIG	19.723	-96.418	218	4.91	0.54
PANG	15.667	-96.491	303	4.51	0.28	MEZC	17.930	-99.591	228	27.44	1.62
PET2	17.535	-101.263	406	3.41	0.40	OXIG	17.072	-96.733	158	28.53	1.40
PHPU	19.044	-98.168	135	170.34	15.81	BHPP	19.109	-98.227	143	58.55	5.51
POZU	17.090	-99.598	257	18.42	0.71	PLIG	18.392	-99.502	218	20.88	1.49

 * PGA and PGV are the geometric mean of two horizontal components

The 2017 earthquake was recorded at 64 firm soil sites (Table 2). The highest intensities were observed at FTIG station (PGA= 369 cm/s2 and PGV=12.7 cm/s) located roughly 100 km southeast from the epicenter. The PGA and PGV contours, shown in Figures 2b and 3b, were constructed following the same procedure as described before. The contours for this earthquake are elongated in the NW-SE direction with the epicenter in the middle, suggesting a bilateral rupture. Slip distribution on the fault plane of this earthquake has been mapped from the inversion of teleseismic waveforms (L.Ye, personal communication, 2018) as well as from the inversion of regional data (Melgar *et al.*, 2017; A. Iglesias, personal communication, 2018). Not surprisingly, directivity is not discernible in the teleseismic inversion because of the relatively small magnitude of the event. Inversion by Melgar *et al.* suggests a directivity towards NW, which is contrary to Iglesias´ inversion that supports rupture propagation predominantly towards SE.

The area under PGA contour of 150 cm/s2 in 2017 is roughly 15,400 km2, slightly greater than the corresponding area of 12,700 km2 in 1999. This PGA contour during 2017 covers 75%, 20%, 4% and 2% of the states of Morelos, Puebla, Guerrero, and Oaxaca, respectively; the corresponding numbers during 1999 are 0%, 35%, 0%, and 2%. In 2017, 24%, 45%, 17%, and 14% of the total area under the 150 cm/s2 contour fall in the states of Morelos, Puebla, Guerrero, and Oaxaca, respectively (Table 3). In contrast, in 1999 the total area under the same PGA contour was distributed as follows: 0%, 84%, 13%, and 3% in the states of Morelos, Puebla, Oaxaca, and Veracruz, respectively.

Table 2. Recorded PGA and PGV during the 2017 earthquake

Station	Lat	Long	R, km	PGA*, cm/s2	PGV*, cm/s	Station	Lat	Long	R, km	PGA*, cm/s2	PGV*, cm/s
hlig	17.830	-97.800	128	227.98	14.29	cuer	18.984	-99.230	102	158.94	18.88
hmtt	17.800	-98.560	90	170.55	12.10	ftig	17.908	-98.133	100	368.52	12.51
phpu	19.040	-98.170	107	141.73	9.84	lvig	19.723	-96.418	287	1.84	0.37
ppig	19.070	-98.630	94	112.62	12.96	plig	18.392	-99.502	101	61.45	5.85
tlig	17.560	-98.570	111	110.70	3.90	pzpu	19.055	-98.227	105	105.35	13.67
teju	18.900	-100.160	172	83.30	3.53	rabo	18.569	-98.445	81	141.50	7.99
meig	17.920	-99.620	124	74.59	2.42	sxpu	19.040	-98.215	104	127.41	18.99
tpig	18.420	-97.360	153	71.34	7.41	tgbt	16.777	-93.089	624	0.88	0.12
acp2	16.870	-99.890	219	35.36	1.35	thez	18.478	-97.383	151	157.41	11.34
oxlc	17.070	-96.700	265	22.52	1.34	tnlp	18.096	-99.561	112	58.25	3.62
atyc	17.210	-100.430	233	18.69	0.67	pb1	18.240	-98.700	81	201.21	7.19
coyc	17.000	-100.090	222	18.32	0.86	pb2	18.330	-98.260	81	223.43	15.12
oxbj	17.070	-96.720	264	18.11	1.45	gr	18.330	-99.190	81	258.29	7.86
vnta	16.910	-99.820	212	10.63	0.89	huig	15.768	-96.108	407	4.11	0.32
pet2	17.540	-101.260	292	10.03	0.44	peig	15.999	-97.147	320	10.88	0.92
xala	19.530	-96.900	234	8.28	1.50	pnig	16.392	-98.127	239	6.63	0.82
caig	17.050	-100.270	231	8.07	0.42	toig	18.096	-97.065	186	19.36	1.40
unio	17.990	-101.810	336	6.08	0.42	txig	17.254	-97.761	172	41.42	5.20
urua	19.420	-102.070	375	6.04	0.86	yoig	16.858	-97.546	219	9.43	1.63
nilt	16.570	-94.620	482	5.98	0.29	cdgu	19.700	-103.448	521	1.95	0.70
pang	15.670	-96.490	389	4.68	0.51	coll	19.191	-104.681	637	1.38	0.17
acam	20.040	-100.720	284	4.48	1.31	jami	16.284	-97.821	260	15.30	1.43
ziig	17.610	-101.460	309	4.19	0.50	lane	15.948	-97.187	322	5.50	0.77
cmig	17.090	-94.880	434	2.99	0.35	lmpp	19.001	-98.182	103	37.13	3.33
dhig	20.300	-99.040	221	2.73	0.80	nux2	17.217	-100.791	263	7.66	0.51
coma	19.330	-103.760	544	2.23	0.44	ocll	17.037	-99.879	204	17.49	0.88
chpa	16.250	-93.910	565	2.16	0.27	pbp2	19.045	-98.208	105	95.98	15.31
mmig	18.290	-103.350	493	2.14	0.34	rpig	21.885	-99.983	413	4.41	1.29
tuig	18.030	-94.420	458	2.07	0.33	sjal	18.585	-103.670	527	3.31	0.22
yaig	18.862	-99.067	85	202.00	13.00	slu2	17.281	-100.935	273	11.78	0.53
arig	18.281	-100.344	182	31.44	1.73	smlc	16.655	-96.729	292	10.50	1.11
chfl	17.969	-97.866	116	76.38	7.30	tama	16.261	-96.575	333	7.30	1.00

* PGA and PGV are the geometric mean of two horizontal components

1999

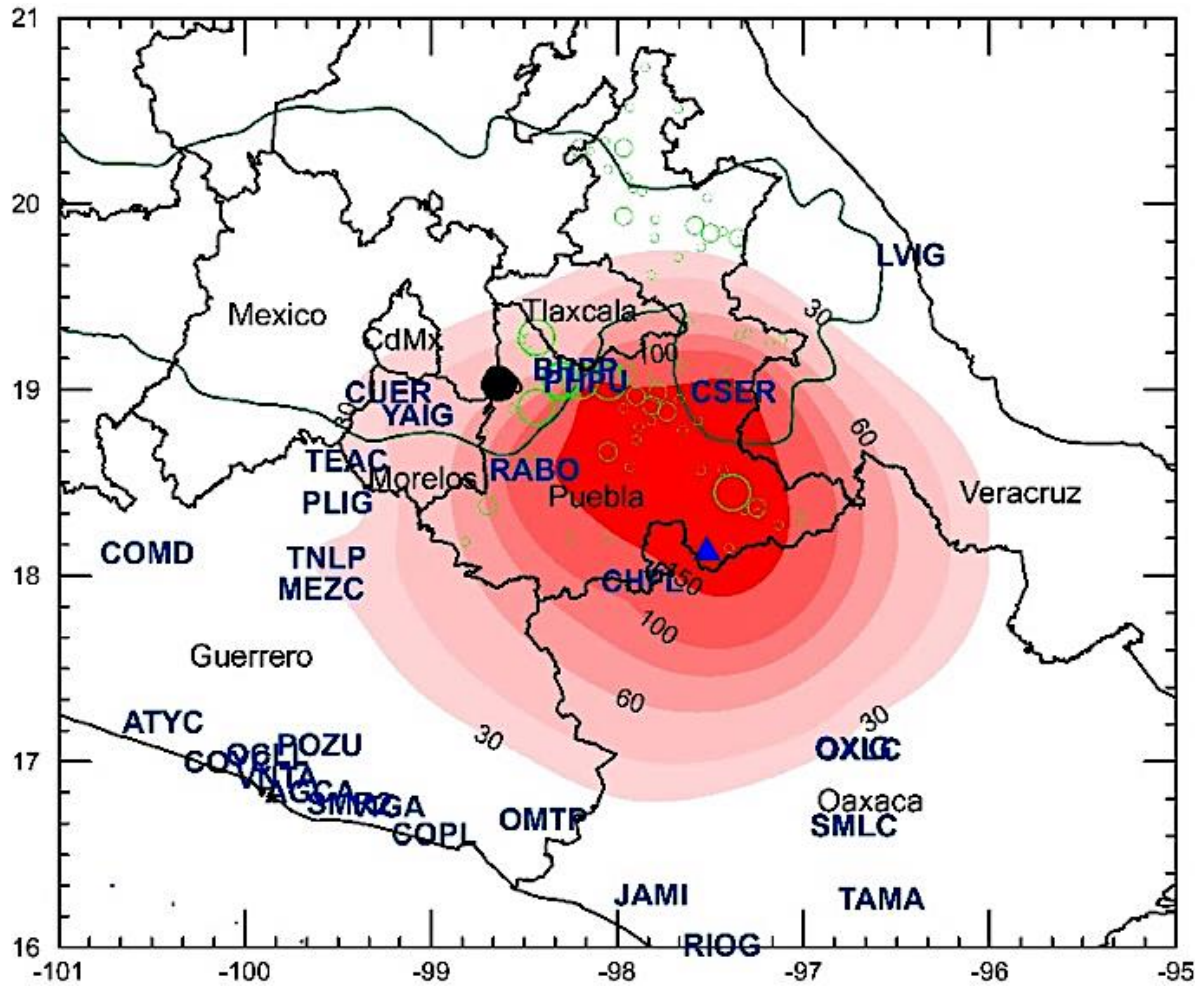Figure 2. a) PGA contours during 1999 (Mw6.9) earthquake (top), and b) 2017 (Mw7.1) earthquake (bottom) in cm/s2. Triangle: epicenter. Station code is given by letters and is plotted at its location. Black dot: Popocatepetl volcano. Green contour: Mexican Volcanic Belt. Large, medium and small green circles are towns in Puebla with population > 100,000, 50,000 - 100,000 and 15,000 - 50,000, respectively
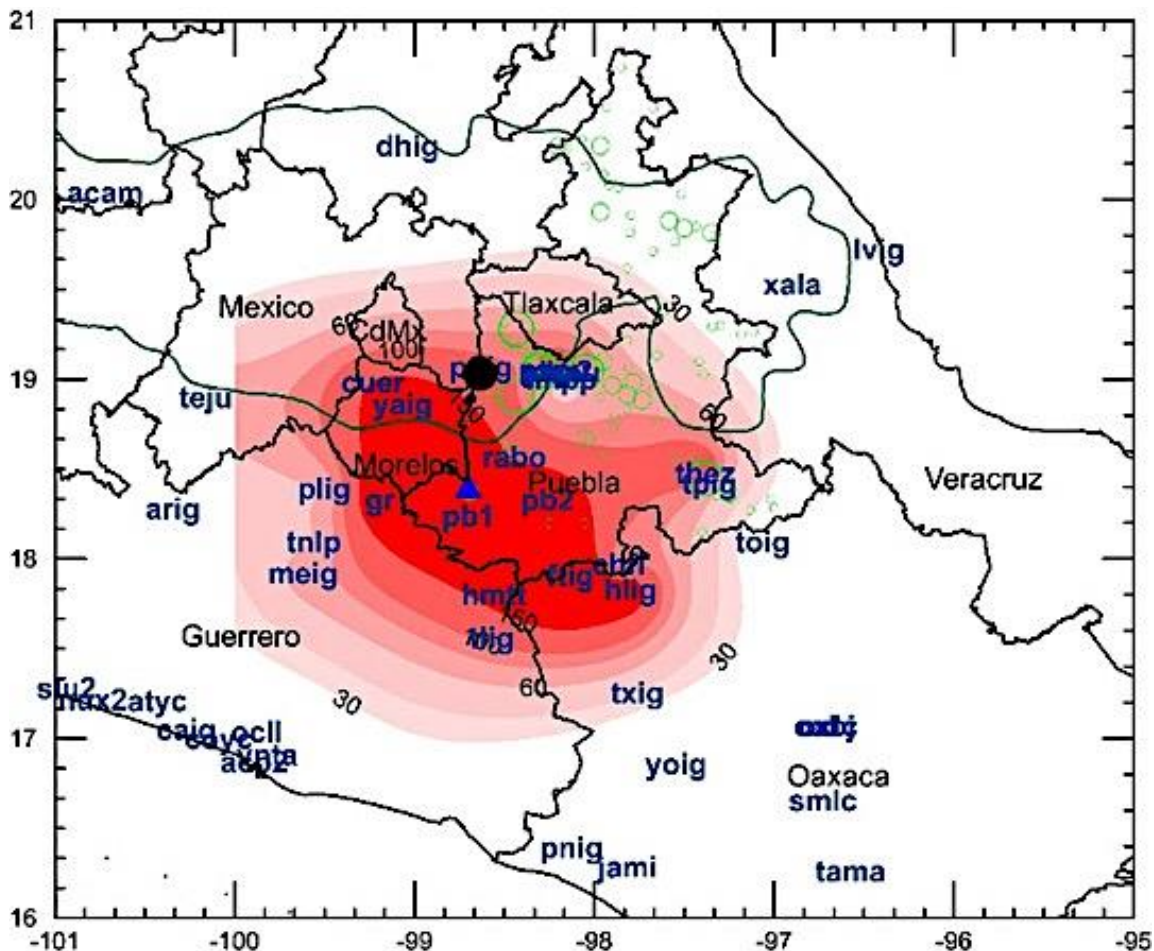
2017

Figure 2 b)

Table 3. Percentage of total area and population under PGA contour of 150 cm/s^2 in different states in central Mexico during the 1999 and 2017 intraslab earthquakes. Total area under this contour was 1.27x10^4 km^2 and 1.54x10^4 km^2 during 1999 and 2017, respectively.

State/ area	Year	Population	% of total area under 150 cm/s^2 contour	Inhabitants under 150 cm/s^2 contour
Morelos / 4.96x10^3 km^2	1999	-	0	0
	2017	1.97x10^6	24	1.46x10^6
Puebla / 3.429x10^4 km^2	1999	5.00 x10^6	84	1.57x10^6
	2017	6.37 x10^6	45	1.30x10^6
Guerrero/6.36x10^4 km^2	1999	-	0	0
	2017	3.65 x10^6	17	1.23x10^5
Oaxaca/9.38x10^4 km^2	1999	3.44x10^6	13	6.05x10^4
	2017	4.10x10^6	14	9.42x10^4
Veracruz/7.28x10^4 km^2	1999	6.91x10^6	3	3.62x10^4
	2017	-	0	0

Estimated number of persons living within PGA contour of 150 cm/s^2: 1.67x10^6 in 1999 and 2.98x x10^6 in 2017.

SEISMIC INTENSITIES AND REPORTED DAMAGE

From the PGA contours shown in Figures 2 to 3, assuming uniform density of population and construction throughout the region, we expect:

     a) Extensive damage in the State of Morelos in 2017 but little damage in 1999.

     b) More damage in the State of Puebla and the city of Puebla during 1999 than in 2017.

     c) Lesser damage to the south of the epicenter in 1999 but nearly equal damage to NW and SE of the epicenter in 2017.

     d) Marginally more damage during 2017 than in 1999.

1999

Figure 3. a) Same as Figure 2 but for PGV in cm/s

2017

Figure 3) b)

A detailed description of the damage during the 1999 earthquake is given by Alcocer *et al.* (1999). Information on damage during 2017 in central Mexico has been compiled by E. Reinoso and his colleagues (personal communication, 2018). A preliminary estimation of damage to historical monuments is available to us (Secretaría de Cultura, 2018). The municipalities receiving funds for reconstruction from the government program for natural disasters (FONDEN) in 1999 and 2017 should, in principle, provide information on the damage. In 2017, the municipalities receiving funds, generally, fall within the PGA contour of 60 cm/s2 (Figure 4). However, the correlation between PGA and municipalities receiving funds from FONDEN during the 1999 earthquake is poor (Figure 4). This may be a consequence of the fact that FONDEN became operational in 1999. The criteria for assigning funds in 1999 may have been different from those in 2017.
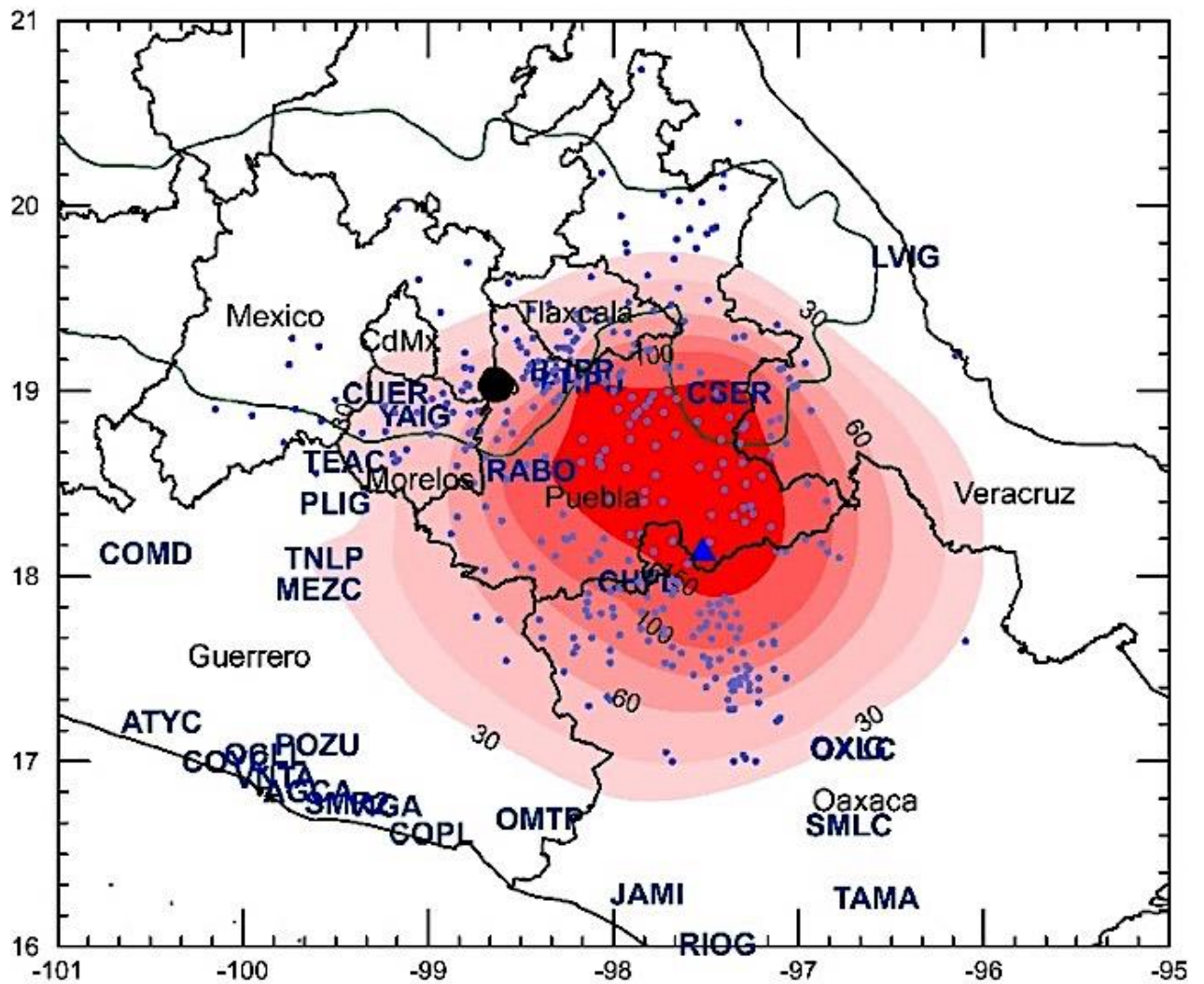
1999

Figure 4. a) PGA contours in cm/s2 for 1999 (top) and b) 2017 (bottom) earthquakes and municipalities that received funds for reconstruction from FONDEN.

2017

Figure 4. b)

Since the available damage reports during the two earthquakes were not elaborated using the same criteria, it is difficult to relate seismic intensity contours of the two earthquakes with ensuing reported damages. Even so, a rough comparison is possible. There were no fatalities reported in Morelos in 1999 (Alcocer *et al.*, 1999); in 2017 there were 74. Although 45 fatalities are reported in Puebla in 2017 and only 15 in 1999 (Alcocer *et al.*, 1999), it is generally accepted that the damage in the state was more severe in 1999 than in 2017. This is also in agreement with damage to historical monuments (churches, monasteries, and government buildings) during the two earthquakes. The 1999 and 2017 earthquakes caused damage to 1124 and 448 historical monuments, respectively (Secretaría de Cultura, 2018). Less damage to the south of the 1999 epicenter is partly supported by the geographical distribution of municipalities receiving funds from FONDEN (Figure 4).

If we assume that the area of severe damage is proportional to the area under the PGA contour of 150 cm/s2 then we expect only marginally more damage in 2017 than in 1999. Yet, there is consensus that the damage in 2017, even excluding Mexico City, was far greater than in 1999. One possibility is that the area of high seismic intensities in 2017 coincided with that of high density of population and historical monuments. Since areas under PGA and PGV contours during the two earthquakes are roughly similar, the difference in their source strength is unlikely to be the cause of much higher damage in 2017. Even so, we first explore, in more detail, the source characteristics of the two earthquakes and its effect on the damage pattern. We then return to distinct locations of the two earthquakes along with uneven density of population, dwellings and historical monuments, and demographic increase since 1999 as the principal causes of the difference in damage during the two earthquakes.

POSSIBLE SOURCE EFFECT ON GROUND MOTION AND DAMAGE DISTRIBUTION

PGA and PGV values as function of minimum distance to the rupture area, R, during the 1999 and 2017 earthquakes are illustrated in Figure 5. The figure also includes predicted median values from the ground motion prediction equation by Garcia *et al.* (2005), henceforth called the G05 model. In general, PGA and PGV values are similar for the two earthquakes. G05 model fits well the PGA data but underestimates observed PGV, except for the 1999 earthquake at sites at R greater than about 200 km located to the south of the epicenter. We note that PGA and PGV for 2017 at sites north and south of the epicenter follow the same attenuation trend. During 1999, however, the PGA, but especially PGV values, are greater to the north and smaller to the south with respect to the trend. This is in agreement with bilateral and northward rupture propagation during 2017 and 1999 earthquakes, respectively, mentioned before. PGA at CU, a firm site in the UNAM campus, Mexico City, during the two earthquakes are in agreement with G05 model but PGV values are much higher than predicted by the model.
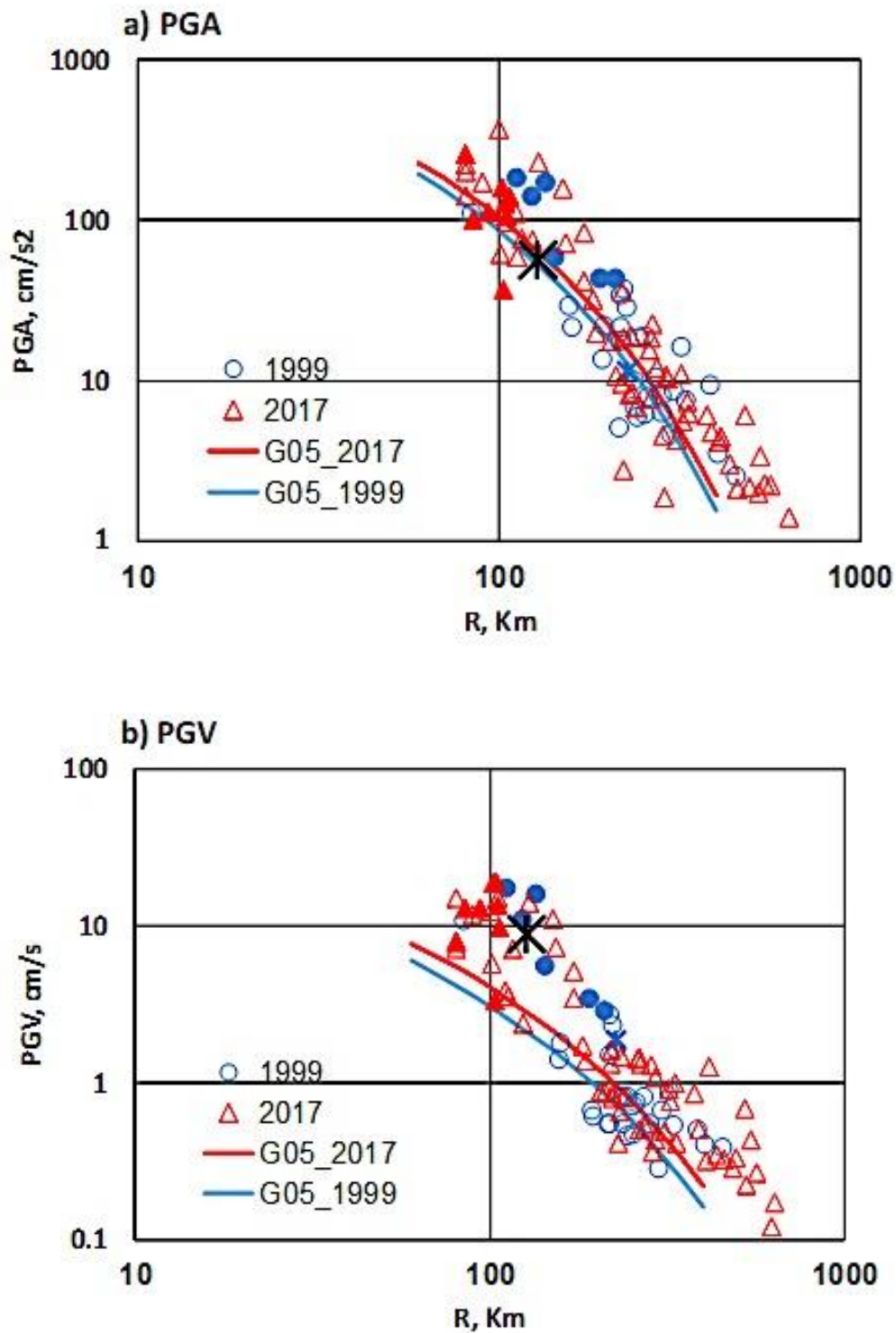
Figure 5. a) PGA and b) PGV during the 2017 and 1999 earthquakes as a function of minimum distance to the fault, R. The filled symbols are sites to the north of the epicenter and the star is CU station in Mexico City. G05: prediction from GMPE of García *et al.* (2005). Observed PGV is greater than G05 model prediction, except at sites south of the 1999 epicenter.

Several stations recorded the ground motion during both earthquakes. This permits a comparison of Fourier amplitude spectra of the two earthquakes and, hence, probe their relative source strength. For the comparison, we reduced the spectra of the 1999 earthquake to the same hypocentral distance as the 2017 earthquake by correcting for geometrical spreading, G(R), and quality factor, Q. Following García *et al.* (2004), we take G(R) = 1/R and Q=251f0.58. The geometric mean of two horizontal components of the reduced spectra are shown in Figure 6. The reduced spectra at sites PHPU, YAIG, RABO and PLIG are greater in 1999 than 2017 at frequencies close to 1 Hz. At CUER, the two reduced spectra are similar or somewhat smaller in 1999. At CHFL the reduced spectrum in 1999 is slightly smaller than in 2017. The spectra in Figure 6 are consistent with rupture propagation to the north in 1999.
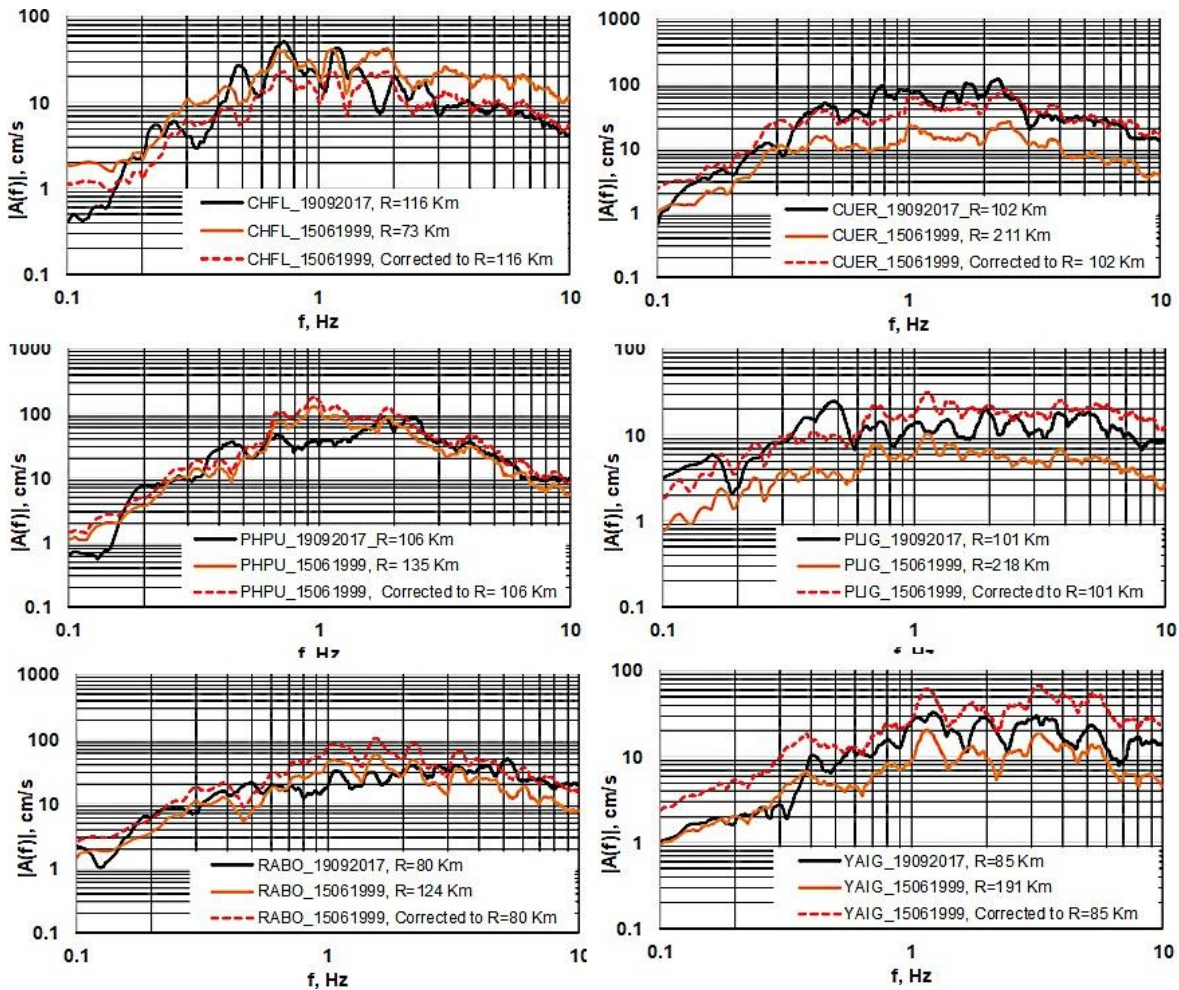

Figure 6. Fourier acceleration amplitude spectra at some stations that recorded the 2017 and 1999 earthquakes. The 1999 spectra, reduced to the same distance at which the 2017 earthquake was recorded by correcting them for geometrical spreading and anelastic attenuation, are also shown.

From the above, we expect the reduced 1999 spectrum at CU in Mexico City to be higher than the 2017 spectrum. Figure 7, however, shows just the opposite; the 2017 spectrum near 1 Hz is significantly higher than the 1999 spectrum. The reason, as discussed by Shapiro *et al.* (2002), is that the seismic waves from 1999 earthquake reaching CU traversed below the active

Popocatepetl Volcano and suffered high attenuation. During the 2017 earthquake the wave path to CU does not pass through the volcano (Figures 1, 2, and 3). A test of this hypothesis is provided by the 2017 recordings at DHIG and PNIG that are located at roughly the same distance (~ 230 km) from the epicenter (Figure 2). The path to DHIG, however, crosses the volcano. As expected, the spectrum at DHIG relative to PNIG is depleted at f > 0.8 Hz (Figure 8).

To summarize, we find that the 1999 source was more energetic to the north of the epicenter than the 2017 source. It follows that the significantly larger damage in central Mexico during 2017 as compared to 1999 can´t be attributed to the source. The 2017 earthquake produced severe damage to certain zones in Mexico City while the 1999 earthquake was only moderately felt. The difference in the damage can be attributed to the fact that the 2017 earthquake was closer to Mexico City (R=127 km) than the 1999 earthquake (R=226 km). High attenuation due to wave path crossing Popocatepetl during 1999 was also partly responsible. The 2017 earthquake occurred closer to more densely populated towns and cities of the State of Morelos than the 1999 earthquake. Next, we explore the effect of location of the earthquakes on the damage.
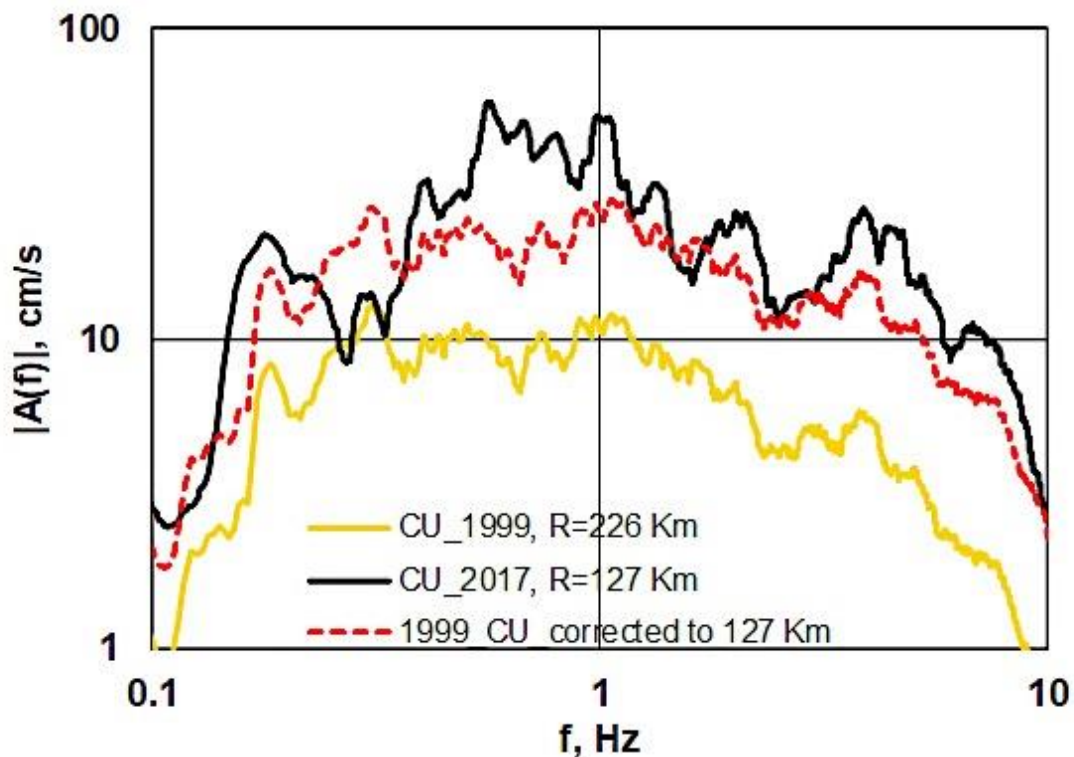

Figure 7. Fourier amplitude acceleration spectra at CU in Mexico City during the 2017 and 1999 earthquakes. The station is located at hill zone. The 1999 spectrum was corrected for geometrical spreading and anelastic attenuation to reduce it to the same distance at the which the 2017 earthquake was recorded.
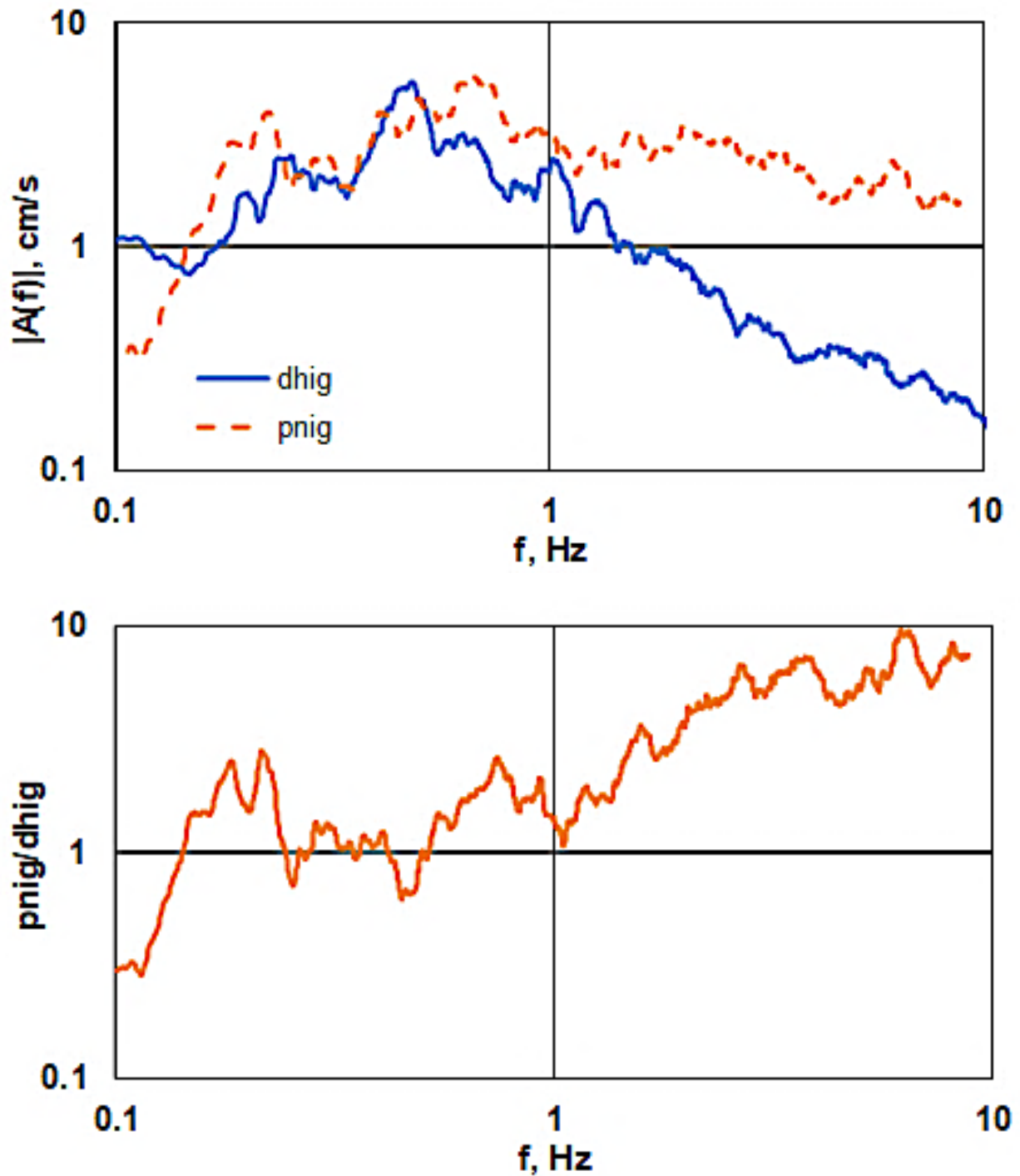
Figure 8. a) (Left) Fourier amplitude acceleration spectra at stations DHIG and PNIG during the 2017 earthquake (see Figure 1 for location of the stations). The stations are located at nearly the same hypocentral distance from the earthquake (~230 km). b) (Right) PNIG to DHIG spectral ratio.

EFFECT OF LOCATION OF THE 1999 AND 2017 EARTHQUAKES ON THE DAMAGE IN CENTRAL MEXICO

We assume that the damage is proportional to the area enclosed in the PGA contour of 150 cm/s2. As mentioned earlier, these areas were 1.24x104 and 1.54x104 km2 during 1999 and 2017, respectively. The distribution of these areas in different states is given in Table 3, along with the total area and number of inhabitants of each state. A demographic increase of 1.65% per year has been assumed in the estimation of number of inhabitants. As given in the table, the total number of inhabitants within the PGA contour of 150 cm/s2 during 1999 and 2017 were ~ 1.67x106 and 2.98x106, respectively. These simple calculations suggest roughly two times more damage in 2017 as compared to 1999. Note that the affected number of inhabitants in 2017 in the states of Morelos and Puebla are 1.46x106 and 1.30x106, respectively. This implies only slightly higher damage in Morelos than in Puebla. E. Reinoso (personal communication, 2018), however, reports 1432 and 464 damaged structures in Morelos and Puebla, respectively. Clearly, our estimation of damage is over simplified. It, nevertheless, provides a gross overview of the damage.

CONCLUSIONS

From the analysis of strong-motion recordings during the 1999 and 2017 intraslab earthquakes in central Mexico, we conclude that: (1) The rupture during 1999 propagated towards north while the directivity was bilateral during 2017. (2) PGA and PGV contours during the two earthquakes had similar areas, suggesting roughly similar source strength. PGA and PGV as function of distance were also similar during the two earthquakes. However, PGV values during 1999 at stations to the south, in the direction away from rupture propagation, were, relatively, smaller. (3) The GMPE for Mexican intraslab earthquakes (García at al., 2005) predicts well the observed PGA during the two earthquakes but grossly under estimates PGV. (4) At a finer level, the 1999 source was somewhat more energetic to the north of the epicenter than that of 2017. (5) Path effect may significantly affect the ground motion and, hence, the damage pattern

In view of the above, we would have expected a similar level and pattern of damage during the two earthquakes or even larger damage to the north of the epicenter during the 1999 earthquake. In reality, the pattern and level of damage during the 2017 differ from those observed during the 1999 and the 2017 earthquake caused significantly more damage in central Mexico. This leads us to conclude that the distinct locations of the two earthquakes along with uneven density of population, dwellings, and historical monuments in the region, and the demographic increase since 1999 were the principal causes of the difference in damage during the two earthquakes. Changes in construction quality may also have played a role in the observed differences. Finally, path effect may significantly affect the ground motion and, hence, the damage pattern. This is especially true for waves traversing Popocatepetl volcano which greatly attenuates of high-frequency shear waves.

ACKNOWLEDGMENTS

REFERENCES

Alcocer S., Aguilar G., Flores L., Bitran D., Duran R., Lopez O., Pacheco M. A., Reyes C., Uribe C and Mendoza M.J., 1999, The 15 June 1999 Tehuacan earthquake, Technical Report, CENAPRED (in Spanish).

Garcia D., Singh S. K, Herraiz M., Ordaz M. and Pacheco J. F., (2005, Inslab Earthquakes of Central Mexico: Peak Ground-Motion Parameters and Response Spectra, Bulletin of the Seismological Society of America, 95 (6): 2272-2282, DOI: https://doi.org/10.1785/0120050072.

Garcia D., Singh S. K, Herraiz M., Pacheco J. F. and Ordaz M., 2004, Inslab Earthquakes of Central Mexico: Q, Source Spectra and Stress Drop, Bulletin of the Seismological Society of America, 94 (3): 789-802, DOI :https://doi.org/10.1785/0120030125

Kitanidis P. K., 1986, Parameter uncertainty in estimation of spatial functions: Bayesian analysis, Water resources research 22(4), 499-507.

Melgar, D., X. Pérez-Campos, L. Ramirez-Guzman, Z. Spica, V. H. Espíndola, W. C. Hammond, and E. Cabral-Cano, 2018, Bend faulting at the edge of a flat slab: the 2017 Mw7. 1 Puebla-Morelos, Mexico earthquake, Geophys. Res. Lett. 46(6), 2633-2641. https://doi.org/10.1002/2017GL076895.

Secretaría de Cultura, 2018, Sismos y patrimonio cultural. Testimonios, enseñanza y desafíos 2017 y 2018, Dirección general de publicaciones de la Secretaría de Cultura.

Shapiro N.M, Singh S.K., Iglesias A., Cruz-Atienza V. and Pacheco J. F, 2000, Evidence of low Q below Popocatépetl Volcano, and its implication to seismic hazard in Mexico City, Geophysical Research Letters, 27(17), 2753-2756.

Singh S.K., Reinoso E., Arroyo D., Ordaz M., Cruz-Atienza V., Pérez-Campos X, Iglesias A. and Hjörleifsdóttir V., 2018, Deadly intraslab Mexico earthquake of 19 September 2017 (Mw7.1): ground motions and damage pattern in Mexico City, Seism. Res. Lett., doi: 10.1785/0220180159.

Singh S.K., Ordaz M., Pacheco J.F., Quaas R., Alcántara L, Alcocer S., Gutierrez C., Meli R., Ovando E., 1999, A preliminary report on the Tehuacán, Mexico earthquake of June 15, 1999 (Mw=7.0). Seism. Res. Lett. 70, 489-504.

MAY RAYLEIGH WAVES PROPAGATE WITH GROUP- AND PHASE-VELOCITIES OF OPPOSITE SIGN IN THE VALLEY OF MEXICO CITY?

Peter G. Malischewsky*[1] and Thomas Forbriger[2]

RESUMEN

Con base a la fórmula que determina la velocidad de grupo de las ondas sísmicas y utilizando resultados previamente publicados por los autores, se discute en forma teórica la ocurrencia de velocidades de grupo negativas de ondas de Rayleigh en modelos simplificados de la cuenca del Valle de México.

PALABRAS CLAVE: Ondas de Rayleigh, velocidades del grupo negativas, Valle de México

ABSTRACT

On the basis of the group-velocity formula the occurrence of negative group velocities of Rayleigh waves is theoretically discussed for simplified models of Mexico City's basin by using results of a preceding article of the authors.

KEY WORDS: Rayleigh waves, negative group velocities, Valley of Mexico City

INTRODUCTION

This short note is a complement of the article about unusual, equivocal Rayleigh dispersion curves by Malischewsky *et al.* (2017) in the Special Volume on the 30TH Anniversary of the 19 September 1985 Earthquake of *Geofísica Internacional*. It was not demonstrated, that the strange dispersion curves presented there lead to negative group velocities, but this is indeed the case as shown below. So this short comment in some way serves the popularization and understanding of negative group velocities, well-known in many fields of physics and techniques [see e. g. Nedopasov *et al.* (2017), Tamm *et al.*. (2017), Gérardin *et al.*. (2019)], in seismology as well [see Lysmer (1970), Forbriger (2017)] . Let us point out that in literature on normal mode theory solutions to the boundary value problem usually are discussed without an explicit source. The sign of propagation velocity then is not defined with respect to a source of wave energy. The

*Corresponding author
[1]Institute of Geosciences
Friedrich-Schiller University Jena
p.mali@uni-jena.de

[2]Karlsruhe Institute of Technology
76187 Karlsruhe, Germany

term "negative group velocity" thus actually means that "group velocity has the opposite sign of phase velocity" and is often coupled with the conception of "backward waves" in literature. It is not the intention of this short comment to shed light onto this connection. We only note, that with Shevchenko (2007) there are three definitions for forward and backward waves, where the classical one is that a wave is considered a forward (backward) wave if the directions of its phase and group velocities are the same (opposite).

GROUP VELOCITIES

The formula for the group velocity of waves [see e. g. Malischewsky (2018).] is

$$U(F) = \frac{C^2}{C - F \, dC/dF}$$

(1)

with dimensionless phase velocity C and dimensionless frequency F, which are defined depending on the model under consideration. Already Lamb (1904) has pointed out that it is possible for the group velocity to be of opposite sign with respect to phase velocity. He discusses the solution of the wave equation in the presence of a source of energy and points out that wave groups always propagate away from the source, while the complete wave train is actually a superposition of harmonic waves with negative phase velocity. Having a look on formula (1) U(F) and C are of opposite sign only for anomalous dispersion, i. e.

$$\frac{dC}{dF} > 0$$

(2)

with the additional condition

$$\frac{dC}{dF} > \frac{C}{F} \, ,$$

(3)

which is a differential inequality.

The dispersion curves in Fig. 1 of Malischewsky *et al.* (2017) concern the first higher Rayleigh mode in the simple LFB (Layer with Fixed Bottom) – model for the Poisson ratios $\nu = 0.37$ and 0.44, respectively. It can be demonstrated that both conditions (2) and (3) are fulfilled for specific frequency ranges, and the occurrence of negative group velocities is obvious. By using eq. (1) and numerical differentiation, the group velocity U is obtained and is presented together with the former phase velocity curves C in Fig. 1. The negative branches of group velocity occur in the frequency ranges

$F \in (0.53, 0.55)$ for $\nu = 0.37$ and
$F \in (0.64, 0.75)$ for $\nu = 0.44$.

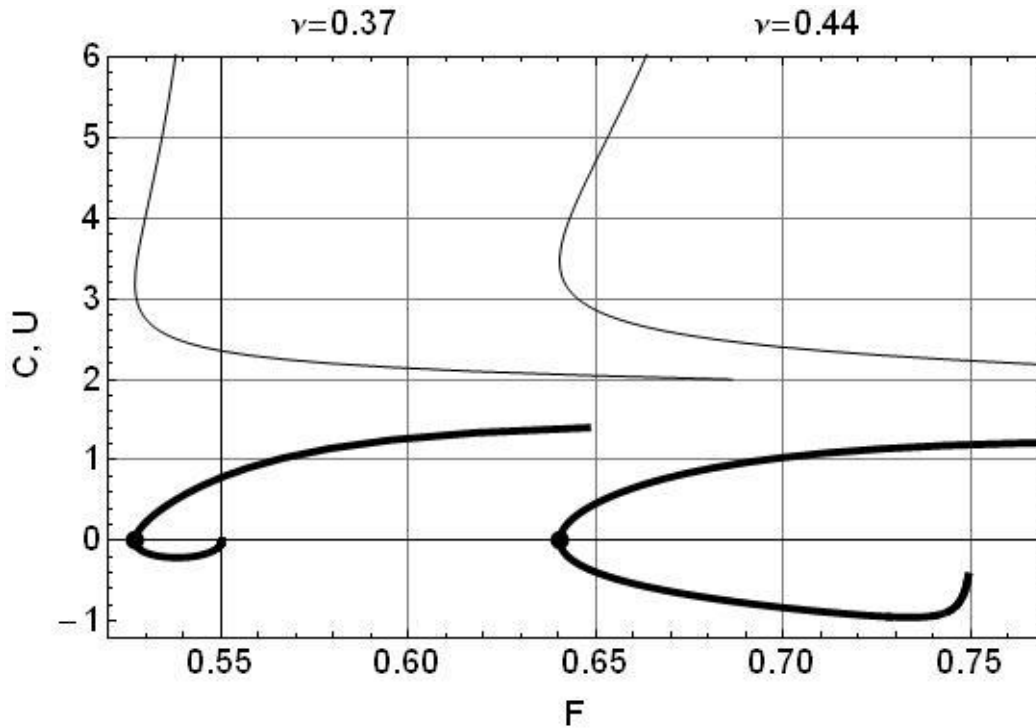These pictures are very similar to those ones obtained by Negishi (1987) in Lamb-wave context.

Figure 1. Phase (thin) and group (thick) velocity curves for Poisson ratios $v = 0.37$ and $v = 0.44$, respectively; the ZGV-points with lower frequencies are marked with black points

Obviously, a necessary precondition for negative group velocities is the existence of so-called ZGV – points (Zero Group Velocity points, see Fig. 1). The derivative dC/dF becomes infinite for the phase-velocity curve at these points. A marginal note: Condition (2) can be easily fulfilled for the fundamental Rayleigh mode of the LOH-model (Layer Over Halfspace) by using the results of Tuan et al. (2008) and specifying the parameters for which the dispersion curve starts with $dC/dF > 0$ for zero frequency. However, in absence of a ZGV-point, condition (3) is not fulfilled, and a negative group velocity does not occur.

Following Forbriger *et al.* (2020) these effects described here for the first higher mode occur for the fundamental mode in certain more complex models as well.

It is yet unclear, what the role of these special waves could be in the seismic regime of Mexico City's valley, but their pure possible existence is scientifically interesting enough to be mentioned and to position it into a larger context.

Let us come back to the title question by affirming it: If any facts are theoretically possible, the nature usually realizes them. Successful predictions is what we expect from a consistent theory. The most prominent example of recent years is the confirmation of the existence of gravitational waves after Einstein's prediction from 1916. For the phenomenon discussed here,

the seismological observation has not been made yet. However, on laboratory scale the phenomenon is confirmed by experiment [Wolf *et al.* (1988), Cès *et al.* (2011)].

ACKNOWLEDGEMENTS

REFERENCES

Cès, M., Clorennec, D. Royer, D. Prada, C., 2011, Thin layer thickness measurements by zero group velocity Lamb mode resonances, *Rev. Sci. Instrum.,* 82, 114902, doi: 10.1063/1.3660182.

Forbriger, T., 2017, Surface waves – benefits and pitfalls for seismic exploration (in German), In: DGG-Kolloquium. Neue Entwicklungen in der Angewandten Seismik. Ed.: Deutsche Geophysikalische Gesellschaft. Mitteilungen der Deutschen Geophysikalischen Gesellschaft, Sonderband I/2017, ISSN 0947-1944, 3-19. http://dx.doi.org/10.5445/IR/1000068706

Forbriger, T., Gao, L., Malischewsky, P., Ohrnberger, M., Pan, Y., 2020, A single Rayleigh mode may exist with multiple values of phase-velocity at one frequency, Geophys. J. Int., ggaa123. (doi: 10.1093/gji/ggaa123).

Gérardin, B., Laurent, J., Legrand, F., Prada, C., Aubry, A., 2019, Negative reflection of elastic guided waves in chaotic and random scattering media, *Scientific Reports*, 9, 1-8.

Lamb, H., 1904, On group-velocity, *Proc. London Math. Soc.*, s2-1.1, 473-479.

Lysmer, J., 1970, Lumped mass method for Rayleigh waves, *Bull. Seism. Soc. Am.*, 60, 89-104.

Malischewsky, P. G., Forbriger, T., Lomnitz, C., 2017, Unusual equivocal Rayleigh-dispersion curves for simple models taking into account the special propagation conditions in the valley of Mexico City (CDMX) – Preliminary results, *Geofísica Internacional*, 56, 7-12.

Malischewsky, P. G., 2018, Surface waves, In: Altenbach, H., Öchsner, A. (eds.) Encyclopedia of Continuum Mechanics. Springer, Berlin, Heidelberg, 1-9.

Nedopasov, I. A., Mozhaev, V. G., Kuznetsova, I. E., 2017, Unusual energy properties of leaky backward Lamb waves in a submerged plate, *Ultrasonics*, 77, 95-99.

Negishi, K., 1987, Existence of negative group velocities in Lamb waves*, Jpn. J. Appl. Phys.*, 26-1, 171-173.

Shevchenko, V. V., 2007, Forward and backward waves: three definitions and applicability, *Physics-Uspekhi*, 50, 287-292.

Tamm, K., Peets, T., Engelbrecht, J., Kartoffelev, D., 2017, Negative group velocity in solids*, Wave Motion*, 71, 127-138.

Tran Thanh Tuan, Malischewsky, P. G., Scherbaum, F., Ohrnberger, M., 2008, Dispersion of zero-frequency Rayleigh waves in an isotropic model 'Layer over half-space', *Geophys. J. Int.*, 175, 537-540.

Wolf, J., Ngoc, T. D. K., Kille, R., Mayer, W. G., 1988, Investigation of Lamb waves having a negative group velocity. *J. Acoust. Soc. Am.*, 83, 122-126.

_____Original paper

Geophysics for geothermal exploration. Directional-derivatives-based computational filters applied to geomagnetic data at lake Cuitzeo, Mexico

Alberto Mazzoldi[1,2*], Victor Hugo Garduño-Monroy[1†], Joaquín José Gómez Cortes[1] and Jorge Alejandro Guevara Alday[1]

Resumen

Para el desarrollo de un campo geotérmico, el conocimiento de la distribución de fracturas, la hidrología y la evolución tectónica del sitio a través de la caracterización estructural del sistema natural es un requisito previo a la perforación de pozos exploratorios. Fallas y fracturas representan vías preferenciales por el flujo de fluidos en el subsuelo y pueden ser detectadas mediante investigaciones geológicas en la superficie y geofísicas en el subsuelo. Una anomalía magnética positiva y de forma sub-circular en planta se encuentra en el medio del lago Cuitzeo, México. A través de un levantamiento geomagnético dentro y alrededor del área que comprende la anomalía tratamos caracterizar el reservorio geotérmico que, al sur del lago, está notificado por manifestaciones hidrotermales. Utilizando filtros computacionales basados sobre el uso de operaciones con las derivadas de valores de campo a los datos magnéticos grabados, hemos puesto en luz algunas de las estructuras que influencian la circulación de los fluidos en el sistema geotermal. Nuestra atención se focalizó sobre fallas ~N-S and E-W, pertenecientes respectivamente a la tectónica Básin & Range (B&R) y a la del Cinturón Volcánico Mexicano (CVM). Según nuestra interpretación, la interacción de dos o mas estructuras de diferentes orígenes (B&R y CVM), además del entorno geodinámico específico (subducción de zona de fracturas), facilitó el surgimiento de cuerpos magmáticos básicos del profundo que, bloqueados por la capa argilosa de sedimentación lacustre del Cuitzeo, dieron lugar, enfriándose lentamente, al sistema geotermal y contribuyeron a la formación de la anomalía magnética.

Palabras clave: CVM; Cuitzeo; Sistema geotermal; Geofísica; Gradientes direccionales; Campo Volcánico Michoacán-Guanajuato.

Abstract

For the development of a geothermal field, the understanding of fracture distribution, hydrology and tectonic evolution of the site through structural characterization of the natural system is a prerequisite to the drilling of exploratory wells. In order to image the underground shape of

*Corresponding author
albertomazzoldi@yahoo.com

[1]Instituto de Investigaciones en Ciencias de la Tierra
Ciudad Universitaria, CP 58060
Morelia, Mich., Mexico

[2] EDRA
Via di Fioranello 31, 00134
Roma, Italy

approximately planar, relatively permeable, geologic features (fractured rock-volumes around fault planes) and to detect hot rock volumes, geologic and geophysical surveying is carried out. A strong positive magnetic anomaly, nearly circular in 2D, characterizes the middle of Cuitzéo lake, Michoacán, Mexico, apparently not related with a volcanic structure on the surface. It may instead be associated to the geothermal system in the area which yields at present hot springs at the southern shore of the lake, at boiling temperatures. In this study, we conducted a ground magnetic survey within and around Lake Cuitzeo with the aim of characterizing this anomaly, following one-kilometer-spaced survey-lines and covering an area of approximately 100 km$_2$. To enhance interpretability, we applied computational filters based on directional derivatives (vertical and horizontal) to our reduced-to-pole magnetic-field raw data – illuminating underground faults and other permeable pathways for fluids and delineating contacts between differently magnetized rocks, through maxima and minima on maps. While most filters used were able to define the basic configuration of the system, we found that computational filters working with ratios of derivatives (vertical and horizontal) were able to better account for the depth of a magnetic source. Also, faults were more clearly imaged on maps. We could mainly highlight ~E-W and ~N-S striking fault-systems, respectively belonging to the ~N-S Trans-Mexican Volcanic Belt extensional tectonics and to the ~E-W Basin & Range, both with lateral movements and still active today. We interpret the magnetic source as a magma body (related to the volcanism of Michoacán-Guanajuato Volcanic Field) that remained trapped during its ascent under Cuitzeo lacustrine sedimentation, during the last 500 ka, forming the once stronger geothermal system.

INTRODUCTION

Geothermal energy exploits the Earth's natural heat for power generation. It is a low-carbon, base-load alternative energy that, despite its low cost relative to other energy sources, is not yet widely used (Goldstein *et al.*, 2011): financial risk associated with locating and developing the resource – which means understanding the underground shape of permeable features such as faults, for their exploitation – have represented so far, together with environmental impacts, main barriers (Subir and Morrow, 2011; IFC, 2013). Geophysical techniques are often useful for discovering unknown subsurface conditions and can be utilized as preliminary screening before performing direct investigations. Non-invasive potential methods – such as gravity and magnetics – are often appropriate for locating structures (e.g. Glen *et al.*, 2008) and in the general characterization of an underground (geothermal) system, aiming to its exploitation (Pipan *et al.*, 2010; Kipsang, 2015). During the last five decades, a variety of methods based on the use of vertical and horizontal gradients of potential-field anomalies have been developed and implemented for the determination of geologic boundaries, such as contacts and faults – hence also valuable for the exploration of geothermal resources (Nabighian, 1972, 1974; Keating and Pilkington, 1990; Ferreira *et al.*, 2013).

In the trans-tensional sector of the Great Basin, Basin and Range (B&R), western USA, the importance of characterizing known geothermal resources is heightened by the fact that most of the still-undiscovered geothermal systems (~75%) may show no surface hydrothermal springs,

thus defined as blind or hidden (Coolbaugh *et al.*, 2006; Faulds and Hinz, 2015). Faulds *et al.* (2010; 2012) categorized almost 250 geothermal fields in the Great Basin and found that the most favorable tectonic setting for the existence of a system is associated with the presence of a (major) normal fault: geothermal fluids flowing preferentially at fault tips and in fault interaction zones. These zones are characterized by a high density of fractures and dynamically-maintained permeability (Curewitz and Karson, 1997; Rowland and Sibson, 2004; Cashman *et al.*, 2012).

Through the study of aerial data collected along the Surprise Valley, CA (North-West Basin & Range), Glen *et al.* (2013) identified an intra-basin magnetic high, running a significant length of the valley, which they interpreted as a buried, faulted mafic dyke. All the geothermal manifestations in the valley seem to be related to this body as they lie where the high is cut by perpendicular faults (Glen *et al.*, 2013).

In this paper we examine an area within the central Trans-Mexican Volcanic Belt (TMVB, Figure 1), in the northeastern part of the Michoacán-Guanajuato Volcanic Field, a sector interested by, approximately, N-S, E-W, NW-SE and NE-SW structures, repeatedly involved in the formation of small, monogenetic and larger, polygenetic volcanoes (Hasenaka and Carmichael, 1985; Suter *et al.*, 1999; Cebriá *et al.*, 2010). We use magnetic data recorded through detailed surface surveying for characterizing a localized positive magnetic anomaly corresponding to a stretch of the central Cuitzeo Lake (Michoacán, Mexico). Southernly, on the lake shore, hydrothermal manifestations reveal the presence of a geothermal system of medium enthalpy at depth (Arredondo-Fragoso, 1983; Campos-Enríquez *et al.*, 1988).

In the following, we first give a broad review of the regional geology, describing the different tectonics interesting the area. We then apply filters based on combinations of directional derivatives to magnetic data surveyed in the study area, for structural interpretation and with the aim of identifying the heat source and the local structures that allow the rise of the geothermal fluid. We eventually try to give a volcanological explanation for the presence of such heat source at depth.

GEOLOGIC SETTING

The study area is located within the central segment of the TMVB, between 99° and 102° W longitude, Figures 1 and 2. Regionally, the area is interested by the northward extension of the arc, carried by ~E-W striking normal faults with a minor but consistent left-lateral slip component (Suter *et al.*, 1995a; Ego and Ansan, 2002; Garduño-Monroy *et al.*, 2009). From Oligocene times, this territory has been affected by two main trends of subduction-arc related volcanism and the related sin- and post-volcanic extensions, nearly perpendicular to each other. These are the NNW–trending Sierra Madre Occidental volcanic province and the roughly East-West–trending Trans-Mexican Volcanic Belt (TMVB). The two volcanic belts overlap between the Pacific coast and the longitude of Mexico City (Figure 1a) and have at least two characteristic features in common: the broad orientation of the arc and the dominant composition of the rocks (Ferrari *et al.*, 1999).

1 Sierra Madre Occidental volcanic and Basin and Range extensional provinces

The Sierra Madre Occidental (SMO) of western Mexico is a huge Silicic plateau which runs a NNW-trending direction for over 2000 km, from south of the TMVB to the MX/USA boarder (Ferrari *et al.*, 1999; Ferrari *et al.*, 2000). It is the result of Cretaceous-Cenozoic magmatic and tectonic episodes related to the subduction of the Farallon plate beneath the North American Plate (NAP). The rapid increase of the subduction angle during the removal of the plate generated a flux of uprising hotter astenospheric magma, underplating the NAP and intruding within the lower crust (Ferrari *et al.*, 2002), allowing for the extrusion of >300,000 km3 of silicic material (Huppert and Sparks, 1988; Ferrari *et al.*, 2007), apparently erupted from fissure vents corresponding to Basin & Range faults traces (Henry and Aranda-Gomez, 1992; Aguirre-Díaz and Labarthe-Hernández, 2003).

The extensional phases that followed the main volcanic peaks and aged about 30, 23, 10 and 5 Ma (Ferrari *et al.*, 1999) have been sufficiently intense (up to 100%) in the northern part of the SMO (northern Mexico, Figure 1a) to exhume part of the Proterozoic crystalline basement (Dickinson and Lawton, 2001; Ferrari *et al.*, 2007), whereas in the reminder of the arc, and particularly within the southern B&R province, extension has not exceeded 20% (Henry and Aranda-Gomez, 1992; Aranda-Gomez and McDowell, 1998), achieving in the Mesa central, north of TMVB (Fig. 1a), a maximum of about 8% (Nieto-Samaniego *et al.*, 1999).

While an ignimbrite from the upper part of a 300 m thick rhyolitic succession 15 km south of the city of Morelia has been dated by K-Ar at 21±1 Ma (Pasquaré *et al.*, 1991), B&R faults allowing for the extrusion of SMO lavas and aged between 38 and 25 Ma are widespread south of the TMVB (Alba-Aldarve *et al.*, 1996; Morán-Zenteno *et al.*, 1999). Garduño-Monroy and Gutiérrez-Negrín (1992) noted how the regional NNW-SSE B&R Taxco-Queretaro fault, passing some tens of kilometers east of Morelia, represents the eastern limit of SMO volcanism and of the Guerrero Terrain (Campa-Uranga and Coney, 1983).

Seismicity, high heat flow and recent volcanism indicate that the Basin and Range province is actively extending, within its northern and southern parts (Parson, 1995).

2 Trans-Mexican Volcanic Belt and subduction of Fracture Zones

The TMVB is an east-west, Late-Miocene to Quaternary mostly calc-alkaline continental volcanic arc of more than 1000 km longitudinal length and up to 150 km N-S width, originated by the subduction of the Rivera and Cocos plates under the North American plate (Nixon, 1982; Garduño-Monroy *et al.*, 1993; Ferrari *et al.*, 2012), Figure 1b. The mean elevation of the arc is >1500 m with respect to the southern forearc region; summit elevations are between 3000 and 5700 m (Suter, 1991). TMVB presents high mean heat flow (>80 Wm$_{-2}$; Prol, 1991) and the combination of this with features such as a negative regional Bouguer anomaly (Urrutia-Fucugauchi and Flores-Ruiz, 1996), volcanic activity, sin- and post-volcanic shallow extensional faulting and seismicity, suggests that its central E-W Chapala-Tula fault system may correspond to a young active continental rift (Luhr *et al.*, 1985; Marquez *et al.*, 1999). To the point that Verma *et al.* (2009) coined the terminology 'Mexican Volcanic Rift'.

Along the arc, volcanoes are distributed with a ~15o oblique trend relative to the Middle American Trench (MAT, Figure 1): this suggests that their location is controlled by the slab

geometry (Pardo and Suarez, 1995; Ego and Ansan, 2002; Ferrari *et al.*, 2012). Particularly, the area of Mexico inland of the MAT can be split into several sections with different subduction angles (from W: Jalisco block, JB, 50₀; Michoacán block, MB, 30₀; Guerrero block, GB, 0₀ until the latitude of Mexico City and Oaxaca block, 30₀. Pardo and Suarez, 1995; Stubailo *et al.*, 2012. Fig. 1b).
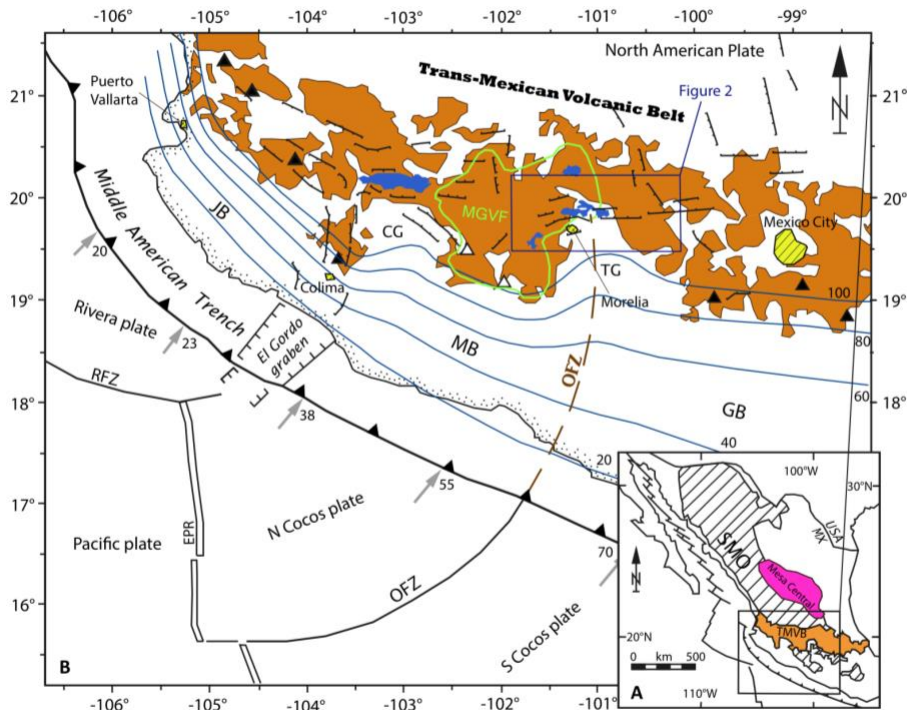

Figure 1 A) The two main volcanic provinces interesting Mexico, Sierra Madre Occidental (SMO) and Trans-Mexican Volcanic Belt (TMVB). For reference, also pictured is the Mesa Central area and the Mexico/USA border. B) TMVB volcanism (brown). With black triangles are located active volcanoes – white triangles represent Paricutin and Jorullo cinder cones at the southern extension of the Michoacán-Guanajuato Volcanic Field (MGVF, green line). Isobaths of the Cocos and Rivera plates (blue lines) follow the subduction of Rivera and Orozco Fracture Zones (RFZ and OFZ). JB=Jalisco Block; MB=Michoacán Block; GB=Guerrero Block; CG=Colima Gap; TG=Tzitzio Gap. Gap. Numbers near arrows along the Middle American Trench indicate subduction speed, in mm/yr.

The Rivera Fracture Zone (RFZ) is generally recognized as the Rivera-Cocos Plates Boundary (RCPB, DeMets *et al.*, 1990; Bandy *et al.*, 1995), it can be dated at 10 Ma as the Rivera plate (Bandy, 1992; Stubailo *et al.*, 2012) and is interested by higher heat fluxes than the surrounding oceanic crust. Gravity, heat-flow and sea-morphology analyses suggest that the subducted part of the RCPB lies directly beneath and is oriented parallel to the Southern Colima graben (Bandy, 1992). Bandy *et al.* (1995) showed that the RCPB lies east of the Central and Northern Colima graben and is related to the Colima Gap (CG, Figure 1b), coinciding in plan with the area where the Wadati-Benioff zone undergoes a sharp decrease in dip, eastward. These authors suggested the presence of a NE-SW oriented tear-fault between the subducting plates, explaining the low density zone beneath the granitic highlands (CG) by thermal convective movements in the upper mantle, providing a conceptual model consistent with roughly E-W extension within the subducting lithosphere (Nixon, 1982; Bandy, 1992; Ferrari *et al.*, 1994).

Easterly of the RFZ, Stubailo *et al.* (2012) confirmed previous results (e.g., Pardo and Suarez, 1995; Blatter *et al.*, 2007) that the angle of subduction varies substantially at the longitude of the Tzitzio Gap (TG, figure 1b), consistent with the location of the Orozco Fracture Zone (OFZ, Fig. 1), which separates older (17.6 Ma), cooler and denser oceanic crust at the NW side from younger crust (12.3 Ma) at the SE (Manea *et al.*, 2005). Slab rollback (retreat) below the MB occurs at about 5 cm yr$_{-1}$ (Singh and Pardo, 1993; Bandy *et al.*, 2000; Suter *et al.*, 2001): this process should displace mantle asthenosphere, and, in the presence of a slab tear, the mantle material would flow through it. Tear faults occur where the plate is weakened by the presence of the fracture zone.

During subduction, fracture zones are buoyant enough to usually lower the angle of descent of the subducting plate: the arc volcanism is consequently displaced landward, creating indentations in the front of the volcanic arc (McCann and Habermann, 1989). Through vulcanological studies, Blatter and Hammersley (2010) concluded that the OFZ is being subducted under the TG and that the buoyancy of the fracture zone would cause this section of the Cocos slab to subduct at a lower angle than the Cocos slab on either side of the OFZ. This causes the subducting material to reach the melting depth of about 100 km at higher distance from the trench, in correspondence with the OFZ (and TG), spatially 'delaying' volcanism at the surface towards the north. Dougherty *et al.* (2012) proposed that the Cocos slab is currently fragmenting into a N Cocos and a S Cocos plates along the projection of the OFZ, in agreement with other authors (Bandy, 1992; Bandy *et al.*, 2000). They identified this tearing event as a younger (~0.9 Ma) analogy of the 10 Ma old Rivera-Cocos plate boundary.

3 STRUCTURAL GEOLOGY, REGIONAL SEISMICITY AND STATE OF STRESS OF CENTRAL TMVB

The central part of the TMVB (99$_\circ$-102$_\circ$W) is characterized by major E-W intra-arc basins: from W to E, the Chapala, Cuitzeo, Acambay and Mezquital grabens, 8-10 Ma old (Garduño-Monroy *et al.*, 1993; Rosas-Elguera *et al.*, 1997), whose E-W to ENE-WSW bordering normal faults have mean Quaternary slip rate of <0.1 mm yr$_{-1}$, characterizing the area with a ~N-S oriented extension of <5% (Suter *et al.*, 1995a; Ferrari and Rosas-Elguera, 2000). Recent studies have proposed, for some of these structures, an age of 18 Ma (Mendoza-Ponce *et al.*, 2018). Figure 2 shows the Acambay and Cuitzeo extensional areas. The Acambay graben is a ~30 km long E-W structure with delimiting faults dipping 50$_\circ$-70$_\circ$, with a mean slip rate of 0.17 mm yr$_{-1}$ during Holocene times (Langridge *et al.*, 2000). Cuitzeo graben (and half-graben) can be traced for over 45 km and its master faults dip between 45$_\circ$ and 75$_\circ$ (Ferrari *et al.*, 1991; Garduño-Monroy *et al.*, 2009. See Figure 3), having slip rates between 0.09 and 0.18 mm yr$_{-1}$, which is approximately three times higher than in the Morelia area, 20 km south (Suter *et al.*, 2001). E-W fault planes' striations indicate an extensional (N-S) dip-slip with a left-lateral strike-slip component (Pasquaré *et al.*, 1988; Garcia-Palomo *et al.*, 2000), which was explained by Ego and Ansen (2002) with slip-partitioning at the trench.
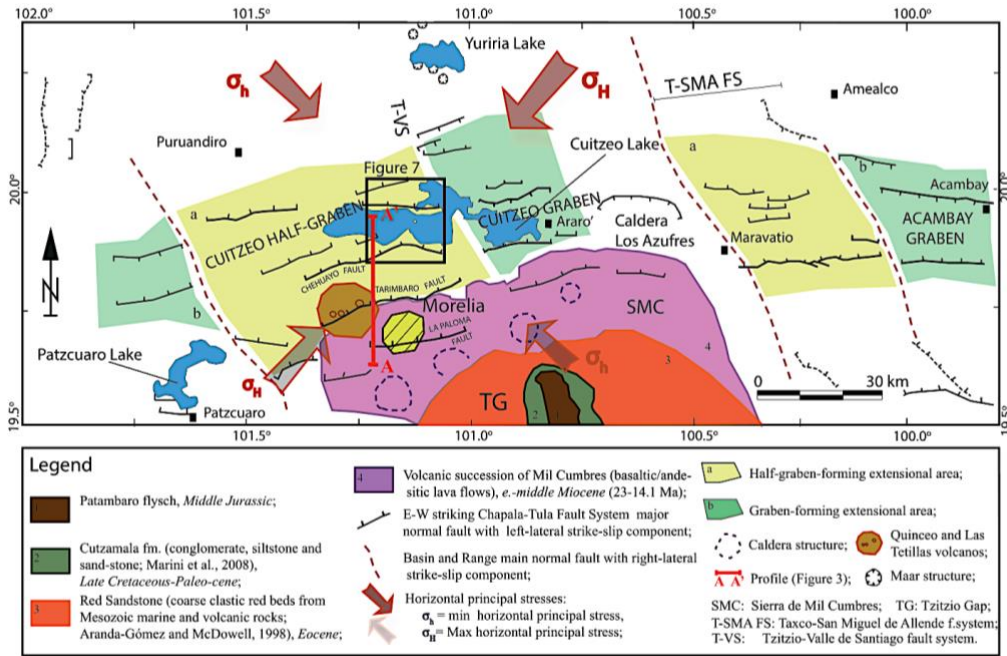
Figure 2. Cuitzeo graben and half-graben, representing the proto-continental rift structure of the Chapa-Tula fault system, cut by regional NNW-SSE normal structures with right lateral sense of shear, belonging to the southern Basin & Range tectonics. Also represented are the Tzitzio Gap (TG) and Sierra de Mil Cumbres (SMC) in the south and some Maars structures in the north, around Yuriria lake. Centrally, the Cuitzeo basin and the area of study (black box). Image modified after Garduño-Monroy *et al.*, 2009.
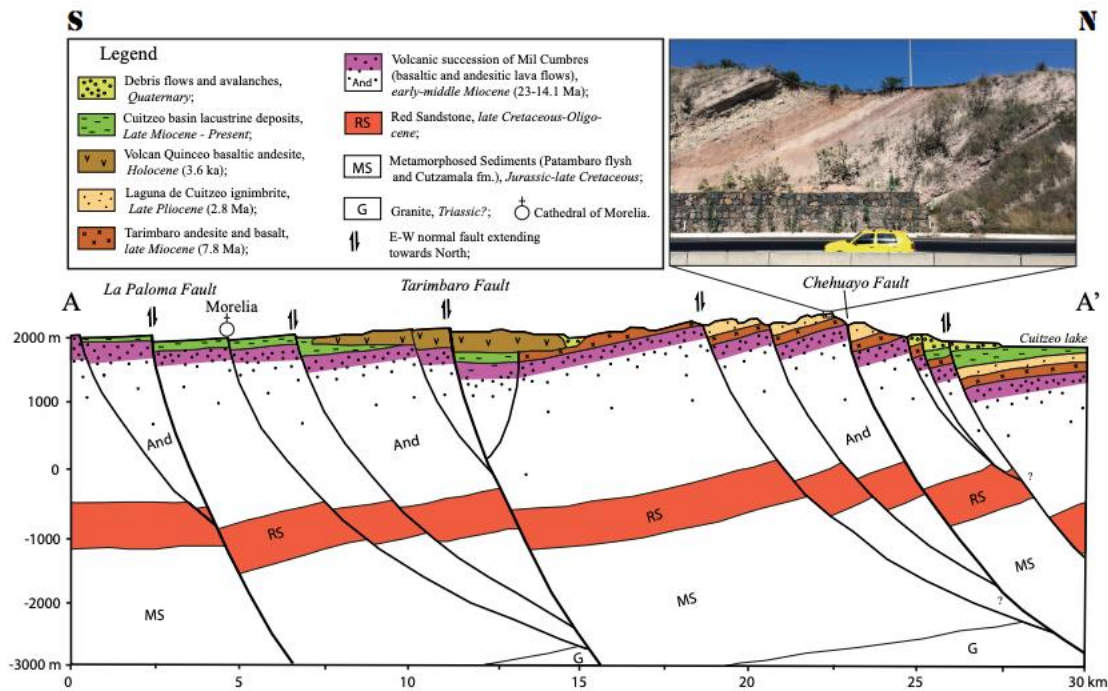

Figure 3. Geologic profile AA' from Figure 2. Evident are the E-W listric normal faults causing minor extension (<5%, see text). The stratigraphy under Cuitzeo lake sedimentation is mainly composed of TMVB-basamental andesite of basic and intermediate nature.

111

Central TMVB is seismically active (Suter *et al.*, 1996; Garduño-Monroy *et al.*, 2009) and during the last century, eight shallow events with magnitude 4.1<M<6.9 occurred along E-W faults; among these, the Acambay, 1912 (M=6.7) and the Maravatio, 1979 (M=5.3) earthquakes (Suter *et al.*, 2001).

Southern B&R NNW-SSE structures present a normal-right-lateral sense of motion (Garduño-Monroy and Gutierrez-Negrin, 1992; Garcia-Palomo *et al.*, 2000). Historical seismic events of Mw>3 comprehend the Pinal de Amoles (1887) and the Sanfandila (1998) events (Suter *et al.*, 1996; Zuñiga *et al.*, 2003) and Peñamiller sequence (2010-2011; Clemente-Chavez *et al.*, 2013). Although we do not have data on mean slip rates, Alaniz-Alvarez *et al.* (1998) determined how, on average, north-south B&R faults only have about one-third of the horizontal displacement rate of the east-west TMVB faults. The contemporaneous activity of TMVB and B&R faults in the area was explained with a recurrent permutation of $\sigma 1$ and $\sigma 2$ (see figure 2, where $\sigma 1 = \sigma V$) which would allow for the activation of NNW-striking B&R structure as right-lateral during the deposition of the Cuitzeo (and Acambay) basin sedimentation (Suter *et al.*, 1995b; Ego and Ansan, 2002).

3.1 The Michoacán-Guanajuato Volcanic Field

A monogenetic volcanic field, covering an area of some 40,000 km_2 is located at the west-central sector of TMVB, extending over northern Michoacán and southern Guanajuato and interesting the study area (Figures 1 and 4). A unique part of TMVB for its lack of young large composite volcanoes, dominant in the rest of the arc, the Michoacán-Guanajuato Volcanic Field (MGVF) has been active from Pliocene to present (Hasenaka and Carmichael, 1985; Ferrari *et al.*, 2007). It contains more than 1000 small volcanic centers, as shown in Figure 4, and its main eruptive products are calc-alkaline olivine basalt and basaltic andesites (Hasenaka and Carmichael, 1987): rocks crystallized from these magmas can hold relatively high abundances of ferromagnetic minerals. The majority of the small-sized volcanoes are cinder cones (~900) but the field also comprehends lava domes, maars, tuff rings and thick lava flows not associated with cones (Williams, 1950; Hasenaka, 1994), coexisting in time and space with over 300 medium-sized shield volcanoes distributed throughout the volcanic field and whose origin may not be univocal (monogenetic or polygenetic. Hasenaka *et al.*, 1994; Verma and Hasenaka, 2004). While small volcanic centres in MGVF are spread all over the extension of the field, authors have identified alignments of cones following geological structures (Cebriá *et al.*, 2010; Gomez-Vasconcelos *et al.*, 2015), implying that, although volcanism may be a consequence of contemporaneous extensional regimes, the distribution of monogenetic vents is actually controlled by reactivation of older fractures, producing space for magma ascent at near surface levels (Hasenaka and Carmichael, 1985).
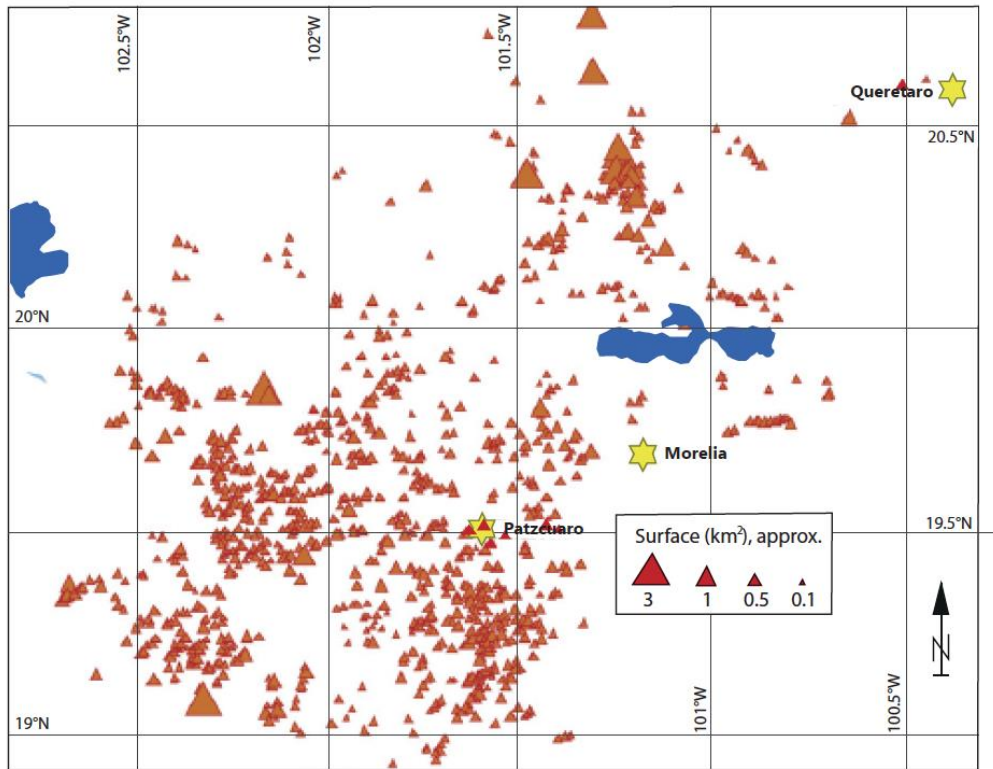
Figure 4. Extension of the Michoacán-Guanajuato Volcanic Field, with an approximate description of cone dimensions (data from Pérez-Lòpez *et al.*, 2011).

Through geochemical and isotopic studies of rock samples from the whole extension of the MGVF, Verma and Hasenaka (2004) concluded that no slab input is present in the basic magmas of the field and that different degree of partial melting of a heterogeneous mantle source could explain the origin of most magmas in the field, allowing for some crustal assimilation for the most evolved – supported by the presence of frequent granitic xenoliths (Verma and Hosenaka, 2004, and references therein).

4 REGIONAL GEOPHYSICS AND THE STUDY AREA

Figure 5 presents the relative Bouguer anomaly with respect to the WGS84 across the area within and around the Cuitzeo Basin. This map is based on data of Petroleum of Mexico (Pemex) from 1980 (Arredondo-Fragoso, 1983). The lowest values of the gravity field within the lake are linked with relatively light lacustrine sediments (density, $\varrho \cong 1.7$ Kg m$_{-3}$) and may then correspond in plan to the depocenter of the lake (where sedimentation has been highest during the past 8-10 Ma), with an estimated thickness of about 1.5 km. Positive anomalies, S and NE of the lake, are respectively linked with the Sierra de Mil Cumbres (SMC) and the Sierra the San Andres (SSA) ranges, built through eruptions of andesitic material ($\varrho \cong 2.7$ kg m$_{-3}$).
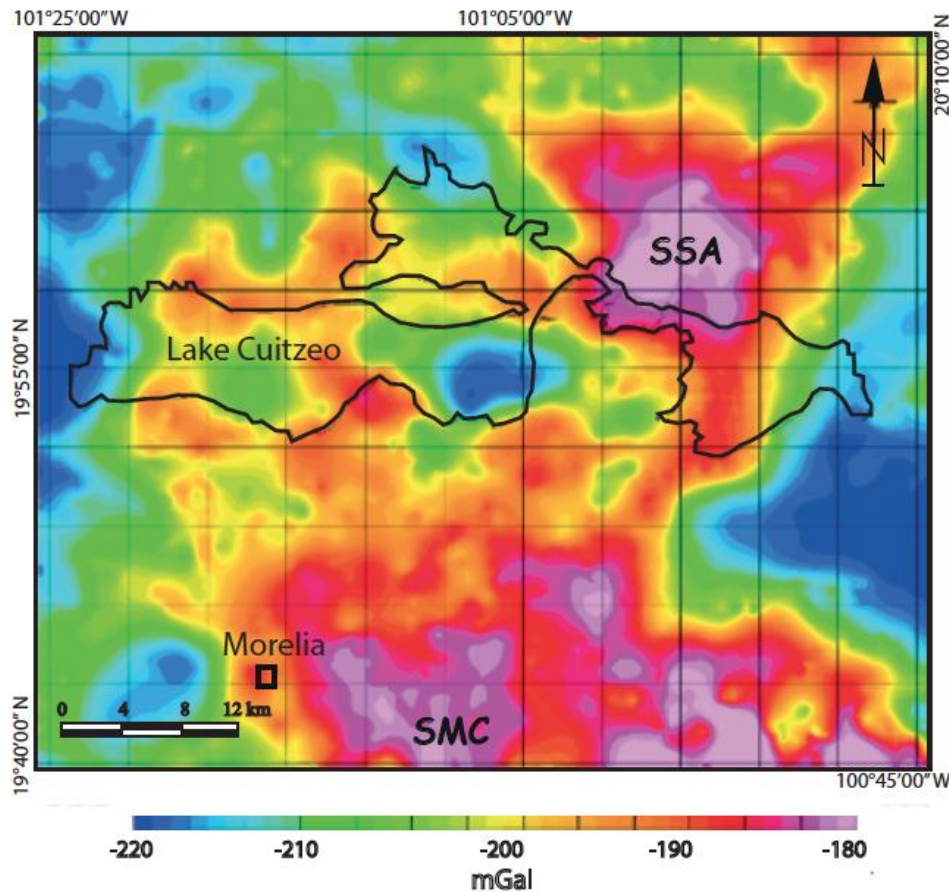
113

Figure 5. Map of anomalous values of gravitational acceleration in the area of the Cuitzeo lake. Peaks are related with the Sierra de San Andrés (SSA), northeast of the lake, and Sierra de Mil Cumbres (SMC), south. Regional lows border the area longitudinally while, in the middle of the lake, low values are located above the depocentre of the basin.

Figure 6 shows the reduction to the pole of the regional magnetic field around the study area, from aeromagnetic data of the Mexican Geological Survey (Servicio Geológico Mexicano, 1988). The magnitude of an anomaly in the magnetic field recorded at the surface, with respect to the International Geomagnetic Reference Field (IGRF; Thebault *et al.*, 2015) mean value, is dependent on the concentration of ferromagnetic minerals in the rocks of the upper crust at the site (Jackson and Bowies, 2014). Strong positive anomalies may then be related with large volumes of rock of basic composition (andesitic/basaltic solidified magmatic bodies), below Curie temperature for magnetite (around 575oC) and crystallized after the Matuyama-Brunhes reversal, about 780 ka (or during any other period of normal polarity), outcropping at the surface or trapped within the shallow crust. Cuitzeo basin is bordered by different magnetic highs linked with volcanic edifices at the surface (Figure 6), particularly the SSA, NE of the lake.

A relatively strong positive magnetic anomaly lies in the middle of the actual lake, some hundreds of meters NW of the gravity low, in plan. The origin of this anomaly may be found in a volcanic structure older than the lake and consequently covered by the lake sediments, or it may be correlated to an ascending magma body, blocked by the plastic lacustrine sediments.
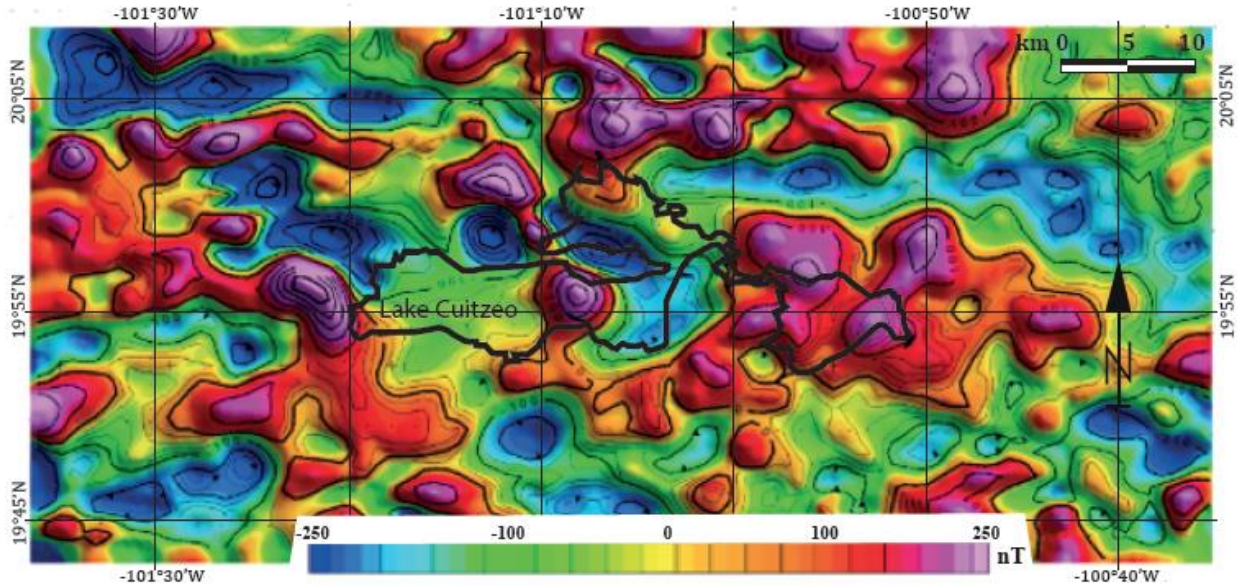
Figure 6. Regional magnetic anomaly (vs IGRF values) map. Positive anomalies around the lake are related with volcanic edifices built with basic and ultrabasic magmas. In the middle of the lake, slightly NW with respect to the gravimetric low, a positive anomaly is studied in this work.

In Figure 7a principal lithologies and main structures are presented: massive andesitic and ignimbritic highly fractured banks outcrops in the area (Fig. 7b and c). Our structural survey showed a statistical prevalence of ~E-W fault planes on outcrop, with dips <75$_\circ$. Nearly vertical ~N-S striking fault planes (showing horizontal striae and with fractures completely sealed by hydrothermal calcite) outcrop in an area south of San Juan Tararameo (SJT, Figure 7d), denoting the existence of a paleo-geothermal system. In the image, inferred continuations of some of these structures below the lake are shown with dotted lines and an andesitic island can be seen in the center of the image. Shown are also the areas interested by geothermal manifestations, with more than 100 springs between San Agustin del Mais (SAM) and SJT, laying near faults intersection (Sibson, 1981; Rawland and Sibson, 2004) and marking the areas with long-lived siliceous sinter terraced-deposits, associated with high temperature hydrothermal reservoirs (Fournier and Rowe, 1966).

Water temperatures of the springs reach 93$_\circ$C (our work), water-boiling T at the location (1820 m a.s.l.). A geochemical study of different geothermal springs around lake Cuitzeo (Segovia *et al.*, 2005) found at SAM and SJT steam heated waters in partial equilibrium, observing a mixing trend among the samples – indicating reservoir temperatures between 150 and 220$_\circ$C. Their Radon analysis results indicated a highly efficient fluid flow transport in the zones where higher temperatures were estimated. Lastly, the 8 NE-SW traces over which magnetic measurements were taken, as described in the following, are also depicted in Figure 7.
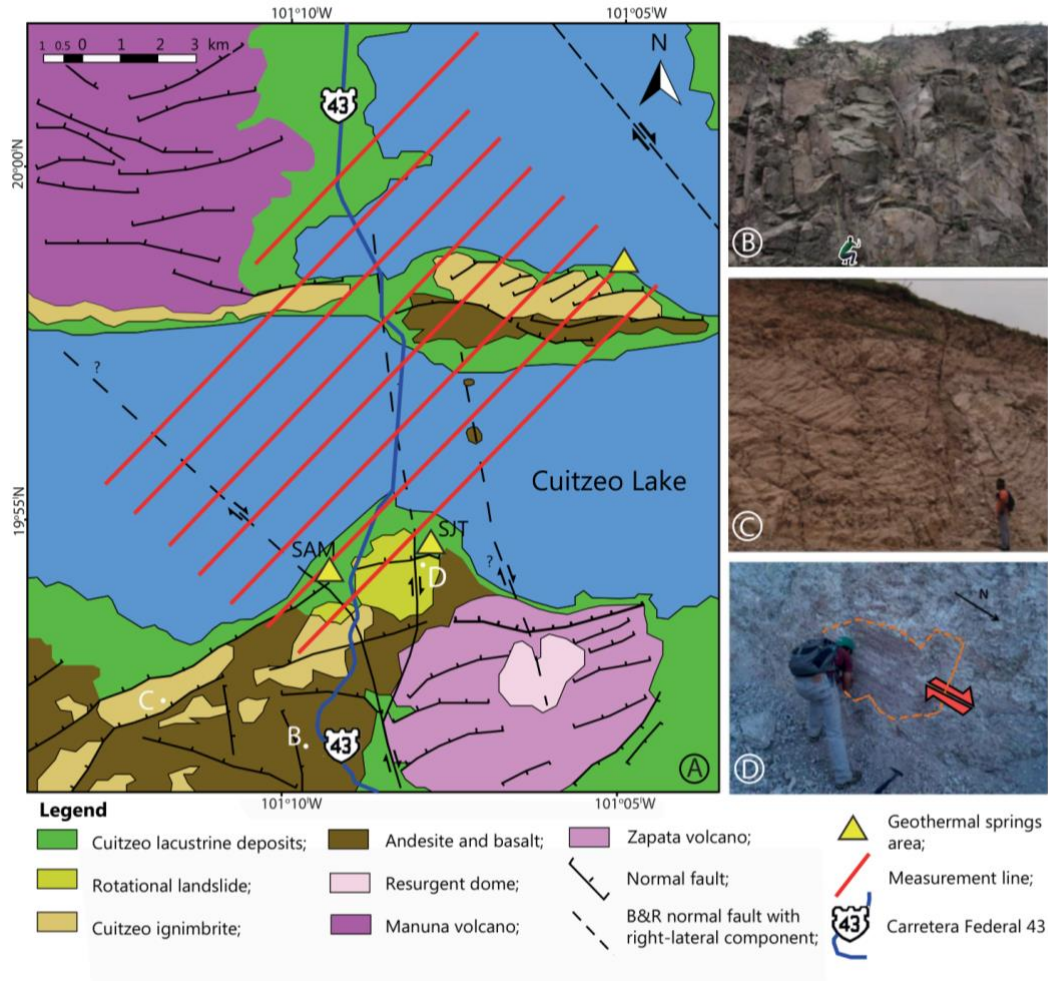
Figure 7 a) The area of study. Represented in the picture is the geological map of this territory with traces of known and supposed fault lines. Also located are the neighborhoods endowed with geothermal springs and the eight lines followed by our magnetic survey. b) Andesite block outcropping. c) Ignimbritic blocks. d) Right-lateral strike-slip fault plane within the andesitic basement, filled with deposition of geothermal calcite.

MAGNETIC SURVEY: DATA ACQUISITION, PROCESSING AND INTERPRETATION

Survey lines, spaced 1 km, were 15 km long but the northern one (reduced to 8 km, Fig. 7a) and were covered on foot and by rowboat (made of plastic and wood for not affecting measurements), from May 2015 to July 2016. Measurements of magnetic field where taken at stations spaced 100 m on each line, using a Geometrix G-857 proton-precision magnetometer, connected with a Garmin Oregon 450 GPS that guaranteed each measure to be taken within 2 meters from the station location, on each line. Different stations could not be covered due to the presence of anthropic barriers, corrupting measures in their proximities (e.g., buildings and other constructions, power lines), leaving a total of 975 point-values for analysis, over an area of some 110 km2. Instrumentation also comprehended an independent base-station for calculating daily variations of the magnetic field due to solar wind interferences during working hours, recording values at a fixed point. Due to theft of the base-station, we used the values of the

Magnetic Observatory of Teoloyúcan to make diurnal corrections to our data, during the last part of the survey.
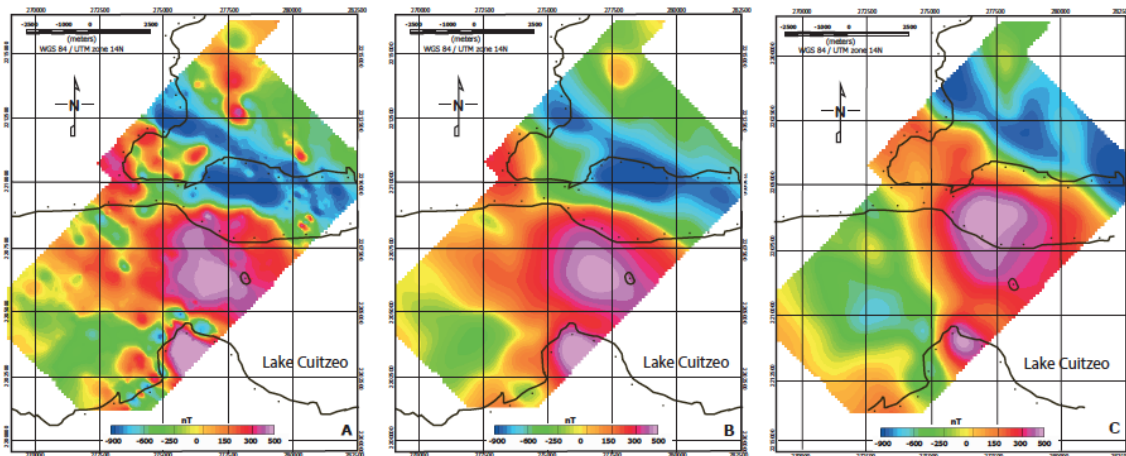

Figure 8 a) Map displaying raw values of the magnetic anomaly (relative to the IGRF) recorded along the measurement lines. Superimposed is Cuitzeo lake-shore contour. b) Upward Continuation at 500 m depth (see text for explanation). c) Reduced-to-Pole values after Upward Continuation; derivative-based computational filters have been applied on this value-grid.

We worked on the magnetic raw database (after correcting for daily variations) using the software Encom Discover PA 2010 (®RockWare). We applied to the mapped dataset computational filters based on operations with directional derivatives of the data, as described in the following. Figure 8a maps the anomaly values of the Total Magnetic Field, relative to the IGRF, displaying a positive anomaly in the middle of the surveyed area.

Surface data suffer from high-frequency noise due to shallow sources and probably also due to higher-than-optimum stations separation, for some stations. One of the tasks of data processing is to simplify the complex information provided in the original data: we have applied to our data an Upward Continuation (UC) filter, a low(wave-frequency)-pass filter which allows to avoid considering the contribution to the total magnetic field recorded at the surface given by rock layers above a certain depth (e.g. Gianiyu *et al.*, 2013, Ferreira *et al.*, 2013). Specifically, the filter was applied to the data-grid for the depth of 500 m in order to discard the contribution of high-frequency shallower potential sources to the recorded magnetic field values, as shown in Figure 8b. The filter Reduction-to-Pole (RP) is utilized to image measured values as if the measurements were taken at the magnetic pole: it reduces bipolar anomalies to monopolar ones, considering magnetic Inclination and Declination at the site (respectively 47° and 7° for the study area), basically placing anomalous values of the magnetic field on the vertical of the geological bodies causing them (Baranov, 1957). The application of the RP filter to UC data is shown in Figure 8c: these data have been used as the basis for the application of the mathematical filters described below.

Local magnetic field of the study area, upward continued and reduced-to-pole, presents a principal positive anomaly (reaching values higher than 400 nT with respect to IGRF) sited near the center of the area (Figure 8c) which is potentially due to the underground geologic body we aim to characterize. Also present is a smaller peak, south of the principal one, which might be related with the volcanic stratigraphy of the shore.

1 DATA FILTERING: OPERATIONS WITH DIRECTIONAL GRADIENTS

In the last decades, a variety of methods based on vertical and horizontal derivatives of surveyed potential field data have been developed as efficient tool for the determination of geometric parameters of causative bodies (such as location of boundaries and depth-to-top) and structures (i.e. major faults. Nabighian, 1972; Roest *et al.*, 1992; Miller and Singh, 1994; Ravat *et al.*, 2002). The first vertical derivative (VDr) of the magnetic field is the rate of change of its intensity (M in Table 1) in the vertical direction. Its computation removes long wavelength features of the magnetic field and, while it amplifies signals from shallower sources, it significantly improves the resolution of closely spaced anomalies (Hood, 1965). VDr (Equation 1 in Table 1), on a map, has its zero values over the vertical edges of thick source bodies and positive and negative values over positive and negative anomalies (Cooper and Cowan, 2004). In Figure 9a the first order VDr of the UC and RP data is shown, together with the representation of a likely anomaly' source edge, drawn approximately following the zero contour. In the image, the magnetic response from the southern anomaly seems slightly heightened.

Table 1. Equations describing computational filters used on magnetic data. See text for explanation.

Equation #	Formula	Measure
1	$VDr = \dfrac{\partial M}{\partial z}$	$\dfrac{\eta T}{m}$
2	$2VDr = \dfrac{\partial^2 M}{\partial z^2}$	$\dfrac{\eta T}{m^2}$
3	$(VDr)THDr = \sqrt{\left(\dfrac{\partial VDr}{\partial x}\right)^2 + \left(\dfrac{\partial VDr}{\partial y}\right)^2}$	$\dfrac{\eta T}{m^2}$
4	$AS = \sqrt{\left(\dfrac{\partial M}{\partial x}\right)^2 + \left(\dfrac{\partial M}{\partial y}\right)^2 + \left(\dfrac{\partial M}{\partial z}\right)^2}$	$\dfrac{\eta T}{m}$
5	$(VDr)AS = \sqrt{\left(\dfrac{\partial VDr}{\partial x}\right)^2 + \left(\dfrac{\partial VDr}{\partial y}\right)^2 + \left(\dfrac{\partial VDr}{\partial z}\right)^2}$	$\dfrac{\eta T}{m^2}$
6	$TA = tan^{-1}\left(\dfrac{VDr}{THDr}\right)$	rad
7	$(TH)TA = tan^{-1}\left(\dfrac{\frac{\partial THDr}{\partial z}}{\sqrt{\left(\frac{\partial THDr}{\partial x}\right)^2 + \left(\frac{\partial THDr}{\partial y}\right)^2}}\right)$	rad

The second vertical derivative (2VDr, Equation 2 in Table 1) is used for improving resolution of anomalies and to delineate geological discontinuities in the subsurface. Lineaments in a 2VDr map would lie at value 2VDr = 0, following abrupt change in magnetization due to geologic structures (Rebolledo-Vieyra *et al.*, 2010; Lopez-Loera *et al.*, 2010). In Figure 9b this filter is applied to our data, showing some imaged potential fault-lines following zero contours on the map, where horizontal gradients are highest. Being a second order filter, 2VDr enhances near surface effects at the expenses of deeper anomalies, it amplifies noise and may produce artificial second derivative anomalies (Wahyudi *et al.*, 2017).

Total Horizontal Derivative (THDr) is considered as the simplest approach to estimate contact locations and has been used as edge detector (Cordell & Grauch, 1985, Cooper & Cowan, 2008). It displays maxima above nearly vertical borders of source bodies (or faults with decent offset) and relative minima at the center and outside of sources. Figure 9c shows the application of this filter to the VDr grid (Equation 3), as in Fedi and Florio (2001), where they used the filter

for defining boundaries of a calderic collapse in southern Italy. Superimposed to the map are some interpreted structures.
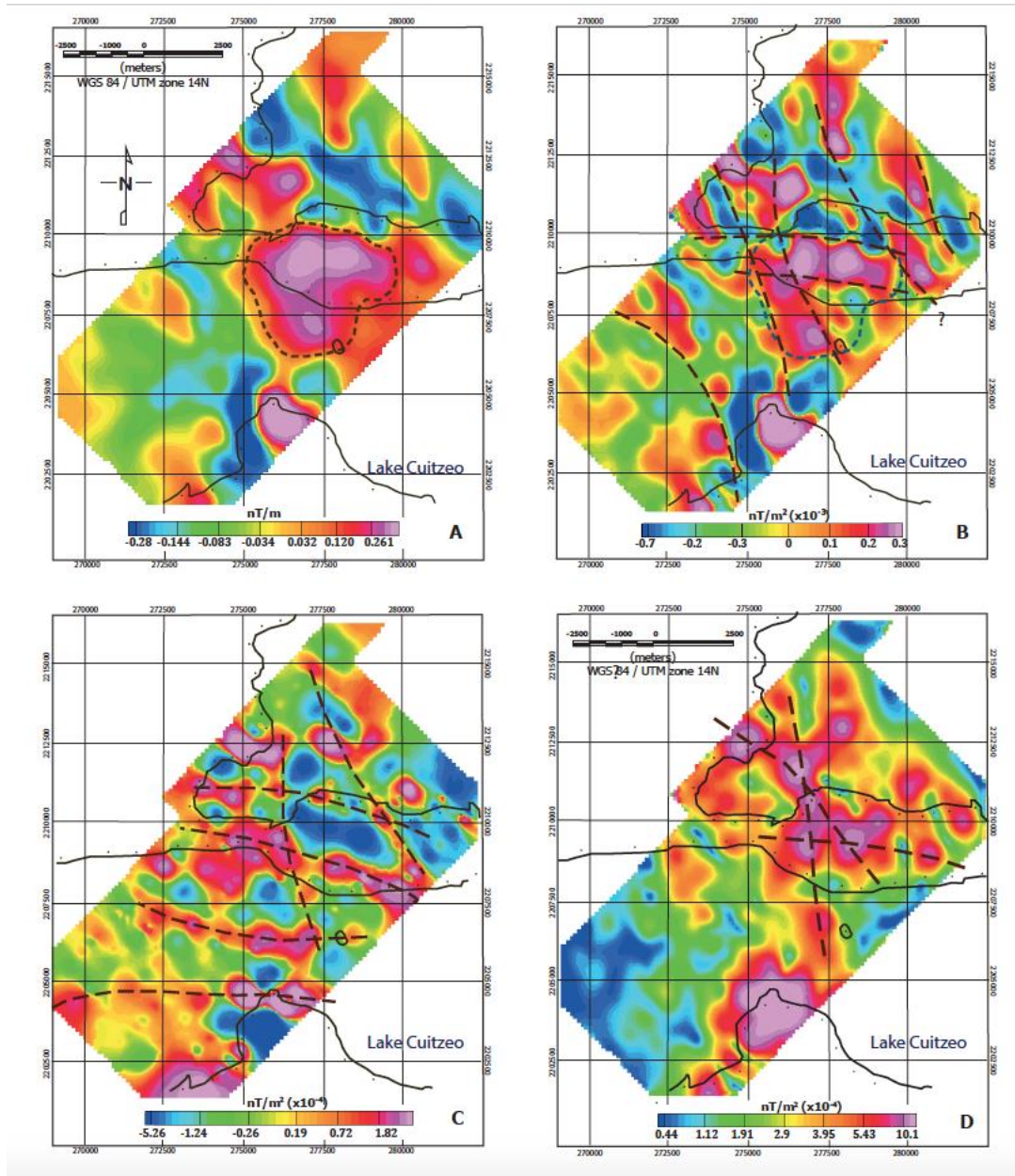

Figure 9. a) First vertical derivative (VDr, equation 1 in Table 1) of the data with contour of the potential magnetic source, interpreted. b) Second vertical derivative (2VDr, eq. 2) applied to our data. Depicted are some potential fault lines, interpreted. c) Total Horizontal derivative (THDr) applied to VDr grid (eq. 3). d) Analytic Signal (AS) applied to VDr grid (eq. 5).

1.1 ANALYTIC SIGNAL

Mathematics, an Analytic Signal (AS) is a complex-valued function that has no negative frequency components. Developed by Nabighian (1972, 1974) and also known as total gradient, the AS amplitude is defined as the square root of the sum of the squared directional derivatives,

as described by eq. 4. AS presents maxima above near vertical magnetic contrasts, identifying faults or geologic bodies of different susceptibility or induced magnetization.

Potential field data correspond to the superposition of all causative sources and nearby source interference yields mislocations (Grauch and Cordell, 1987). Authors have used the filter AS on grids of vertical derivatives of n order (for n = 1, 2) for sharpening nearby boarders (Nabighian, 1972, Roest *et al.*, 1992). Figure 9d displays the AS filter applied to the VDr grid (eq. 5). The signal due to the southern positive anomaly appears strongly enhanced and, while this filter distinguishes between the two anomalies, it only marginally helps in structures identification. From the image we could recognize a N-S and a E-W striking structures crossing near the centre of the picture and a NW-SE structure which we could not recognize through the application of other filters but that may also belong to B&R deformation. Application of AS to higher order vertical derivatives of our data amplifies high-frequency noise to intolerable levels, further attenuating deep source signal.

Since the strength of a magnetic field decays proportionally to source–receptor distance cubed, a handicap of these simple derivative-based filters is that they tend to magnify shallow sources at the expenses of deeper ones, whose gradients measured at surface are weaker. Particularly for our data, the southern anomaly recognized on the RP map (fig. 8c) seems enlarged by vertical derivations (fig. 9a, b and d).

2 TILT ANGLE

The Tilt Angle (TA), introduced by Miller and Singh (1994) for profiled data and improved by Verduzco *et al.* (2004) for 3D cases, overcomes the problem of amplifying shallow sources, which characterizes simple derivative-based filters. This is accomplished by dealing with the ratio of the vertical derivative to the horizontal one, as in Eq. 6. Both VDr and THDr will be smaller for deep sources than for shallower ones, so that their ratio will still be large over the source, pass through zero over or near the edges (where VDr is zero and THDr presents maxima), and will be negative outside of the magnetic body (where VDr < 0), in 2D. Due to the nature of the arctan trigonometric function, all amplitudes are restricted to values between $\pi/2$ and $-\pi/2$ (+90° and -90°) regardless of the amplitudes of VDr and THDr (Miller and Singh, 1994). These facts make this filter function like an automatic gain control (AGC) sieve, tending to equalize the amplitude of the signal for shallow and deeper sources (Verduzco *et al.*, 2004; Salem *et al.*, 2007). The application of the TA to our data is shown in Figure 10. This filter gives the two sources (northern and southern, in the image) balanced leverages: the dimensions of the southern anomaly appear downsized and can be linked with a shallow source (shore' volcanic stratigraphy?).

Salem *et al.* (2007) developed the 'Tilt-depth method' for estimating the depth of a magnetic source from 2D TA maps. They demonstrated how, under certain assumptions such as when contacts (between differently magnetized lithologies) are nearly vertical and the magnetic field is vertical (or RP), contours of TA on a map can help identifying both the edges of magnetic structures (TA = 0) and their depth, as half the physical distance between $\pm\pi/2$ contours. They applied the method on aeromagnetic data over the Karoo sedimentary rift structures of southeast Tanzania (Salem *et al.*, 2007). Applied to our data (Figure 10), the methodology estimates a depth for the roof of the magnetic body (which we argue to equal the depth of the bed of Cuitzeo'

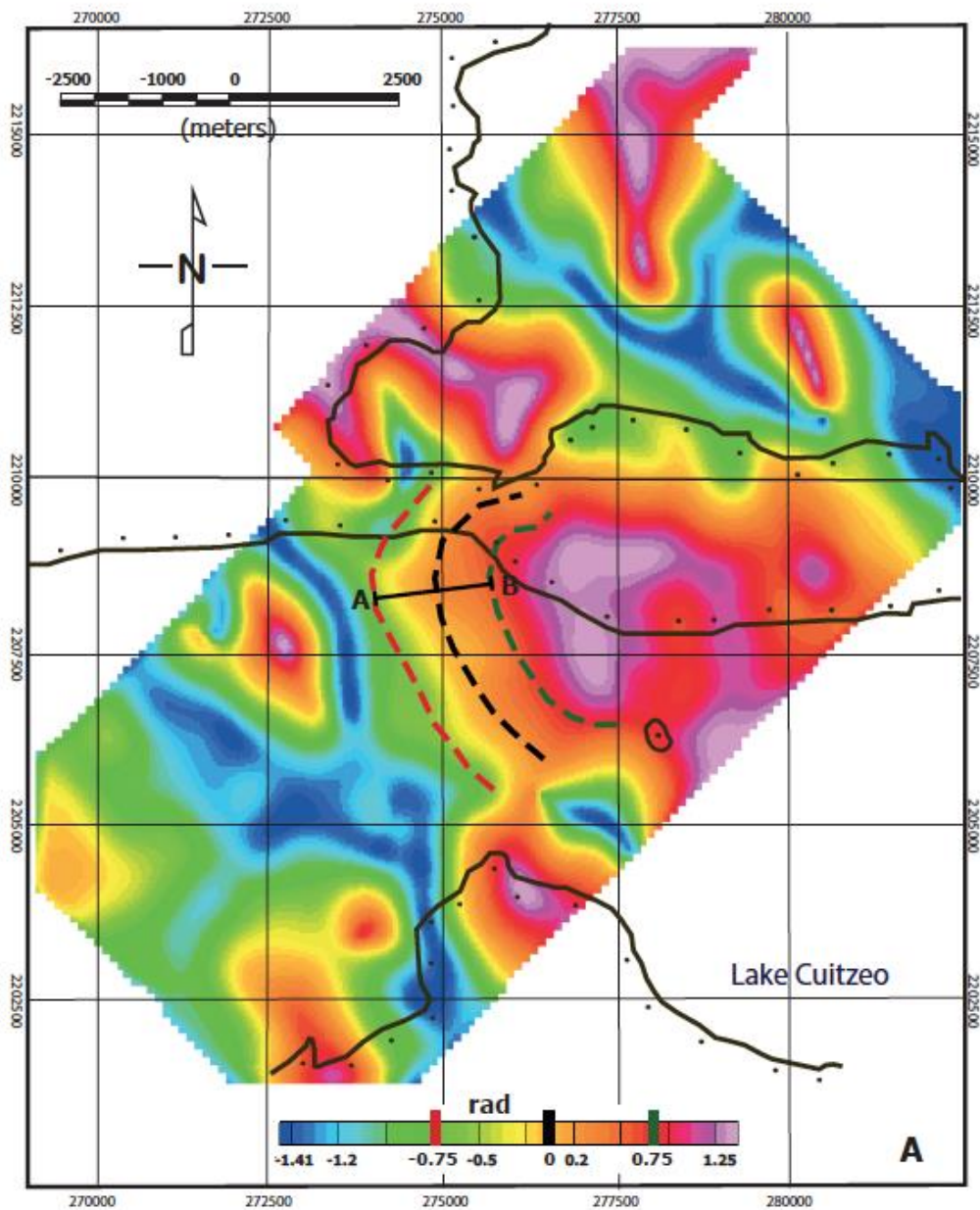lacustrine sedimentation, at the site) between about 700 and 900 m (depth = AB/2, on the TA map).

Figure 10. Tilt-Angle (TA, eq. 6) applied to our data. Coloured dotted lines are drawn following the contours TA=-0.75, 0.75 and 0, for the application of the *Tilt-depth* method, described in the text.

2.1 TILT ANGLE OF THE HORIZONTAL GRADIENT

Ferreira *et al.* (2013) presented an edge detection method that is based on the enhancement of the THDr of magnetic anomalies using the TA. Referred to as Tilt angle of the (total) horizontal gradient, (TH)TA was applied by the authors to 3D synthetic models, displaying balanced maxima over the

edges of magnetic prisms located at different depths with outstanding precision, particularly when compared to other edge detection methods. Also, the filter was tested for the detection of edges of superimposed sources (Ferreira *et al.*, 2013), obtaining promising results. The authors applied the filter to aeromagnetic data of an area in the central portion of the Ribeira belt (state of Rio de Janeiro, southeastern Brazil), a Neoproterozoic range consisting of four tectonostratigraphic terranes. Through its maxima, the filter helped in defining major regional faults and shear zones and in characterizing dykes and other intrusions (Ferreira *et al.*, 2011).
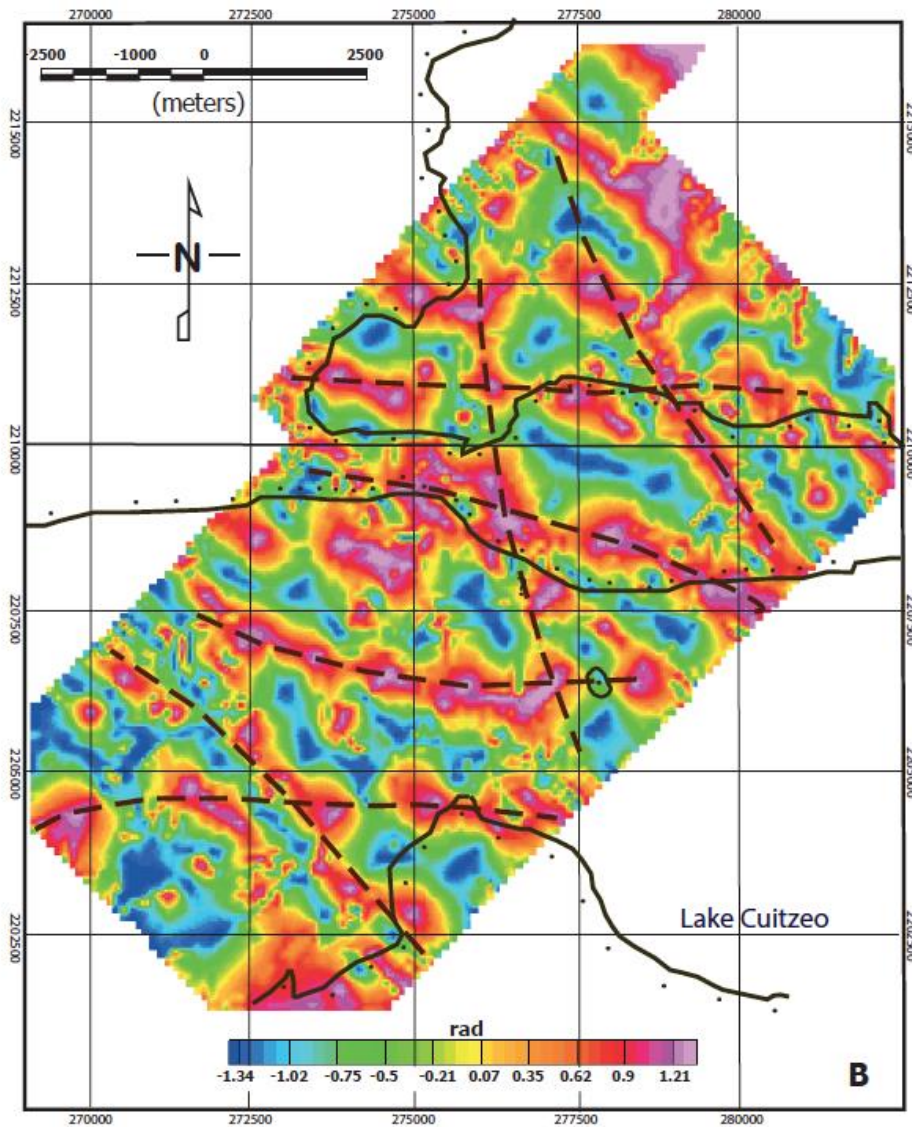

Figure 11. TA applied to the THDr grid, (TH)TA, eq. 7. Superimposed are the traces of some potential fault lines, interpreted.

We applied (TH)TA to our data (eq., 7. Figure 11) and it revealed very useful in locating potential faults, giving support to our structural interpretation. Main TMVB (E-W) and B&R (N-S) faults in our study area, identified by this method through positive sharp peaks, affect the volcanic bedrock (pre-TMVB) and the >8 Ma old lacustrine sedimentation, thicker than 700 m above the magnetic source in study. There are recurrent E-W structures affecting the study area,

one of which interests the Cuitzeo peninsula (Figures 7, 9a, b, c, 11) that, being located on top of the magnetic anomaly in maps, could be directly related to the once hotter magma body, now causing the magnetic anomaly. Particularly, the southern half of the peninsula is made up of lava flows of basic composition (andesite) and is separated from the northern half, constructed with ignimbritic products, by an E-W structure lying approximately in the middle (figure 7a): the two lithologies might have been erupted from the fissure itself, potentially during the same event. On the other hand, we believe that the volcanic island in the middle of the lake may be linked with a N-S structure, as explained in the conceptual model of the system, in the following.

DISCUSSION AND CONCLUSIONS

The application of filters based on combinations of directional derivatives to magnetic data surveyed over the middle section of Lake Cuitzeo helped in the identification of structures potentially affecting the underground, below and within the cap-rock layer consisting of the basin sedimentation. While the application of the vertical derivatives and tilt angle filters to the data may indicate the presence of a cylindrically shaped magnetic body at a depth shallower than 1 km (Figures 9a and 10), the interpretation of results is based on restricting assumptions (e.g. verticality of lateral borders) which would indeed characterize the magnetic body based on its inherent geometry, related to its nature and origin. The Authors of this work have been criticized on a previous publication (Mazzoldi *et al.*, 2016) in that the magnetic anomaly in the study area may be due to a volcanic structure older than the Cuitzeo lake (8-10 Ma) and submerged by the lake sediments afterward, thus not related with the geothermal system. Transect in Figure 3 shows the stratigraphy below the sediments of lake Cuitzeo, displaying massive amounts of andesitic material constituting the TMVB basement. Authors agree that a TMVB 'basement volcanism', with the same general geometry of the present arc and developed during a time-span comprehending the last activities of SMO and the beginning of proper TMVB volcanism, should be considered as an independent volcanic province (Gutiérrez-Negrín, 1988; Ferrari *et al.*, 1999). With an approximate age between 15 and 7 Ma, its volcanic products would still belong to a calc-alkaline series, but more acidic than TMVB magmas (Venegas *et al.*, 1985; Garduño-Monroy and Gutiérrez-Negrín, 1992), somehow representing a middle member between SMO and TMVB – which contrast with the thesis of the magnetic high being due to a volcanic edifice of ultrabasic composition (needed to justify the anomaly under the lake).

The highly basic and ultrabasic magmas of the MGVF, solidified underground below the lake sediments and forming the studied magnetic anomaly, allowed to shed some light on the structural condition of the geothermal reservoir at Cuitzeo, through the application of directional filters to our raw magnetic data. Our interpretation of results images E-W and N-S to NW-SE strikes (e.g. Figure 11) as principal directions of the faults present in the area. These would be transtensive structures belonging respectively to the TMVB tectonics, extending to the north, and to the older B&R, ENE-directed extensive tectonics. We have also defined dimensions and depth of the magnetic body that we believe could be the heat source of the geothermal system in existence, described below.

1 GEOTHERMAL SYSTEM UNDER LAKE CUITZÉO

Thinned crust is often characterized by listric normal faults which tend to flatten at a depth proximal to the brittle-ductile transition (Jackson and McKenzie, 1983; Brogi *et al.*, 2003). The top of the reflective zone is generally located at about 15±5 km (McCarthy and Thompson, 1988; Mayer *et al.* 1997) but it tends to be shallower beneath regions with higher heat flow (Ranalli, 1995). An example can be found in southern Tuscany, central Italy, in the geothermal areas of Lardarello and Amiata (Batini *et al.*, 1978; 1983; Borgia *et al.*, 2014), where the regional average heat-flow is very high (120 mW/m2; Brogi *et al.*, 2003) and the brittle-ductile transition reach depths as shallow as 3-6 km (Batini *et al.*, 1985; Liotta and Ranalli, 1999), together with its shear-decollement zone properties (Borgia *et al.*, 2014; Mazzoldi *et al.*, 2015). At this depth main listric normal faults flatten.

Along the length of the E-W Chapala-Tula fault system – a proto-continental rift for some authors (see above) – the general northward extension, the frequency of geothermal areas, the high average heat flow (≥80 mW m-2) and the average low dip of the domino fault-systems (lower than 70o between Morelia and lake Cuitzeo), make us suppose that the main E-W structures, coeval to the TMVB (8-10 Ma, and potentially already active during TMVB basement volcanism, >15 Ma, Mendoza-Ponce *et al.*, 2018), find a decollement shear-zone at a depth of no more than 8-10 km (probably shallower) – at which level they flatten. On the other hand, being active since the construction of the TMVB, NW- to N-trending Basin&Range faults, older than 20 Ma and with a higher angle of dip, could reach deeper than 15 km: the imposition of the regional average high heat-flow in the area, some 10 Ma (or 15-18 Ma, depending on whether the TMVB basement volcanism is considered as a main player for heat-flow and E-W faults activation), only relatively affected their geometry.

From these observations we derive our essential conceptual model of the geothermal system. In Figure 12a an idealized section cutting along the longitude of the TMVB is presented. The image summarizes the most recent models for the subduction of the Rivera and Cocos plates, previously described, with the two main gaps in Quaternary volcanism at the surface (Colima Gap and Tzitzio Gap) coinciding with the presence of tear faults at depth. This geometry involves a relatively strong vertical heat-flow for those sectors interested by the tears. Figure 12b depicts our conceptual model of the geothermal system. A soaring basaltic/andesitic magmatic body, exploiting a B&R structure of the T-VdS fault system for its rising, got trapped at near-surface level under a thick layer of plastic clay, identifiable with Cuitzeo lacustrine sedimentation, which interrupted its vertical motion, sometime during the last 500 ka. Hydrothermal calcite interesting B&R fault planes on the southern shore of the lake (figure 7d), and thick sinter deposits near hydrothermal springs, suggest that the system might have been bigger and more vigorous in the past. Activity of the N-S faults would have made it possible for a portion of the magma to reach the surface, through the clayey caprock, forming the andesitic island in the middle of the lake. Also, as shown by geological and geophysical analyses (e.g., figures 7a, 9b, 11), the whole peninsula of Cuitzeo may be related to this same intrusion through a E-W structure, more active than B&R, interesting the main part of its extension. Along the depth of the crystallized, still hot intrusion, water would heat up and consequently ascend to the surface, through listric E-W fault planes, more active and highly fractured (permeable) along their intersections with almost vertical B&R planes. These permeable intersections control the location of geothermal springs at the surface (e.g. Sibson, 1990; Figure 12b).
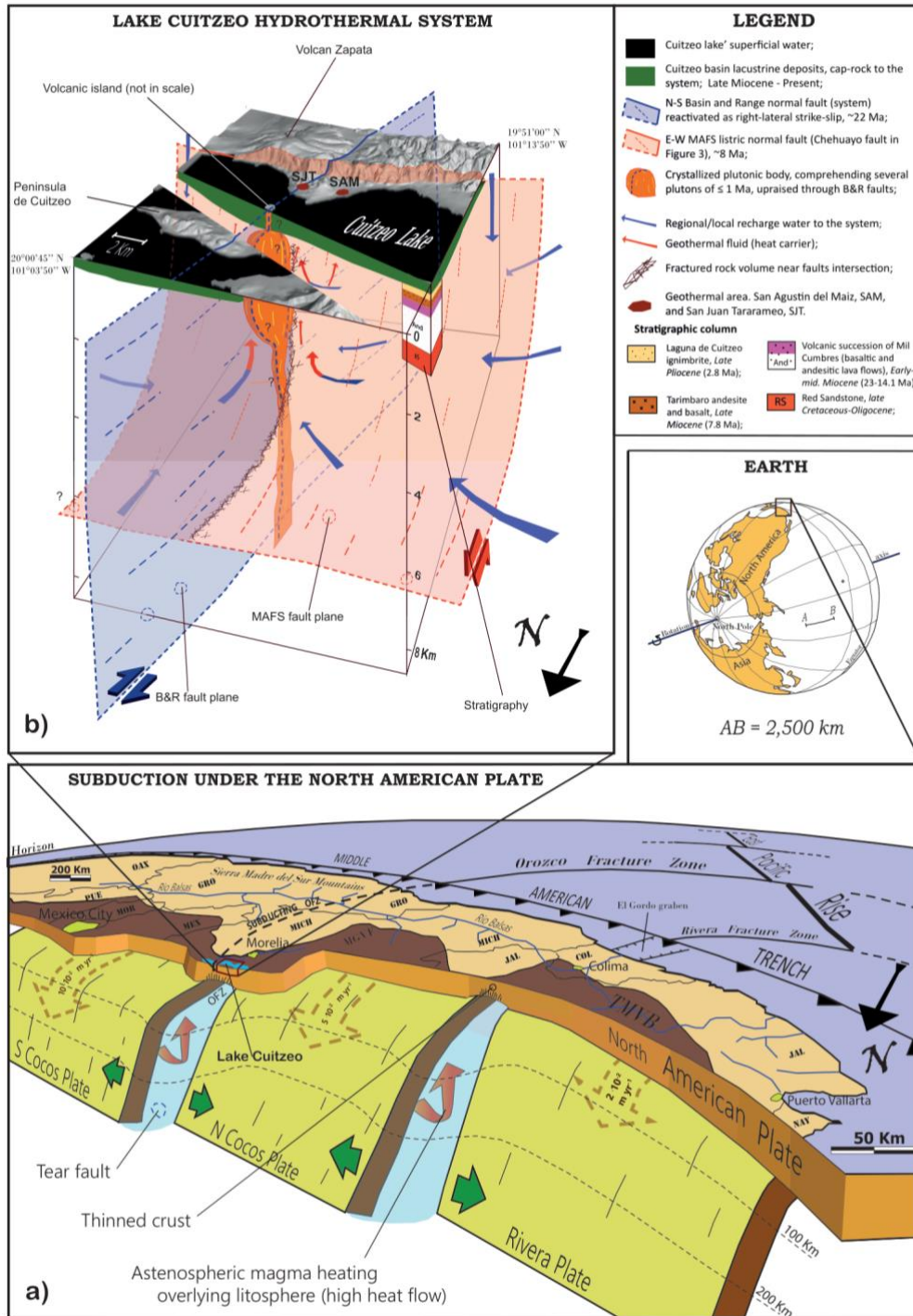
Figure 12. A) 3D representation of the subduction process under the North American Plate, as described in the text. The image highlights the importance of the subduction of fracture zones, the consequent presence of tear faults and their effect on surface volcanism (Tzitzio and Colima Gaps). While the dotted arrows over the subducting plate segments represent their (subduction) velocity, the red arrows drafted in correspondence with the tear faults separating plate' segments represent the toroidal flow of mantle around the Rivera and N Cocos plates (e.g., León-Soto *et al.*, 2009) and the resulting high heat-flow; B) 3D representation of our conceptual model of the geothermal system. Hot magma, ascending through a B&R fault found in a thick layer of lake sediments a barrier to reach the surface. A geothermal system is then created: hot water finds its way upward through fractured rocks near the intersection of B&R and TMVB faults.

At San Agustin del Mais, there is already some experience in geothermal development, thanks to different thermal resorts in the area, and geothermal fluid at about 130$_\circ$C is exploited at some 300 m depth (personal communication from spa owner). The estimated reservoir temperatures (150-220$_\circ$C, par. 2.4) and the mixing trend of the geothermal fluid (Segovia *et al.*, 2005) lead to the hypothesis that fluid at T>150$_\circ$C can be economically harvested somewhere around 500-600 m depth, provided the fractured zone of the main E-W fault bordering the southern bank of the Cuitzeo lake is targeted, particularly near its intersection with B&R structures, to avoid permeability issues during production. Geothermal exploitation at the site may be profitable to the industry and probably also to the local economy, although, on top of the presumed environmental stress delivered to an already polluted area, less heat may be available to local spas after beginning of production.

2 ALIGNMENTS OF CONES IN THE MGVF AND ORIGIN OF THE PLUME

Within MGVF authors have detected small-cones alignments following geologic lineaments, confirming that distribution of volcanoes can be the expression of stress conditions in the crust during activity (Hasenaka, 1984; Hasenaka and Carmichael, 1985; Cebriá *et al.*, 2010). In the southern half of the field, NE-striking alignments of cinder cones are evident (Ban *et al.*, 1992; Figure 13), coinciding with the orientation of the Tenochtitlán Fault System whose mean faults strike parallels the relative motion vector of the Cocos and North American plates (40$_\circ$; DeMets *et al.*, 1990), defining an approximately NW-SE σ_3. These structures controlled the spatial distribution of many monogenetic and polygenetic volcanoes within the TMVB, hold evidences of Holocene reactivation, and disciplined the eruption of >70 cinder cones in MGVF, younger than 40,000yr (Ban *et al.*, 1992; Cebriá *et al.*, 2010; Figure 13). NE-striking lineaments contain Paricutin and Jorullo volcanoes (recently active) at their SW edges, and, if prolonged towards the NE, would interest our study area. Although results of our geophysical survey do not support the existence of NE-SW faults below Cuitzeo lake, these structures exist some km south of the SW shore of the lake (see Figures 2, 4, 7 and 13).

In the northeastern and northwestern parts of MGVF, authors described alignments of cinder cones with E-W strikes (Hasaka and Carmichael, 1985; Ban *et al.*, 1992), clearly related to the Chapala-Tula fault system. These faults, potentially delineating a young rift zone over the axis of TMVB, may also be invoked as cause for the ascent of the plume, below the lake, although their relatively low angle of dip would make this option less preferable.

The last lineament of interest is located at the northeastern sector of the MGVF, where some 13 maars (and many cinder-cones, not represented in figure 13), aged between 1.8 and 0.075 Ma (Aranda-Gomez and Carrasco-Nuñez, 2014) are distributed within an elongated 7 km by 50 km stripe, oriented NNW-SSE. This has been taken as evidence of a pre-existing buried fault system, a zone of deep crustal discontinuity enabling magmas to reach the surface (Murphy, 1982; Uribe-Cifuentes and Urrutia-Fucugauchi, 1999): ascending magma encountered the regional aquifer, favoring the generation of phreatomagmatic eruptions (Aranda-Gomez and Carrasco-Nuñez, 2014). Some of these maars hold lower crustal xenoliths, which is proof of their deep origins (Uribe-Cifuentes and Urrutia-Fucugauchi, 1999; Ortega-Gutiérrez *et al.*, 2014).

Following the most recent models (e.g. Blatter and Hammersley, 2010; Stubailo *et al.*, 2012), this zone of crustal weakness occupy part of the projection on the surface of the tear fault caused at depth by the subduction of the Orozco Fracture Zone (Figure 12a), which has a high heat

flow, favoring the ascent of astenospheric magma through the lower crust. Figure 13 highlights how, on a map, the alignment of maars strikes parallel to the continuation of the subducting OFZ and, on the ground, to the Tzitzio-Valle de Santiago fault system, already active during Basin & Range tectonics and still today.

We can further our hypothesis based on the volume of magnetic rock needed to create such an anomaly on the surface. If we assign to the magnetic source a diameter of say 3 km in 2D (Figure 9a and 10) and estimate for the plume a similar thickness (3 km, low appraisal), we would have a volume somehow higher than 20 km$_3$, higher than characteristic values of erupted material for monogenetic cinder cones (Max registered 5 km$_3$, Hasenaka and Carmichael, 1985), let alone maars volcanoes. Alaniz-Alvarez *et al.* (1998) observed how, over the TMVB, monogenetic small cones are preferentially oriented parallel to east-west normal faults with high slip rates; on the other hand, polygenetic volcanoes align along faults with low displacement rates (north-south B&R faults). The crystallized magmatic body under Cuitzeo lake, affected by different extensional tectonics, may be more relatable to a shield volcano of the MGVF and, in turn, might have enjoyed different recharge of magma, piling below the clay sediments, during its history.
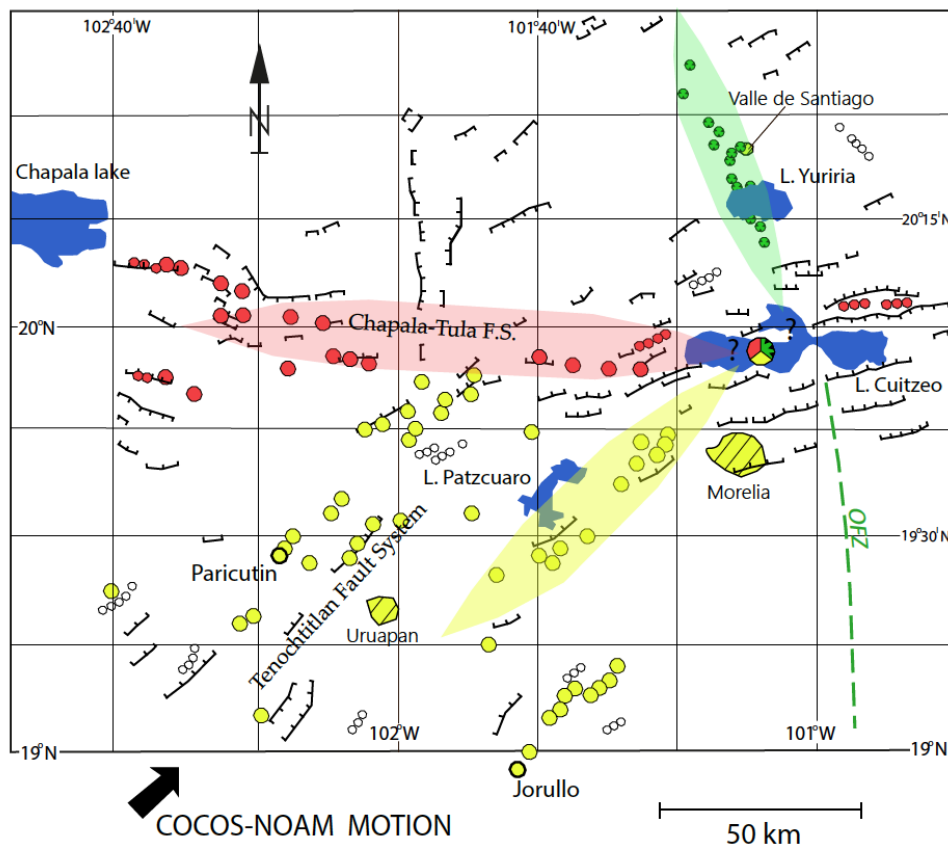

Figure 13. Represented on the map are alignments of volcanic edifice belonging to the MGVF. Particularly, in yellow are depicted some of the cinder cones following Tenochtitlán Fault System structures (N40$_0$); in red, cinder cones are aligned with Chapala-Tula F.S. faults; in green, maars volcanoes are aligned along the Tzitzio-Valle de Santiago Fault System, as described in the text.

2.1 NEW RESULTS

In 2017 researchers from Universidad Michoacana de San Nicolas de Hidalgo (UMSNH) dated some of the E-W normal faults near Cuitzeo lake at about 18 Ma and the island in the middle of the lake (considered in this study) at 17 Ma, through $_{40}Ar/_{39}Ar$ analysis. As we detailed through the text, we believe this age for E-W faults of the Morelia-Acambay fault system reflects the imposition of an early TMVB-basement volcanism (and related heat-flow) which generated the right stress-field for the creation of these structures, probably with a pure extensional motion, during early Miocene times. This new insight might have scientists think again on the age of lake Cuitzeo, currently believed to be around 10 Ma, but probably older. The age of the island is another issue, having been related to the still-hot, crystallized, basic plume under the lake, in this work. An age of 17 Ma would not give any chance to a magmatic body to still be at an interesting temperature for feeding a hydrothermal system at present. A volume of magma as the one imaged in this work would cool down in no longer than say 500 ka after underground emplacement and we may fit this new finding (the age of the island) in our model in basically two ways. First, as we explained in the previous paragraph, the specific structural background of the study area (main N-S and E-W faults intersection) can influence the magma supply and provide recharge over time. Hence, while the island may be an early expression of the phenomenon, repeated magma top-ups from below might have influenced the strength of the geothermal system along time. In this case, a direct affinity with MGVF volcanism is less unambiguous. A second loophole in accounting for the age of the volcanic island is that it might not be related at all with the geothermal arrangement at the site. We believe new geophysical and geological studies should focus on the characterization of perspective geothermal sites laying along the TMVB, with the aim of easing future explorations and broadening general knowledge.

ACKNOWLEDGEMENTS

REFERENCES

Aguirre-Díaz, G.J., and Labarthe-Hernandez, G., 2003. Fissure ignimbrites: Fissure-source origin for voluminous ignimbrites of the Sierra Madre Occidental and its relationship with Basin and Range faulting. Geology, 31, 773–776;

Alaniz-Alvarez, S.A., A.F. Nieto-Samaniego and L. Ferrari, 1998. Effects of strain rate in the distribution of monogenetic and polygenetic volcanism in the Trans-Mexican Volcanic Belt. Geology 26(7). DOI: 10.1130/0091-7613(1998)026<0591:EOSRIT>2.3.CO,2;

Alba-Aldarve, L. A., Reyes-Salas, M., Morán-Zenteno, D., Angeles-Garcia, S. y Corona-Esquivel R., 1996, Geoquímica de las rocas volcánicas terciarias de la región de Taxco-Huautla: Actas Instituto Nacional de Geoquímica, v. 2, p. 39–44;

Aranda-Gómez, J.J. and F. McDowell, 1998. Paleogene extension in the Southern Basin and Range province of Mexico: Syn-depositional tilting of Eocene Red Beds and Oligocene volcanic rocks in the Guanajuato mining district. Int. Geol. Rev,40(2), 116-134;

Aranda-Gomez, J.J. and G. Carrasco-Nuñez, 2014. The Valle de Santiago maars, México: the record of magma-water fluctuations during the formation of a basaltic maar (La Alberca) and active post-desiccation subsidence at the bottom of a maar lake (Rincón de Parangueo). Conf. Proc. 5th Int. Maar Conference. Nov. 20, 2014, Queretaro, Mexico;

Arredondo-Fragoso, J.J., 1983. Levantamiento gravimetrico en la zona central de la laguna de Cuitzeo, Michoacán. Informe 29-83, Comision Federal Electricidad, Gerencia de proyectos geotermicos. Mexico;

Ban, M., T. Hasenaka, H. Delgado-Granados and N. Takaoka, 1992. K-Ar ages of lavas from shield volcanoes in the Michoacán-Guanajuato volcanic field, Mexico. Geofisica Internacional 31, 4: 467-473;

Bandy, W.L., 1992. Geological and Geophysical Investigation of the Rivera-Cocos Plate Boundary: Implications for Plate Fragmentation. Ph.D. Dissertation, Texas A&M University, College Station, Texas, 195p;

Bandy W.L., Mortera-Gutierrez C., Urrutia-Fucugauchi J. and Hilde T.W.C., 1995. The subducted Rivera-Cocos plate boundary: Where is it, what is it, and what is its relationship to the Colima rift?. Geophys. Res.Lett., 22, 3075-3078;

Bandy W.L., T.W.C. Hilde and C.-Y. Yan, 2000. The Rivera-Cocos plate boundary: Implications for Rivera-Cocos relative motion and plate fragmentation, in Cenozoic Tectonics and Volcanism of Mexico, edited by H. Delgado-Granados, G. Aguirre-Díaz, and J.M. Stock, Spec. Pap. Geol. Soc. Am., 334, 1–28;

Baranov, V., 1957. A new method for interpretation of aeromagnetic maps: pseudo-gravity anomalies, Geophysics, 22, 359-383;

Batini, F., Burgassi, P.D., Cameli, G.M., Nicolich, R., Squarci, P., 1978. Contribution to the study of the deep lithospheric profiles: deep reflecting horizons in Larderello-Travale Geothermal field. Mem. Soc. Geol. Ital. 19, 477– 484;

Batini, F., Bertini, G., Giannelli, G., Pandeli, E., Purceddu, M., 1983. Deep structure of the Larderello geothermal field: contribution from recent geophysical and geological data. Mem. Soc. Geol. Ital. 5, 219– 235;

Batini, F., G. Bertini, G. Giannelli, E. Pandeli, E. Puxeddu and I. Villa, 1985. Deep structures, age and evolution of the Larderello-Travale geothermal field. Geothermal Res., Comm. Transaction, 9 (1978), 1-7;

Blatter, D., G. Farmer and I. Carmichael, 2007. A north-south transect across the central Mexican volcanic belt at 100oW: Spatial distribution, petrological, geochemical, and isotopic characteristics of quaternary volcanism, J. Petrol., 48, 901–950;

Blatter, D.L. and L. Hammersley, 2010. Impact of the Orozco Fracture Zone on the central TMVB. J. Volc. Geother. Res. 197 (2010) 67–84;

Borgia, A., Mazzoldi, A., Brunori, C.A., Allocca, C., Delcroix, C., Micheli, L., Vercellino, A., Grieco, G., 2014. Volcanic spreading forcing and feedback in geothermal reservoir development, Amiata volcano, Italia. J. Volcanol. Geotherm. Res. 284 (2014), 16;

Brogi, A., Lazzarotto, A., Liotta D. and G. Ranalli, 2003. Extensional shear zones as imaged by reflection seismic lines: the Lardarello geothermal field (central Italy). Tectonophysics 363 (2003), 127–139;

Campa-Uranga, M.F. and P.J. Coney, 1983. Tectono-stratigraphic terranes and mineral resource distribution in Mexico. Canadian Journal of Earth Sciences, 20, 623 1040-1051;

Campos-Enriquez, O.J., Herrera, M.C.R. and E. Bigurra-Pimental, 1988. Resultados preliminares del estudio magnetotelurico del área geotérmica de Araró y San Agustin del Maiz, Mich., MX. Informe 13/88. Comision Federal Electricidad, Gerencia de proyectos geotermicos. Mexico;

Cashman, P.H., J.E. Faulds and N.H. Hinz, 2012. Regional variations in structural controls on geothermal systems in the Great Basin. GRC Transactions, Vol. 36, 2012; 25-30;

Cebriá, J.M., C. Martin-Escorza, J. Lopez-Ruiz, D. Moran-Zenteno & B.M. Martiny, 2010. Numerical recognition of alignments in monogenetic volcanic areas: Example from the Michoacán-Guanajuato Volcanic Field in Mexico and Calatrava in Spain. J. Volc. Geoth. Res., 2010, 1-4;

Clemente-Chavez A., A. Figueroa-Soto, F.R. Zuñiga, M. Arroyo, M. Montiel and O. Chavez, 2013. Seismicity at the northeast edge of the Mexican Volcanic Belt (MVB) and activation of an undocumented fault: the Peñamiller earthquake sequence of 2010–2011, Querétaro, Mexico. Nat. Hazards Earth Syst. Sci., 13, 2521-2531;

Coolbaugh, M.F., Raines, G.L., Zehner, R.E., Shevenell, L., and Williams, C.F., 2006. Prediction and discovery of new geothermal resources in the Great Basin: Multiple evidence of a large undiscovered resource base: Geothermal Resources Council Transactions, v. 30, p. 867-873;

Cooper, G.R.J. and D.R. Cowan, 2004. Filtering using variable order vertical derivatives. Computer & Geoscience, 30, 455-459;

Cooper, G.R.J. and D.R. Cowan, 2008. Edge enhancement of potential-field data using normalized statistics. Geophysics, 73 (3), H1–H4;

Cordell, L. and Grauch, V.J.S., 1985. Mapping basement magnetization zones from aeromagnetic data in the San Juan Basin, New Mexico. In: The Utility of Regional Gravity and Magnetic Anomalies Maps. Society of Exploration Geophysicists, 181–197;

Curewitz, D. and J.A. Karson, 1997. Structural settings of hydrothermal outflow: Fracture permeability maintained by fault propagation and interaction. Journal of Vulcanology and Geothermal Research, 79. 149-168;

DeMets, C., R.G. Gordon, D.F. Argus and S. Stein, 1990. Current plate motions. Geophysical J. International, 101: 425-478;

Dickinson, W.R., and Lawton, T.F., 2001. Carboniferous to Cretaceous assembly and fragmentation of Mexico: Geological Society of America Bulletin, v. 113, p. 1142–1160, doi: 10.1130/0016-7606(2001)113<1142;

Dougherty S.L., Clayton R.W. and Helmberger D.V., 2012. Seismic structure in central Mexico: Implications for fragmentation of the subducted Cocos plate. J. Geophys. Res. 117;

Ego F. and V. Ansan, 2002. Why is the Central Trans-Mexican Volcanic Belt (102o-99oW) in transtensive deformation? Tectonophysics 359, 189-208;

Faulds, J.E., Coolbaugh, M., Bouchot, V., Moek, I., Oguz. K., 2010. Characterizing

Structural Controls of Geothermal Reservoirs in the Great Basin, USA, and Western Turkey:Developing Successful Exploration Strategies in Extended Terranes. International Geothermal Association. World Geothermal Congress 2010, Apr 2010, France. 11 p. <hal-00495884>;

Faulds, J.E., Hinz, N., Kreemer, C. and M. Coolbaugh, 2012. Regional Patterns of Geothermal Activity in the Great Basin Region, Western USA: Correlation with Strain Rates. GRC Transactions, 36;

Faulds, J.E. and N. Hinz, 2015. Favorable Tectonic and Structural Settings of Geothermal Systems in the Great Basin Region, Western USA: Proxies for Discovering Blind Geothermal Systems. Proceedings of the World Geothermal Congress 2015. Melbourne, Australia, 19-25 April 2015;

Fedi, M. and G. Florio, 2001. Detection of potential field source boundaries by enhanced horizontal derivative method. Geophysical Prospecting, 49, 40-58;

Ferrari, L., Garduño, V.H., Pasquare` G., and Tibaldi, A., 1991, Geology of Los Azufres caldera, Mexico, and its relationships with regional tectonics: J. Volc. Geoth. Res., 47, 129–148;

Ferrari, L., Pasquaré, G., Venegas, S., Castillo, D. and F. Romero, 1994. Regional tectonics of western Mexico and its implications for the northern boundary of the Jalisco block. Geofis. Int. 33, 139-151;

Ferrari, L., Lopez-Martinez, M., Aguirre-Dıaz, G. and G. Carrasco-Nuñez, 1999. Space–time patterns of Cenozoic arc volcanism in central Mexico: from the Sierra Madre Occidental to the Mexican Volcanic Belt. Geology 27, 303–306;

Ferrari, L., G. Pasquare´, S. Venegas-Salgado, and F. Romero-Rios, 2000. Geology of the western Mexican Volcanic Belt and adjacent Sierra Madre Occidental and Jalisco block, Geol. Soc. Am. Spec. Pap., 334, 65–84, 2000;

Ferrari, L., and Rosas-Elguera, J., 2000. Late Miocene to Quaternary extension at the northern boundary of the Jalisco block, western Mexico: The Tepic-Zacoalco rift revised, in Delgado-Granados, H., *et al.*, eds., Cenozoic tectonics and volcanism of Mexico: Geological Society of America Special Paper 334, 41–63;

Ferrari, L., López-Martínez, M., and Rosas-Elguera, J., 2002. Ignimbrite flare-up and deformation in the southern Sierra Madre Occidental, western Mexico—implications for the late subduction history of the Farallon Plate: Tectonics, 21, doi:10.1029/2001TC001302;

Ferrari, L., Valencia-Moreno M and S. Bryan, 2007. Magmatism and tectonics of the Sierra Madre Occidental and its relation with the evolution of the western margin of North America. in Alaniz-Álvarez, S.A., and Nieto-Samaniego, Á.F., eds., Geology of México: Celebrating the Centenary of the Geological Society of México: Geological Society of America. Special Paper 422, p. 1–39, doi: 10.1130/2007.2422(01);

Ferrari, L., T. Orozco-Esquivel, V. Menea, M. Menea, 2012. The dynamic history of the Trans-Mexican Volcanic Belt and the Mexico subduction zone. Tectonophysics 522-523 (2012), 122-149;

Ferreira, F.J.F., de Castro, L.G., A.B.S. Bangiolo, J. deSouza and M.A.T. Romeiro, 2011. Enhancement of the total horizontal gradient of magnetic anomalies using tilt derivatives: Part II – Application to real data. 81st Annual International Meeting, SEG, Expanded Abstract, 887-891;

Ferreira, F.J.F., Souza, J., Bongiolo, A.B.S. and L.G. de Castro, 2013. Enhancement of the total horizontal gradient of magnetic anomalies using the tilt angle. Geophysics, 78, (3). J33-J41;

Fournier, R. O. and Rowe, J.J., 1966. Estimation of underground temperatures from the silica content of water from hot springs and wet-steam wells. Am. J. Sci., 264: 685–697;

García-Palomo, A., J.L. Macias and V.H. Garduño-Monroy, 2000. Miocene to Recent structural evolution of the Nevado de Toluca volcano region, central Mexico. Tectonophysics, 318, 281-302;

Garduño-Monroy V.H. and N.A. Gutiérrez-Negrín, 1992. Magmatismo, hiatus y tectónismo de la Sierra Madre Occidental y del Cinturón Volcánico Mexicano. Geofísica Internaciónal 31, 417-429;

Garduño-Monroy V.H., Spinner J., Ceragioli E., 1993. Geological and structural study of the Chapala rift, State of Jalisco, Mexico. Geofís. Int. 32(1993), 487-499;

Garduño-Monroy V.H., R. Pérez-Lopez, I. Israde-Alcantara, M.A. Rodríguez-Pascua, E. Szynkaruk, V.M. Hernández-Madrigal, M.L. García-Zepeda, P. Corona-Chávez, M. Ostroumov, V.H. Medina-Vega, G. García-Estrada, O. Carranza, E. Lopez-Granados and J. C. Mora Chaparro, 2009. Paleoseismology of the southern Morelia-Acambay fault system, central Mexico. Geofis. Int., 48 (3), 319-335;

Gianiyu, S.A., Badmus, B.S., Awoyemi, M.O., Akinyemi, O.D. and Olurin O.T., 2013. Upward Continuation and Reduction to Pole Process on Aeromagnetic Data of Ibadan Area, South-Western Nigeria. Earth Science Research, 2, 1, 66-73;

Glen J.M.G., Egger, A.E. and D.A. Ponce, 2008. Structures controlling geothermal circulation identified through gravity and magnetic transects, Surprise Valley, California, NW Great Basin. GRC Transactions, 32, 2008, 279-283;

Glen J.M.G., Egger, A.E., Ippolito C., Athens N., 2013. Correlation of geothermal springs with sub-surface fault terminations revealed by high-resolution, UAV-Acquired magnetic data. Proceedings of the Thirty-eight workshop on geothermal reservoir engineering. Stanford University, Stanford, California, February 11-13 2013, SGP-TR-198;

Goldstein, B., G. Hiriart, R. Bertani, C. Bromley, L. Gutiérrez-Negrín, E. Huenges, H. Muraoka, A. Ragnarsson, J. Tester, V. Zui, 2011. Geothermal Energy. In IPCC Special Report on Renewable Energy Sources and Climate Change Mitigation [O. Edenhofer, R. Pichs-Madruga, Y. Sokona, K. Seyboth, P. Matschoss, S. Kadner, T. Zwickel, P. Eickemeier, G. Hansen, S. Schlömer, C. von Stechow (eds)], Cambridge University Press, Cambridge, United Kingdom and New York, NY, USA;

Gómez-Vasconcelos, M.G., Garduño-Monroy, V.H., Macías, J.L., Layer, P.W. and Benowitz, J.A., 2015. The Sierra de Mil Cumbres, Michoacán, México: Transitional volcanism between the Sierra Madre Occidental and the Trans-Mexican Volcanic Belt. Journal of Volcanology and Geothermal Research, 301, 128-147;

Grauch .J.S. and Cordell L., 1987. Limitations of determining density or magnetic boundaries from the horizontal gradient of gravity or pseudogravity data. Geophysics, vol. 52, 1; 118-121;

Gutiérrez-Negrín, L., 1988. The La Primavera (Jalisco, Mexico) Geothermal Field. Geothermal Resources Council, TRANSACTIONS, Vol. 12, 1988 - http://pubs.geothermal-library.org/lib/grc/1001702.pdf;

Hasenaka, T., M. Ban and H.D. Granados, 1994. Contrasting volcanism in the Michoacán-Guanajuato Volcanic Field, central Mexico: Shield volcanoes vs. cinder cones. Geofísica Internacional, 33 (1). 125-138;

Hasenaka, T., 1994. Size, distribution and magma output rate for shield volcanoes of the Michoacán-Guanajuato Volcanic Field, central Mexico. J. Volc. Geoth. Res., 63(1-2): 13-31;

Hasenaka, T. and Carmichael, I.S.E., 1985. The cinder cones of Michoacán-Guanajuato, central Mexico: their age, volume, distribution, and magma discharge rate, J. Volc. Geoth. Res., 25, 104-124;

Hasenaka, T. and Carmichael, I.S.E., 1987. The cinder cones of Michoacán-Guanajuato, central Mexico: Petrology and chemistry. J. Petrology, 28(2): 241-269;

Henry, C.D. and J.J. Aranda-Gomez, 1992. The real southern Basin and Range: Mid- to late Cenozoic extension in Mexico. Geology, 20, p. 701-704;

Hood, P.J., 1965. Gradient measurements in aeromagnetic surveying. Geophysics, 30, 891-902;

Huppert, H. E., and R. S. J. Sparks, 1988. The generation of granitic magmas by intrusion of basalt into continental crust. J. Petrol., 29, 599 – 642;

International Finance Corporation, 2013. Success of Geothermal Wells: a Global Study. Prepared by International Finance Corporation and GeothermEx, Inc. http://www.ifc.org/wps/wcm/connect/7e5eb4804fe24994b118ff23ff966f85/ifc-drilling-success-report-final.pdf?MOD=AJPERES;

Jackson, J. and D. McKenzie, 1983. The geometrical evolution of normal fault systems. J. Structural Geology, 5, 5, 471-482;

Jackson M. and J.A. Bowies, 2014. Curie temperatures of titanomagnetite in ignimbrites: Effects of emplacement temperatures, cooling rates, exsolution, and cation ordering. Geochemistry, Geophysics, Geosystems, (15), 11. 4343-4368;

Keating, P.B: and M. Pilkington, 1990. An automated method for the interpretation of magnetic vertical-gradient anomalies. Geophysics, 55, 336-343;

Kipsang, C., 2015. Cost model for geothermal wells. Proceedings of the World Geothermal Congress 2015. Melbourne, Australia, 19-25 April 2015;

Langridge, R.M., Weldon, R.J.II, Moya, J.C., and Suárez, G., 2000. Paleoseismology of the 1912 Acambay earthquake and the Acambay-Tixmadeje´ fault, Trans-Mexican Volcanic Belt: Geophys. Res., 105, 3019–3037;

León-Soto, G., Ni, J.F., Grand, S.P., Sandvol, E., Valenzuela, R.W., Speziale, M.G., González, J.M.G., Reyes, T.D., 2009. Mantle flow in the Rivera–Cocos subduction zone. Geophysical Journal International 179, 1004–1012;

Liotta, D. and G. Ranalli, 1999. Correlation between seismic reflectivity and rheology in extended lithosphere: southern Tuscany, Inner Northern Apennines, Italy. Tectonophysics 315, 109–122;

Lopez-Loera, H., Urrutia-Fucugauchi and L.M. Alva-Valdidia, 2010. Magnetic characteristics of fracture structure of the Colima Volcanic Complex, western Mexico. Geosphere, 6(1), 35-46;

Luhr, J.F.S., A. Nelson, J.F. Allen and I.S.E. Carmichael, 1985. Active rifting in southwestern Mexico: manifestations of an incipient eastward spreading ridge jump. Geology, 13, 54-57;

Manea, V.C., Manea, M., Kostoglodov, V., Sewell, G., 2005. Thermo-mechanical model of the mantle wedge in central Mexican subduction zone and a blob tracing approach for the magma transport. Physics of the Earth and Planetary Interiors 149, 165-186;

Márquez, A., R. Oyarzun, M. Doblas, and S. P. Verma, 1999. Alkalic (ocean-island basalt type) and calc-alkalic volcanism in the Mexican Volcanic Belt: a case for plume-related magmatism and propagating rifting at an active margin? Geology, 27, pp. 51-54;

Mayer, G., Mai, P.M., Plenefisch, T., Echtler, H., Lu Schen, E., Wehrle, V., Muller, B., Bonjer, K.P., Prodehl, C., Fuchs, K., 1997. The deep crust of the Southern Rhine Graben: reflectivity and seismicity as images of dynamic processes. Tectonophysics 275, 15-40;

Mazzoldi, A., Borgia, A., Ripepe, M., Marchetti, E., Ulivieri, G., Della Schiava, M. and C. Allocca, 2015. Faults strengthening and seismicity induced by geothermal exploitation of a spreading volcano, Mt. Amiata, Italia. J. Volc. Geoth. Res., 301(2015), 159-168;

Mazzoldi, A., J.A. Guevara-Alday, J.J. Gomes-Cortes and V.H. Garduño-Monroy, 2016. Papel de estructuras Basin and Range en la formación del sistema geotérmico al centro-sur del lago Cuitzeo, segmento central del Cinturòn Volcanico Mexicano. Asociación Geotérmica Mexicana. Memorias de XXIII Congreso Anual - Morelia, Mich., 10-11 Marzo 2016;

McCann, W.R. and Habermann, R.E., 1989. Effects of the subduction of bathymetric highs. Pure and Applied Geophysics 129 (1/2), 41-69;

McCarthy, J. and Thompson, G.A., 1988. Seismic imaging of extended crust with emphasis on the western United States. Geol. Soc. Am. Bull. 100, 1361-1374;

Mendoza-Ponce, A., Figueroa-Soto, A., Soria-Caballero, D. and V.H. Garduño-Monroy, 2018. Active faults sources for the Patzcuaro-Acambay fault system (Mexico): fractal analysis of slip rates and magnitudes Mw estimated from fault length. Nat. Hazards Earth Syst. Sci., 18, 3121-3135;

Miller, H. G., and V. Singh, 1994. Potential field tilt - A new concept for location of potential field sources. Applied Geophysics, 32, 213–217;

Morán-Zenteno, D. J., Alba-Aldave, L., Corona-Ezquivel, R., Reyes-Salas, M., Martínez-Serrano, R., and Angeles-García, S., 1999. Stratigraphy and tectonic significance of the Tertiary silicic volcanism in northern Guerrero, México: Revista Mexicana de Ciencias Geologicas, 15(2);

Murphy, G.P., 1982. The chronology, pyroclastic stratigraphy and petrology of the Valle de Santiago maar field, central Mexico. M.Sc. Thesis, University of California, Berkeley, USA;

Nabighian, M.N., 1972. The analytic signal of two-dimensional magnetic bodies with polygonal cross-section: Its properties and use for automated anomaly interpretation. Geophysics, 37: 507-517;

Nabighian, M.N., 1974. Additional comments on the analytic signal of two dimensional magnetic bodies with polygonal cross-section. Geophysics, 39, 85-92;

Nieto-Samaniego, A.F., Ferrari, L., Alvaniz-Alvarez, S.A., Labarthe-Hernandez, G. and R. Rosas-Elguera, 1999. Variation of Cenozoic extensión and volcanism accross the southern Sierra Madre Occidental volcanic province, Mexico. Geol. Soc. Am. Bull., 111, 347-363;

Nixon, G.T., 1982. The relationship between Quaternary volcanism in central Mexico and the seismicity and structure of subducted ocean lithosphere. Geol.Soc.Am.Bull., 93(6), 514-523;

Ortega-Gutiérrez, F., A. Gomez-Tuena, M. Elias-Herrera, L.A. Solari, M. Reyes-Salas and C. Masias-Romo, 2014. Petrology and geochemistry of the Valle de Santiago lower-crust xenoliths: Young tectonothermal processes beneath the central TMVB. Lithosphere, 6(5): 335-360;

Pardo, M. and G. Suárez, 1995. Shape of the subducted Rivera and Cocos plate in southern Mexico: seismic and tectonic implications. Journal of Geophysical Research 100, 12: 357-373;

Parsons, T.E., 1995. The Basin and Range province: Chapter 7. In: Continental Rifts: Evolution, Structure, Tectonics. USGS Pubblication, Edited by: Elsevier, Series number: 264. Pp. 277-324;

Pasquaré, G., Garduño-Monroy, V.H., Tibaldi, A. and M. Ferrari, 1988. Stress pattern evolution in the central sector of the Mexican Volcanic Belt. Tectonophysics, 146, 353-364;

Pasquaré, G., L. Ferrari, V. H. Garduño-Monroy, A. Tibaldi, and L. Vezzoli, 1991. Geological map of the central sector of Mexican Volcanic Belt, States of Guanajuato and Michoacán, Geol. Soc. Am. Map Chart Ser., MCH 072, 1 sheet, 20 pp., Geol. Soc. of Am., Boulder, Colo., 1991;

Pérez-Lòpez, R., D. Legrand, V.H. Garduño-Monroy, M.A. Rodriguez-Pascua, J.L. Giner-Robles, 2011. Scaling lwas of the size-distribution of monogenetic volcqnoes within the MGVF, Mexico. J. Volc. Geoth, Res. 201, 65-72;

Pipan, M., Forte, E., Del Ben, A., Nava-Alonzo, H.F., Giudetti G. and S. Supriyanto, 2010. Seismic and elettromagnetic study of reservoir properties for geotermal application. Proc. World. Geoth. Congr., 2010. Bali, Indonesia, April 2010;

Prol, R.M., 1991. Terrestrial heat flow in Mexico, in Exploration of the Deep Continental Crust; Terrestrial Heat Flow and the Lithosphere structure. Edited by V. Cermak and L. Rybach, 475-485. Springer-Verlag, New York, 1991;

Ranalli, G., 1995. Rheology of the Earth, 2nd ed. Chapman and Hall, London;

Ravat, D., Kirkham, K. and T.G. Hildenbrand, 2002. A source-depth separation filter: Using the Euler method on the derivatives of total intensity magnetic anomaly data. The leading edge. April 2002, 360-365;

Robelledo-Vieyra, M., Urrutia-Fucugauchi, J., Lopoez-Loera, H., 2010. Aeromagnetic anomalies and structural model of the Chicxulub multiring impact cráter, Yucatan, Mexico. Revista Mexicana de Ciencias Geologicas, 27, 1, 185-195;

Roest, W.R., Verhoef, J., Pilkington, M., 1992. Magnetic interpretation using 3-D analytic signal. Geophysics 57, 116-125;

Rosas-Elguera, J., L. Ferrari, Lopez-Martinez, M. and F.J. Urrutia.Fucugauchi, 1997. Stratigraphy and tectonics of the Guadalajara región and the triple junction area, western Mexico. Int. Geology Review, 39. 125-140;

Rowland, J.V. and R.H. Sibson, 2004. Structural controls on hydrothermal flow in a segmented system, Taupo Volcanic Zone, New Zeland. Geofluids 4, 259-283;

Salem, A., Williams S., Fairhead J.D., Ravat D. and Smith R., 2007. Tilt-depth method: A simple depth estimation method using first-order magnetic derivatives. The leading edge, December 2007, 1502-1505;

Segovia, N., Barragan, R.M., Tello, E., Alfaro, R., Mena, M., 2005. Geochemical exploration at Cuitzeo Basin Geothermal Zone (Mexico). J. Applied Science 5 (9), 1658-1664;

Servicio Geológico Mexicano, 1988. "Datos magnéticos (vuelos sistemáticos). Grid con datos cada 200 m: E14-A13 (Cuitzeo); E14-A14 (Zinapécuaro); F14-C83 (Moroleón); F14-C84 (Acámbaro)". Escala 1:50000. SGM. México, DF;

Sibson, R.H., 1981. Controls on low-stress hydro-fracture dilatancy in thrust, wrench and normal fault terrain. Nature 289, 665-667;

Sibson, R.H., 1990. Conditions for fault-valve behavior. Geological Society, London. Special Pubblication 54, 15-28;

Singh, S.K., Pardo, M., 1993. Geometry of the Benioff zone and state of stress in the overriding plate in central Mexico. Geophys. Res. Lett. 20, 1483 – 1486;

Stubailo, I., Beghein, C. and P.M. Davis, 2012. Structure and anisotropy of the Mexico subduction zone based on Rayleigh-wave analysis and implications for the geometry of the Trans-Mexican Volcanic Belt. J. Geoph. Res., 117. B05303;

Subir, K.S. and J.W. Morrow, 2011. An investigation of drilling success in Geothermal Exploration, Development and Operation. GRC Transaction, 35;

Suter, M., 1991. State of stress and active deformation in Mexico and the western Central America. In Slemmons, Engdahl, Zoback and Blackwell eds., Neotectonics of North America. Boulder, CO. Geological Society of America Decade Map Volume, 401-421;

Suter, M., Quintero-Leogorrote, O. and M. Lopez-Martinez, 1995a. The Acambay graben: active intra-arc extensión in the Trans-Mexican Volcanic Belt. Tectonics, 14, 1245-1262;

Suter, M., Carrillo-Martinez M., Lopez-Martinez, M. and E. Farrar, 1995b. The Aljibes half-graben—Active extensión at the boundary between the trans-Mexican volcanic belt and the Basin and Range Province, Mexico. Bull. Geol. Soc. Am. 107(6), 627-641;

Suter, M., Carrillo-Martınez, M. and O. Quintero-Legorreta, 1996. Macroseismic study of shallow earthquakes in the central and eastern parts of the Trans-Mexican volcanic belt. Bull. Seismol. Soc. Am. 86, 1952–1963;

Suter, M., J. Contreras, A. Gomez-Tuena, C. Siebe, O. Quintero-Lagorreta, A. Garcia-Palomo, J. Macias, S.A. Alaniz-Alvarez, A.F. Nieto-Samaniego and L. Ferrari, 1999. Effects of strain rate in the distribution of monogenetic and polygenetic volcanism in the Trans-Mexican Volcanic Belt. Geology 27(6): 571-575;

Suter, M., Lopez-Martınez, M., Quintero- Leogorrote, O., and M. Carrillo-Martınez, 2001. Quaternary intra-arc extension in the Central TMVB. Bull. Geol. Soc. Am. 113, 693– 703;

Thebault, E., Finlay, C., Beggan, C., Alken, P., Aubert, J., Barrois, O., Bertrand, F., Bondar, T., Boness, A., Brocco, L., Canet, E., Chambodut, A., Chulliat, A., Coisson, P., Civet, F., Du, A., Fournier, A., Fratter, I., Gillet, N., Hamilton, B., Hamoudi, M., Hulot, G., Jager, T., Korte, M., Kuang, W., Lalanne, X., Langlais, B., Leger, J.M., Lesur, V. and F. Lowes., 2015. International Geomagnetic Reference Field: the 12th generation. Earth, Planets and Space, 67:79;

Uribe-Cifuentes, R.M. and J. Urrutia-Fucugauchi, 1999. Paleomagnetic study of the Valle de Santiago volcanics, Michoacan-Guanajuato volcanic field, Mexico. Geofisica Internacional, Vol, 38. 4: 2017-230;

Urrutia-Fucugauchi, F.J. and J.H. Flores Ruiz, 1996. Bouguer gravity anomaly and regional crustal structure in central Mexico. Int. Geol. Rev. 38, 176–194;

Verduzco, B., J. D. Fairhead, C. M. Green, and C. MacKenzie, 2004. New insights into magnetic derivatives for structural mapping. The Leading Edge, 23, 116–11;

Venegas, S., F. Maciel and J.J. Herrera, 1985. Recursos geotérmico de la Faja Volcánica Mexicana. Geofis. Int., 24-1, 47-81;

Verma P.S. and T. Hasenaka, 2004. Sr, Nd and Pb isotopic and trace element geochemical constraints for a veined-mantle source of magmas in the MGVF, west-central Mexican Volcanic Belt. Geochemical J., 38, 43-65;

Verma, S.P., 2009. Continental Rift Setting for the Central Part of the Mexican Volcanic Belt: A Statistical Approach. The Open Geology J., 3, 8-29;

Wahyudi E.J., Kynantoro Y. and S. Alawiyah, 2017. Second vertical derivative using gravity data for fault structure interpretation. Int. Conf. on Energy Sc.(ICES 2016). doi :10.1088/1742-6596/877/1/012039;

Williams, H., 1950. Volcanoes of the Paricutin region. U.S.G.S. Bulletin 965-C: 281-353;

Zuñiga F.R., J.F. Pacheco, M. Guzman-Speziale, G.J. Aguirre-Díaz, V.H. Espíndola, E. Nava, 2003. The Sanfandila earthquake sequence of 1998, Queretaro, Mexico: activation of an undocumented fault in the northern edge of central Trans-Mexican Volcanic Belt. Tectonophysics 361, 229-238.